

Antiprotonic helium and *CPT* invariance

Ryugo S Hayano¹, Masaki Hori¹, Dezső Horváth^{2,4} and Eberhard Widmann³

¹ Department of Physics, University of Tokyo, 7-3-1 Hongo, Bunkyo-ku, Tokyo 113-0033, Japan

² KFKI Research Institute for Particle and Nuclear Physics, H-1525 Budapest, Hungary

³ Stefan Meyer Institute for Subatomic Physics, Boltzmannngasse 3, A-1090 Vienna, Austria

E-mail: horvath@rmki.kfki.hu

Received 12 March 2007, in final form 31 July 2007

Published 1 November 2007

Online at stacks.iop.org/RoPP/70/1995

Abstract

We review recent progress in the laser and microwave spectroscopy of antiprotonic helium atoms ($\bar{p}\text{He}^+ \equiv e^- - \bar{p} - \text{He}^{++}$) carried out at CERN's Antiproton Decelerator facility (AD). Laser transitions were here induced between Rydberg states (n, ℓ) and ($n \pm 1, \ell - 1$) of $\bar{p}\text{He}^+$ ($n \sim 40$ and $\ell \lesssim n - 1$ being the principal and orbital angular momentum quantum numbers of the antiproton orbit). Successive refinements in the experimental techniques improved the fractional precision on the $\bar{p}\text{He}^+$ frequencies from 3 parts in 10^6 to ~ 1 part in 10^8 . These included a radiofrequency quadrupole decelerator, which reduced the energy of the antiprotons from 5.3 MeV (the energy of the beam emerging from AD) to ~ 100 keV. This enabled the production of $\bar{p}\text{He}^+$ in ultra-low density targets, where collisional effects with other helium atoms are negligible. A continuous wave pulse-amplified dye laser, stabilized against a femtosecond optical frequency comb, was then used to measure the $\bar{p}\text{He}^+$ frequencies with ppb-scale precision. This progress in the experimental field was matched by similar advances in computing methods for evaluating the expected transition frequencies in three-body QED calculations. The comparison of experimental (ν_{exp}) and theoretical (ν_{th}) frequencies for seven transitions in $\bar{p}^4\text{He}^+$ and five in $\bar{p}^3\text{He}^+$ yielded an antiproton-to-electron mass ratio of $m_{\bar{p}}/m_e = 1836.152\,674(5)$. This agrees with the known proton-to-electron mass ratio at the level of $\sim 2 \times 10^{-9}$. The experiment also set a limit on any *CPT*-violating difference between the antiproton and proton charges and masses, $(Q_p - |Q_{\bar{p}}|)/Q_p \sim (m_p - m_{\bar{p}})/m_p < 2 \times 10^{-9}$ to a 90% confidence level. If on the other hand we assume the validity of the *CPT* invariance, the $m_{\bar{p}}/m_e$ result can be taken to be equal to m_p/m_e . This can be used as an input to future adjustments of fundamental constants. The hyperfine structure of a state in $\bar{p}^4\text{He}^+$ has also been measured by microwave spectroscopy to a precision of 3×10^{-5} . This corresponds to the accuracy of the most precise three-body QED calculations. Further increases in the experimental precision may soon yield an improvement in the value of the antiproton magnetic moment.

(Some figures in this article are in colour only in the electronic version)

This article was invited by Professor C Jarlskog.

⁴ Author to whom any correspondence should be addressed.

Contents

	Page
1. Introduction	1997
1.1. Particles and antiparticles	1997
1.2. <i>CPT</i> invariance and its possible violation—theoretical aspects	1998
1.3. Direct <i>CPT</i> tests at high and low energies	2001
1.4. Antihydrogen and antiprotonic helium atoms	2003
2. Exotic atom spectroscopy and particle-mass determination	2004
2.1. Exotic atoms, formation and cascade	2004
2.2. Determination of particle properties using exotic atoms	2005
2.3. Antiprotonic helium atoms	2007
2.4. Theoretical considerations	2009
3. Laser spectroscopy of antiprotonic helium $\bar{p}\text{He}^+$ atoms	2015
3.1. The Antiproton Decelerator at CERN	2016
3.2. Laser-induced annihilation spectroscopy	2019
3.3. First experiments at AD	2023
3.4. Collisional frequency shifts in the $\bar{p}\text{He}^+$ transitions	2030
3.5. The radiofrequency quadrupole decelerator	2032
3.6. Direct measurement of the transition frequencies of isolated $\bar{p}\text{He}^+$	2034
3.7. Higher precision: cw pulse-amplified laser locked to a frequency comb	2036
3.8. Parts-per-billion-scale laser spectroscopy of $\bar{p}\text{He}^+$	2040
4. The mass and charge of the antiproton	2042
4.1. Determination of the antiproton-to-electron mass ratio	2043
4.2. <i>CPT</i> constraints on the \bar{p} mass and charge	2046
5. The magnetic moment of the antiproton	2047
5.1. HF structure in laser transitions	2048
5.2. Laser-microwave-laser resonance method	2048
5.3. Experiment	2049
5.4. Results	2050
6. Future prospects	2054
6.1. Doppler-free two-photon laser spectroscopy of antiprotonic helium	2054
6.2. Microwave spectroscopy of antiprotonic helium	2055
6.3. Two-body antiprotonic helium ions	2057
7. Summary	2058
Acknowledgments	2060
References	2060

1. Introduction

Symmetries in particle physics are even more important than in chemistry or solid state physics. Just like in any theory of matter, the inner structure of the composite particles is described by symmetries, but in particle physics most of the phenomena, at least at laboratory energies, are deduced from the symmetries (or invariance properties) of the state equations or from symmetry violation: the conservation laws, the interactions and even the existence of particle masses (see, e.g. [1] for general references).

CPT invariance is one of the most important symmetries of Nature and for a long time nobody doubted its validity. However, at present several alternative theories have been developed and this increased the interest in experimental tests. The present review is devoted to the tests of *CPT* invariance using antiprotonic helium, a three-body system consisting of a helium nucleus, an antiproton and an electron. In this section we summarize the theoretical issues of *CPT* invariance and its possible violations and the available experimental tests.

Our aim is to present the most recent results of the field. Because of volume limitations we do not describe the historical development of antiprotonic helium studies: these were published in great detail in the review [2].

1.1. Particles and antiparticles

According to the Standard Model of elementary particles—which agrees with all available experimental evidence so far—the visible matter of our world consists of a few point-like elementary particles: spin $\frac{1}{2}$ fermions (quarks and leptons, see table 1) whereas all interactions are mediated by elementary integer-spin bosons.

The strongly interacting hadrons come in two varieties; mesons and baryons. Mesons are composed of a quark and an antiquark whereas the baryons are three-quark states.

All fermions have *antiparticles*, anti-fermions which have identical properties but with opposite charges. Due to the $U(1)$ symmetry of the equation of motion of fermions, the Dirac equation, the fermion current is a conserved quantity, one cannot create or destroy fermions alone; they form and disappear in fermion–antifermion pairs only. The positron mass is $511 \text{ keV}/c^2$, so in order to create an electron–positron pair one needs an energy above 1.022 MeV . This is the typical energy range of nuclear transitions and so for getting low energy positrons one can use an isotope with β^+ decay; frequently ^{22}Na is used in most positron sources. For a positron beam one can use higher energy electrons hitting a target and selecting the positrons from pair production. When positrons are slowed down and stopped in matter, they annihilate in flight or get bound to electrons or ions, trapped in cavities or coordinated in liquids. At the end they annihilate with electrons and emit two or three photons depending on the relative spin states of the particles.

The proton mass is $938 \text{ MeV}/c^2$; the creation of a proton–antiproton pair needs at least a 2 GeV energy deposit, so one needs a high-energy accelerator to get antiprotons. There are several such laboratories in Europe, the USA and Japan. At CERN antiprotons are produced in an iridium target at a $3.5 \text{ GeV}/c$ momentum, slow down in 3 steps in the Antiproton Decelerator ring to $100 \text{ MeV}/c$ at which they are delivered to the experiments.

The proton and antiproton are composite particles; the quark model describes several of their static properties (spin, magnetic moment, etc) as a bound state of three quarks (or antiquarks). However, the dynamic studies at high energies revealed that only half of the momentum of the proton or antiproton can be attributed to the constituent quarks; the rest is a cloud of gluons and virtual quark–antiquark pairs. This is, of course, also demonstrated by the masses: in the quark model the proton is described as a (uud) state and the masses of those

Table 1. The elementary fermions of the Standard Model. L stands for left: it symbolizes that in the weak isospin doublets left-polarized particles and right-polarized antiparticles appear; their counterparts constitute iso-singlet states. The apostrophes of down-type quarks denote their mixed states for the weak interaction.

	Fermion doublets ($S = 1/2$)	Charge Q	Isospin I
Leptons	$\begin{pmatrix} \nu_e \\ e \end{pmatrix}_L$, $\begin{pmatrix} \nu_\mu \\ \mu \end{pmatrix}_L$, $\begin{pmatrix} \nu_\tau \\ \tau \end{pmatrix}_L$	0 -1	+1/2 -1/2
Quarks	$\begin{pmatrix} u \\ d' \end{pmatrix}_L$, $\begin{pmatrix} c \\ s' \end{pmatrix}_L$, $\begin{pmatrix} t \\ b' \end{pmatrix}_L$	+2/3 -1/3	+1/2 -1/2

quarks are of the order of 10 MeV whereas the proton mass is 2 orders of magnitude higher. From this follows one of the mysteries of particle physics: how could such a complicated system produce exactly 1/2 spin?

Following from the composite structure of the proton, the proton–antiproton annihilation is also a complicated reaction. Once an antiproton is stopped in matter, it gets captured via Coulomb interaction in an atomic orbit and then is generally absorbed in a nucleus and annihilates in a very short time, usually within a femtosecond due to strong interaction. The proton–antiproton annihilation produces on average 4.5 energetic charged particles, predominantly pions as those are the lightest hadrons, emitted in all directions. This makes it relatively easy to build detectors for antiprotonic experiments as one does not have to cover the whole solid angle to have a detection efficiency of antiproton annihilation close to 100%.

The different abundances of particles and antiparticles in our Universe are one of the mysteries of astrophysics: apparently there is no antimatter in the Universe in significant quantities, see, e.g. [3]. If there were antimatter galaxies they would radiate antiparticles and we would see zones of strong radiation at their borders with matter galaxies, but astronomers do not see such a phenomenon anywhere.

1.2. CPT invariance and its possible violation—theoretical aspects

1.2.1. CPT invariance in field theory. Speaking in terms of Dirac theory an extremely interesting property of the free *antiparticles* is that they can be treated mathematically as if they were *particles* of the same mass and of oppositely signed charge of the same absolute value *going backward in space and time*. This is the consequence of one of the most important symmetries of Nature: CPT invariance [1, 4, 5]. It states that the following operations:

- charge conjugation C (i.e. changing particles into antiparticles),
- parity change P (i.e. the mirror reflection of space coordinates), and
- time reversal T ,

when performed simultaneously, do not change the measurable physical properties of the system.

CPT invariance is valid [4] within the framework of a local, unitary and Lorentz-invariant field theory in flat space–time. As the CPT operator is antiunitary, it relates the S -matrix of a process to that for the inverse process with all spin-components reversed and particles replaced by antiparticles. Of course, that does not mean that the same process will have the same probability, e.g. that a particle will decay with the same rate to the same final states as its antiparticle, but the sum of all partial decay rates, i.e. the lifetimes should be the same.

This means that the annihilation of a free positron with an electron can be described as if an electron came to the point of collision, irradiated two or three photons and then went out

backwards in space–time. Actually, the Feynman diagram technique assumes and uses *CPT* invariance and so all calculations in particle physics phenomenology should lose validity with the *CPT* symmetry disproved. Thus, the amazing agreement between the predictions of the Standard Model and the measured data also serves as an indirect proof of the *CPT* invariance.

Note that for parity reflection changing the signs of all three coordinate axes is equivalent to changing the sign of one, which results in, e.g. changing the polarization of a particle. A function has even parity if it does not change upon inverting its variable and odd if it keeps its absolute value but changes sign, i.e. acquires a factor of -1 . For instance, $f(x) = A \cos x$ has even whereas $f(x) = A \sin x$ has odd parity. Any function can be written as a sum of an odd and an even function in many ways, e.g. by polynomial or trigonometric expansion and grouping even and odd terms, or formally as

$$f(x) = \frac{1}{2}\{f(x) + f(-x)\} + \frac{1}{2}\{f(x) - f(-x)\}.$$

Parity seems to be a basic property of fields in particle physics. A field is even or odd if its sign changes appropriately at the space–time point of parity inversion. The electromagnetic and strong interactions conserve parity whereas the weak interaction maximally violates it. This violation of mirror symmetry is manifested by the fact that in weak interactions preferably left-polarized (i.e. polarized against their momenta) particles and right-polarized antiparticles (polarized along the momentum) are produced. When following the proposal of Lee and Yang [6] the experiments of Wu *et al* [7] and Lederman and co-workers [8] proved that weak interactions violated parity conservation Pauli exclaimed: ‘I cannot believe that God is left-handed’. This discovery has started a systematic test of all invariance principles which almost immediately resulted in discovering *CP* violation in weak interactions. Although as opposed to the maximality of parity violation, *CP* symmetry is violated very little, e.g. for the channel of its discovery, $K_L^0 \rightarrow \pi\pi$ on the level of 10^{-3} , it again forced the field to revise particle theory.

If we build a clock looking at its design in a mirror, it should work properly except that its hands will rotate the opposite way and the lettering will be inverted. The laws governing the work of the clock are invariant under space inversion, i.e. conserve parity. *CP* invariance seems to be even more plausible as that involves simultaneous space reflection and charge inversion. Unlike the other interactions, the weak interaction violates both parity and *CP* conservation; *CPT* invariance, however, is still assumed to be absolute in field theory. Returning to the example of the clock, a *P* reflection means switching left to right, a *C* transformation means changing the matter of the clock to antimatter and the time reversal *T* means that we play the video recording of the movement of the clock backwards.

Thus *CPT* invariance implies that particles and their antiparticles must have similar properties: the same mass and quantum numbers, the same absolute values with opposite signs of the charge-like quantities (electric charge, lepton and baryon number) and anti-colours for anti-quarks.

1.2.2. Possible alternatives versus experimental evidence. There are several ways to incorporate *CPT* violation in Standard Model extensions. Colladay and Kostelecký [9, 10] developed a general *CPT*-violating Hamiltonian which could be reduced to having a Lorentz violation for a free fermion but keeps the observer frame Lorentz-invariant. For a free fermion the generalized Dirac Lagrangian is [11]

$$\mathcal{L} = \frac{1}{2}i\bar{\psi}\Gamma^\nu\bar{\partial}_\nu\psi - \bar{\psi}M\psi, \quad (1)$$

where the generalized mass and γ -matrices are

$$M \equiv m + a_\mu\gamma^\mu + b_\mu\gamma_5\gamma^\mu + \frac{1}{2}H^{\mu\nu}\sigma_{\mu\nu} \quad (2)$$

and

$$\Gamma^{\nu} \equiv \gamma^{\nu} + c^{\mu\nu} \gamma_{\mu} + d^{\mu\nu} \gamma_5 \gamma_{\mu} + e^{\nu} + i f^{\nu} \gamma_5 + \frac{1}{2} g^{\lambda\mu\nu} \sigma_{\lambda\mu} \quad (3)$$

The partial derivation $\bar{\partial}$ is defined as $A\bar{\partial}^{\mu}B = A(\partial^{\mu}B) - (\partial^{\mu}A)B$, γ^{μ} are the Dirac-matrices and $\sigma^{\mu\nu} = \frac{i}{2}(\gamma^{\mu}\gamma^{\nu} - \gamma^{\nu}\gamma^{\mu})$.

Here all additional terms violate Lorentz invariance and those with a_{μ} and b_{μ} explicitly violate *CPT* invariance as well. The parameters $a_{\mu}, b_{\mu}, \dots, H^{\mu\nu}$ control the degree of Lorentz and *CPT* violation. As these terms are independent of the coordinate system, the system is Lorentz-invariant in the observer frame, but Lorentz-violating in the particle frame. We have not observed direct Lorentz-violation yet, so those parameters must be very small. The role of the various parameters is analyzed in [9, 10]. The stability and causality of this approach was discussed in many subsequent papers [12–14]. Note that Lorentz violation means dependence on the direction of movement in a fixed coordinate system.

Quantum gravity [15, 16] could cause fluctuations leading to Lorentz violation or loss of information in black holes which would mean unitarity violation. According to Mavromatos it is difficult to incorporate *CPT* invariance in quantum gravity. First of all, *CPT* invariance assumes flat space–time; it loses validity in highly curved ones such as in microscopic black holes [17] with Planck-sized, 10^{-35} m, event horizons. Such black holes could swallow information; thus unitarity could be violated leading to an evolution from pure to mixed quantum states and thus to decoherence, i.e. to *T* violation [18]. This is completely independent of a hypothetical Lorentz-violation. A quantum decoherence model was used to interpret both neutrino masses and dark energy in [19].

CPT invariance is so deeply embedded in field theory that many theorists claim it is impossible to test within the framework of present-day physics. Indeed, in order to develop *CPT*-violating models one has to reject fundamental axioms such as Lorentz invariance, the locality of interactions or unitarity [12, 14–16]. As shown by Greenberg [20] *CPT* violation in a unitary and local field theory implies violation of Lorentz invariance while the converse statement is not true: Lorentz violation does not necessarily lead to *CPT* violation. One does not willingly give up locality (i.e. causality), but unitarity or Lorentz-covariance, in principle, could be violated.

As far as we know, the Standard Model is valid up to the Grand Unification Theory (GUT) energy scale, $\sim 10^{16}$ GeV (which is somewhat below the Planck scale), as no available experimental evidence shows any significant deviation from it. Still, the Standard Model is a model, not a completely consistent theory, and it has some theoretical difficulties. The electroweak and colour interactions are deduced from local $U(1) \otimes SU(2) \otimes SU(3)$ gauge invariance requirements, and in order to make them work one has to introduce a spontaneously symmetry-breaking Higgs-field. However, gravity does not fit into this picture. We do not know why there are exactly three fermion families and which interaction causes the mixing of the neutrino types. The prevalence of matter against antimatter in the Universe and the left–right asymmetry of weak interactions is also unexplained and the Universe seems to be dominated by the mysterious dark matter and the even more mysterious dark energy. There are extensions of the Standard Model trying to explain these effects, but so far we have no experimental evidence supporting any of them in spite of great efforts of the particle physics community.

Above the Planck energy scale we may expect to have new physical laws which allow for Lorentz and *CPT* violation as well [12]. Quantum gravity [15, 16] could cause fluctuations leading to Lorentz violation or loss of information in black holes which would mean unitarity violation. Also, a quantitative expression of Lorentz and *CPT* invariance needs a Lorentz and *CPT* violating theory [12].

1.2.3. Neutrino oscillation and CPT violation. As mentioned above, the Standard Model cannot fully explain neutrino oscillation. Phenomenologically, the oscillations observed for solar and atmospheric neutrinos can be incorporated using two neutrino mass differences and a mixing matrix with three angles and a phase [5]. The *Liquid Scintillator Neutrino Detector (LSND)* experiment at Los Alamos found a strange excess of $\bar{\nu}_e$ in a $\bar{\nu}_\mu$ beam [21] which cannot be explained within the Standard Model with three neutrinos. For a Standard Model interpretation of the LSND results a fourth, sterile neutrino has to be introduced [5] as the studies of the invisible width of the Z boson allow for three lepton families in the Standard Model.

Several interpretations have been proposed to explain the LSND results based on *CPT*-violating models [19, 22–26]. The LSND Collaboration also proposed [27] an interpretation of this neutrino oscillation using an extension of the Standard Model with Lorentz and *CPT* violation of the order of 10^{-19} GeV. In 2007 the results of the *Minimal Booster Neutrino Experiment (MiniBooNE)* Collaboration [28] excluded the existence of sterile neutrinos.

Recently, the Kostelecký group developed a Lorentz-violating extension of the Standard Model [24] called the *tandem model* [29] which can explain all of observed neutrino oscillations using massive neutrinos in a Hamiltonian with Lorentz-violating terms. The tandem model is very attractive as (1) it does not need an additional kind of interaction, (2) it can account for all experimental data including the LSND result and (3) it needs only 3 parameters as opposed to the neutrino mass mixing of the Standard Model which introduces two mass differences and 4 mixing parameters.

There is another recent attempt by Barenboim *et al* [25] to interpret the neutrino oscillation data using a *CPT*-violating extension of the Standard Model. The neutrino mass difference is partially deduced from unitarity-violating quantum-gravity-induced decoherence. The model fairly reproduces the KAMLand and Super-Kamiokande results for $\nu_e \leftrightarrow \nu_\mu$ oscillations.

Klinkhamer [26] proposed a Lorentz-violating model for neutrino oscillations in vacuum which he successfully applied to the $\nu_e \leftrightarrow \nu_\mu$ oscillation data. He has shown that these oscillations may be *T* and *CP* invariant at low energies, but strongly *T* and *CP* violating at much higher ones.

In the papers [25–27, 29] several tests are proposed to check the models for neutrino oscillations in short- and long-baseline experiments.

1.3. Direct CPT tests at high and low energies

CPT invariance is so far fully supported by the available experimental evidence and it is absolutely fundamental in field theory. All of this is the best possible reason to test it as precisely as possible. There are many experiments aimed at doing that. In principle the simplest way is to compare the mass or charge of particles and antiparticles. However, as pointed out in [18] not all *CPT*-violating mechanisms imply such a difference between particle and antiparticle. Of course, on the other hand, an observation of such a difference should imply breaking the *CPT* invariance.

There are many experimental tests, none showing significant deviations from the *CPT* invariance; these are summarized in the recent reviews [5, 14, 17, 30].

Usually, the comparison of the masses of the neutral K meson and its antiparticle is considered to be the most precise such measurement: the relative difference $|m_{K^0} - m_{\bar{K}^0}|/\text{average}$ has been found to be less than 10^{-18} [5] on a 90% confidence level using kaon oscillation. However, the Dehmelt group [31] has shown that from their spin and cyclotron frequency studies performed with single electrons and positrons in a magnetic trap, by directly measuring the difference between the two frequencies, $\omega_a^\pm = \omega_s^\pm - \omega_c^\pm$, which is

proportional to the anomalous magnetic moment of the particles, a much lower *CPT* violation limit was obtained: $\hbar|\omega_a^+/2 - \omega_a^-/2|/(m_0c^2) < |3 \pm 12| \times 10^{-22}$ for the electron.

The TRAP group measured the charge/mass ratio of the proton and the antiproton at LEAR [32]. They kept a single antiproton and a single H^- ion in the same Penning-trap simultaneously at different orbits and measured their cyclotron frequencies. The measurements were performed at liquid helium temperature, in a magnetic field of $B = 5.85$ T and in an extremely high vacuum estimated to be about $p = 5 \times 10^{-17}$ Torr. While the particle at the lower orbit of $R \sim 350 \mu\text{m}$ was studied, the other one at a higher orbit of $R > 1.6$ mm was *parking* and waiting its turn. The orbits of the particles were switched by excitation. The cyclotron frequencies were found to be $\nu_c(p) = 1.001\,089\,218\,750(2)\nu_c(H^-)$. After having made corrections for the H^- - p deviation they limited the relative proton-antiproton charge/mass difference to $\kappa < (0.9 \pm 0.9) \times 10^{-10}$. Achieving this precision took 10 years of work. As shown by [33] this result should be corrected for a polarization frequency shift resulting in $\kappa < (1.6 \pm 0.9) \times 10^{-10}$. To date this is the most precise *CPT* test in the baryon sector. The theoretical issues of experiments with Penning traps are discussed in [34].

Hughes *et al* [35] have evaluated a test of *CPT* and Lorentz invariance from the microwave spectroscopy of muonium ($\text{Mu} = \mu^+e^-$). Hamiltonian terms beyond the Standard Model violating *CPT* and Lorentz invariance would contribute frequency shifts to the transitions involving muon spin flip, which were precisely measured in ground state muonium in a strong magnetic field of 1.7 T. The shifts would be indicated by anti-correlated oscillations at the Earth's sidereal frequency. No time dependence was found at the level of 20 Hz, limiting the size of some *CPT* and Lorentz-violating parameters at the level of 2×10^{-23} GeV.

Phillips *et al* [36] searched for a *CPT* and Lorentz-violation signature by monitoring the Zeeman frequency of hydrogen atoms in a static magnetic field using a hydrogen-maser double-resonance technique during the sidereal rotation of the laboratory reference frame. On the basis of these data and also using an earlier *CPT* and Lorentz constraint on the electron they limited a *CPT*-violating parameter for the proton to 2×10^{-27} GeV at the 1-sigma level. A similar test was made by Bear and co-workers [37, 38] for the neutron using a noble-gas laser limiting *CPT* and Lorentz violation to 10^{-27} GeV.

The BaBar [39] and Belle [40] experiments at B-factories used $B^0 - \bar{B}^0$ oscillations to limit the *CPT* violation in the B-meson sector. Following the proposal given in [41] the BaBar collaboration studied the variation of these oscillations as a function of sidereal time. If Lorentz invariance is violated, some measured reaction rates may depend on the absolute orientation of the experimental apparatus with the rotation of Earth. The analysis was performed using equation (1) where the term with a_μ violates both Lorentz and *CPT* invariances. a_μ is a constant vector with a frozen orientation in space-time, the possible variation of which is assumed to occur at a much larger length scale than the Earth (solar) scale. This may lead to its periodic sidereal variation. The BaBar experiment has found a 2.2σ difference in the period of 12 h in this *CPT* (and Lorentz) depending parameter. Although this deviation is statistically not significant, it should motivate further *CPT* studies.

CPT violation was also searched for in the cosmic microwave background (CMB) using the data collected by the Wilkinson Microwave Anisotropy Probe (WMAP) and by the Boomerang experiment [42]. If the Lorentz and *CPT* symmetries are broken by a term in the effective Lagrangian, which couples the dual electromagnetic field strength tensor to an external four-vector, the polarization vectors of propagating CMB photons will get rotated. The data seem to slightly favor (by 1.2σ) a non-zero rotation. A new interpretation [43] of the Boomerang results favors non-zero coefficients for the Lorentz-violating terms on the 1σ level. On the other hand, as shown by [44], assuming an energy dependent velocity of light in the form of $c(E) \sim c_0(1 - E/M)$ the Lorentz-violation energy scale M can be

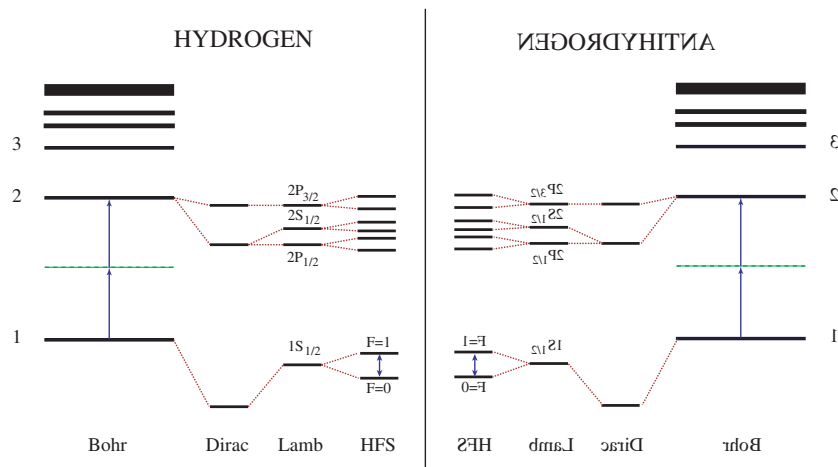


Figure 1. Atomic levels in hydrogen and antihydrogen. CPT symmetry requires them to be exactly equivalent. The 2S–1S two-photon transition and the ground-state hyperfine splitting (HFS) microwave transition are the best candidates for high-precision CPT tests.

limited to $M > 0.9 \times 10^{16}$ GeV using γ -ray bursts from the astrophysical sources of known red-shifts.

Note that antiproton gravity is not of this category. The CPT theorem only says that an apple should fall towards the Earth the same way as an anti-apple to anti-Earth; it is the weak equivalence principle which should make an anti-apple fall to the Earth the same way.

1.4. Antihydrogen and antiprotonic helium atoms

CERN constructed its *Antiproton Decelerator* facility (AD) [45] in 1999 in order to test the CPT invariance by comparing the properties of proton and antiproton and those of hydrogen and antihydrogen.

Antihydrogen, the bound system of an antiproton and a positron, is a very attractive subject for testing CPT invariance, as it is an anti-atom, which is shown to form, can be confined in a trap and is stable *in vacuo*. The extremely small line width (1.3 Hz) corresponding to the long lifetime of the metastable 2S state makes the 2S–1S transition (figure 1) a promising candidate for high-precision measurements; a Doppler-free excitation is possible in the case of absorption of two photons from opposite directions. This transition has been recently measured in hydrogen with a precision of 1.8×10^{-14} [46]. However, as shown in [47] the 1S and 2S states of the same spin configuration in hydrogen and antihydrogen have identical leading-order energy shifts and thus no leading order spectroscopic 1S–2S signal is expected for Lorentz or CPT violation in free hydrogen or antihydrogen. At the same time studying hyperfine transitions in hydrogen and antihydrogen confined in a magnetic trap is most promising from a theoretical perspective.

Although some antihydrogen atoms have been successfully produced by two collaborations at the AD, ATHENA [48] and ATRAP [49], the high hopes promised by antihydrogen spectroscopy have not yet been realized. The goals of the ongoing efforts are to make antihydrogen atoms in the ground state (none has been positively identified) and magnetically trap them, both being the prerequisites for high-precision spectroscopy.

Another system studied at the AD, by the ASACUSA (Atomic Spectroscopy And Collisions Using Slow Antiprotons) Collaboration, is the antiprotonic helium atom. It is

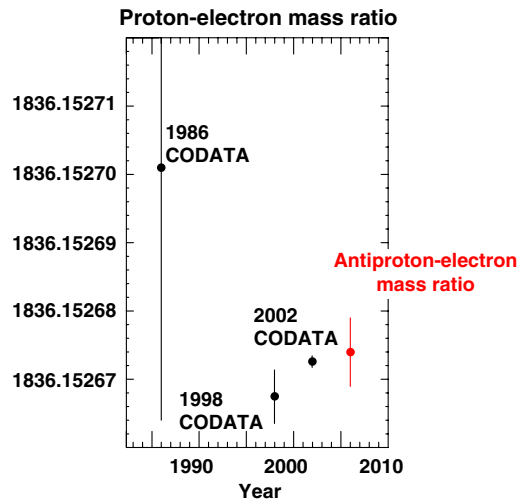


Figure 2. Proton-to-electron [50] and antiproton-to-electron [51] mass ratios.

sufficiently stable to be an object of precision spectroscopy and sufficiently simple to have its energy spectra calculated with very high precision. As shown in figure 2, which compares the recent result of the antiproton-to-electron mass ratio obtained by $\bar{p}\text{He}^+$ laser spectroscopy [51] with the CODATA (Committee on Data for Science and Technology) values for the proton-to-electron mass ratio [50], the mass equality of proton to antiproton (i.e. *CPT*) has been tested at the level of 10^{-9} using antiprotonic helium atom spectroscopy. If we assume on the other hand the validity of the *CPT* invariance, the antiproton result can be combined with m_p/m_e to provide a more precise value for the proton-to-electron mass ratio.

CPT studies performed on this atomic state is the subject of this review. Section 2 overviews the formation and decay processes of antiprotonic helium atoms. Section 3 is devoted to the technical aspects of the laser spectroscopy performed on antiprotonic helium. Section 4 describes the state of art of determining the mass and charge of the antiproton using the spectroscopic results. Section 5 describes the efforts and results of measuring the magnetic moment of the antiproton using the laser-microwave-laser triple resonance method. Section 6 summarizes the expected developments of the subject: two-photon spectroscopy to reduce Doppler broadening, improved microwave technique and spectroscopy of the two-body antiprotonic helium ion. Section 7 provides a summary of the review.

2. Exotic atom spectroscopy and particle-mass determination

2.1. Exotic atoms, formation and cascade

Exotic atoms denote systems in which a heavy negatively charged particle ' X^- ' (e.g. antiproton, see table 2) is bound by the Coulomb force to the nucleus. The atoms formed by a positive particle and an electron (such as positronium, $\text{Ps} = e^+e^-$, or muonium, $\text{Mu} = \mu^+e^-$) also belong to the family of exotic atoms and, owing to the wide applications of positron annihilation and muon spin research in solid state physics and chemistry, their study is much more intensive than that of exotic atoms with negative particles. Also, the physical processes are quite different for exotic atoms with negative and positive particles. In this review we shall treat exotic atoms with negative particles only.

Table 2. Properties of *exotic* particles as compared with those of the electrons. The strongly interacting particles, the integer spin *mesons* and the half-integer spin *baryons*, are together called *hadrons*. The data are taken from [5].

Particle	Spin (\hbar)	Lifetime (s)	m_X/m_e	mc^2 (MeV)	Class
e^-	1/2	∞	1	0.511	Lepton
μ^-	1/2	2.197×10^{-6}	207	105.7	Lepton
π^-	0	2.603×10^{-8}	273	139.6	Meson
K^-	0	1.237×10^{-8}	966	493.6	Meson
\bar{p}	1/2	∞	1836	938.3	Baryon
Σ^-	1/2	1.48×10^{-10}	2343	1197.4	Baryon

The importance of the Coulomb attraction between negatively charged mesons and atomic nuclei was recognized by Araki and Tomonaga already in 1940 [52], who studied the absorption of slow mesons in matter and argued that the negative mesons should be much more likely to be captured by nuclei than to decay freely, while practically all positive mesons should undergo spontaneous disintegration. Subsequently, Fermi and Teller [53], Wightman [54] and others established that the nuclear capture of slow mesons is preceded by the exotic-atom formation and cascade processes.

When a negatively charged particle X^- is injected into matter, it continues to lose energy by ionization until its kinetic energy T falls below the ionization energy I of the stopping material. The initial capture of the negatively charged particle X^- is expected to occur [53, 54] at

$$n \sim n_0 = \sqrt{\frac{M_X^*}{m_e^*}}, \quad (4)$$

where n is the principal quantum number of the initial-capture orbit and M_X^* and m_e^* respectively, are the reduced masses of the X^- -nucleus and the electron–nucleus systems. In the case of antiproton, the capture occurs at around $n \sim \sqrt{1800} \sim 40$. The atomic capture process is followed by various cascade (deexcitation) mechanisms as schematically illustrated in figures 3 and 4, where figure 3 is for μ^- atoms while figure 4 is for the low-lying levels of the $\bar{p}\text{He}$ atom.

Auger transitions prevail in the initial stage of the cascade, while the radiative transitions become dominant in the later stage. If the particle is strongly interacting as in the case of antiproton, the strong-interaction effects become non-negligible for small n and/or small ℓ orbits, inducing the shift of binding energies of those low-lying states as well as broadening of the level widths (figure 4).

Another important effect contributing to the cascade of exotic atoms is the Stark mixing. This is particularly important for X^- capture in H_2 and He targets [55]. When for instance the X^- -p atom is formed and moves in the H_2 target, the atom is subject to oscillating electric fields, which induce Stark mixing among levels of the same n but different ℓ . The Stark mixing has the effect of redistributing the level population according to the statistical weight $2\ell + 1$, erasing the ‘memory’ of the primordial ℓ distribution. As shown by [56] when X^- is a strongly interacting particle such as \bar{p} , nuclear absorption and subsequent annihilation can occur for high- n S-states and so the Stark mixing can induce nuclear absorption even for large- n , large- ℓ states, which would otherwise survive for a long time avoiding nuclear interaction.

2.2. Determination of particle properties using exotic atoms

Spectroscopy of exotic atoms offers a powerful tool to study fundamental interactions as well as particle properties. For example, the masses of π^\pm [57] and K^\pm [58, 59] as listed in the

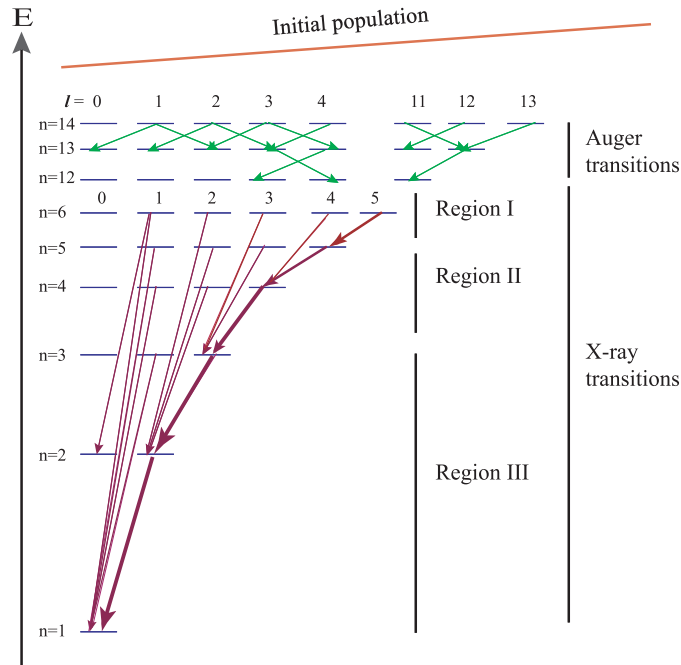


Figure 3. Deexcitation of a muonic atom. From highly excited states Auger transitions prevail, in the lower region x-ray emission. The x-ray region can be divided into three subregions: (I) strong electron screening effect, (II) low electron screening, negligible nuclear interaction, and (III) interaction with the nucleus.

review of particle physics [5] were determined using exotic-atom x-ray transitions, and the ‘CPT theorem’ discussed in the previous section was used to assign the same values to the mass of their antiparticles.

In those measurements, particle masses were determined by noting that the transition energy ΔE from the state (n, ℓ) to (n', ℓ') can be written as

$$\Delta E_{n,\ell \rightarrow n',\ell'} = Rhc \frac{m_X^*}{m_e} Z^2 \left(\frac{1}{n'^2} - \frac{1}{n^2} \right), \quad (5)$$

wherein R denotes the Rydberg constant, h the Planck constant, c the speed of light, m_X^*/m_e the reduced ‘ X^- ’-to-electron mass ratio and Z the nuclear charge. For the sake of simplicity we here adopted the Bohr model and ignored the nuclear charge screening by the electron(s) which in general can be still present when x-rays are emitted (see figure 3).

The situation is different for the proton, since the proton mass rather than the antiproton mass can be more precisely determined using Penning traps. The 1998 CODATA recommended value [60] for m_p/m_e of 1836.152 6675(39) (relative standard uncertainty of 2.1×10^{-9}), was based on the measurement conducted by the University of Washington group [61], who compared the cyclotron frequencies $\omega_c = qB/m$ of a single C^{6+} ion and a single electron trapped in a Penning trap, i.e. the determination of the electron mass in units of the atomic mass unit). This was then combined with their comparison of the cyclotron frequencies of a single proton and a single C^{4+} ion [62], yielding the m_p/m_e value.

The 2002 CODATA recommended value [50] for m_p/m_e of 1836.152 672 61(85) (relative standard uncertainty of 4.6×10^{-10}) was based on a new measurement carried out by the GSI-Mainz collaboration [63], who compared the $^{12}C^{5+}$ cyclotron frequency and its spin

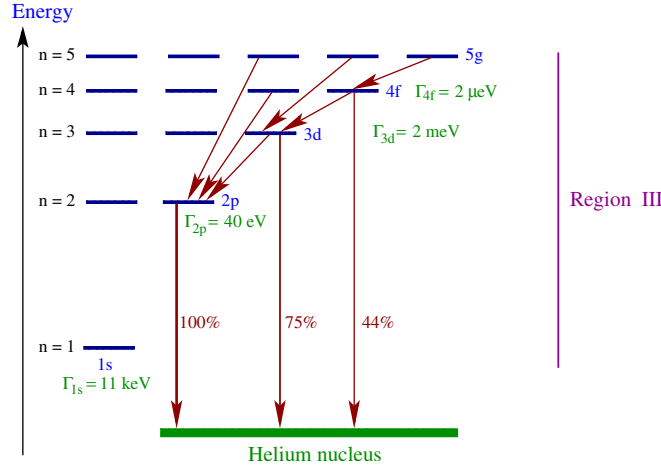


Figure 4. Deexcitation of the low-lying levels of the antiprotonic helium atom. For the highly excited states see figure 3. In the lower x-ray region strong interaction with the nucleus shifts and broadens the states with low orbital momentum, there is strong nuclear absorption from the lowest states, so that the 1s state is practically not populated. Γ is the level width. The probabilities of nuclear absorption are also shown for the lowest circular antiprotonic states.

precession frequency $\omega_L = geB/(2m_e)$. From the measured ratio ω_c/ω_L and the quantum-electrodynamical (QED) prediction for the bound-electron g factor, the electron's mass in units of the atomic mass unit was obtained. The proton mass values thus obtained are much more precise than the antiproton mass value obtained by the antiprotonic atom x-ray measurements (having relative uncertainties of $\sim 4 \times 10^{-5}$) [64]. The advent of antiprotonic helium atom laser spectroscopy has made it possible to improve this by more than four orders of magnitude.

In addition to the particle mass, the magnetic moment μ of a fermion can be determined from the fine or hyperfine splitting of exotic atoms. In the case of the muon, the most precise value for the muon-to-proton magnetic moment ratio came from the hyperfine splitting of muonium (μ^+e^-) [65] before a higher accuracy was achieved in a storage ring. For other elementary particles such as the Σ^- [66] and the antiproton [67], μ was determined from the fine structure, i.e. the spin-orbit splitting which in the case of the antiproton is given by

$$\Delta E_{LS}(n, l) = (1 + 2\kappa) \frac{Mc^2}{2} \frac{(Z\alpha)^4}{n^3 l(l+1)}, \quad (6)$$

where the anomalous magnetic moment of the antiproton is defined by

$$\mu_{\bar{p}} = -(1 + \kappa)\mu_N, \quad (7)$$

with $\mu_N = e\hbar/(2m_p)$ being the nuclear magneton, e the elementary charge and m_p the proton mass.

2.3. Antiprotonic helium atoms

The serendipitous discovery of metastable antiprotonic helium atoms [2,68] was soon followed by the advent of laser spectroscopic techniques [69,70], and after about 10 years of continuous improvements, it has now become possible to deduce the antiproton mass nearly as precisely as that of the proton [51]. Current experiments are being carried out by the ASACUSA at CERN's Antiproton Decelerator facility (AD). High-precision determination of the \bar{p} mass

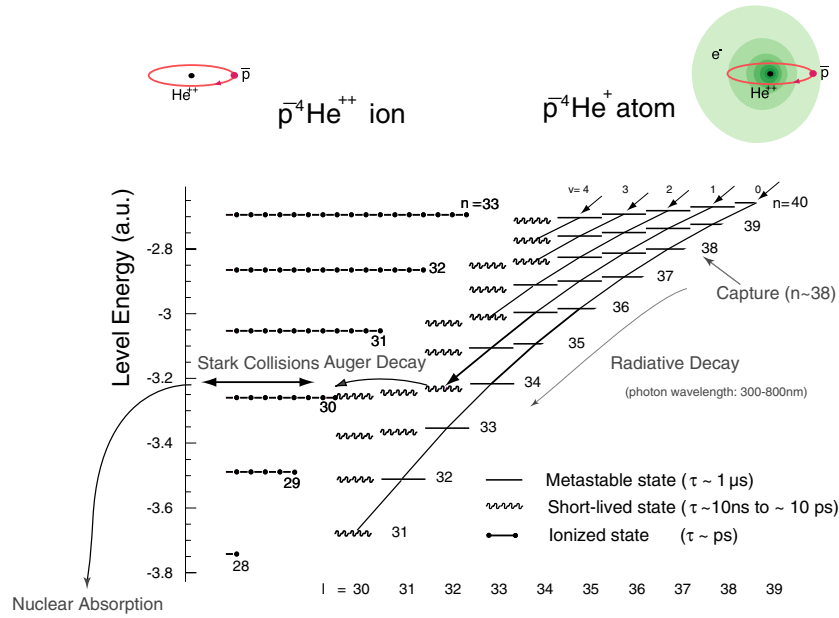


Figure 5. Level diagram of $\bar{p}^4\text{He}^+$ in relation to that of $\bar{p}^4\text{He}^{++}$. The continuous and wavy bars stand for metastable and short-lived states, respectively, and the dotted lines are for l -degenerate ionized states.

using the laser spectroscopy of antiprotonic helium is the main subject of this review, and we present here a brief outline of the method involved and the results obtained.

Normally, when an antiproton is stopped in matter, the antiproton annihilates on a nucleus within picoseconds, leaving no time for high-precision laser spectroscopy. The only exception is known to occur in helium [2], due to the formation of the antiprotonic helium atom, i.e. a neutral three-body system comprising an antiproton, a helium nucleus and an electron (hereafter denoted $\bar{p}\text{He}^+$). $\bar{p}\text{He}^+$ is a naturally occurring antiproton trap in which an antiproton can be ‘stored’ for several microseconds, and its partial energy diagram is depicted in figure 5.

When the antiproton is located in a near-circular ($n \approx 38$, $l \geq 35$) orbit of a neutral $\bar{p}\alpha e^-$ atom, those states from which Auger transitions are suppressed due to high angular momentum exchange ($\Delta l > 3$) will become metastable as the electron removes the l -degeneracy of the levels with the same principal quantum number n thereby preventing fast Stark-transitions and also screens to some extent the $\bar{p}\alpha$ system from collisional deexcitation. The levels indicated by the continuous lines in figure 5 have metastable ($\gtrsim 1 \mu\text{s}$) lifetimes and deexcite radiatively, while the levels shown by wavy lines are short lived ($\lesssim 10 \text{ ns}$) and deexcite by Auger transitions to antiprotonic helium ion states (shown by dotted lines). While the radiative rates Γ_{rad} depend only weakly on the orbital quantum number l , at least around the circular states as discussed here, the Auger rates Γ_{Aug} increase sharply towards smaller l . A rule of thumb is if the angular momentum change Δl of the Auger transition is large ($\Delta l \geq 4$), the Auger transition rate is slower than the radiative ($\Gamma_{\text{Aug}} < \Gamma_{\text{rad}}$), making such states metastable. For lower Auger multipolarities ($\Delta l \leq 3$), the Auger rate Γ_{Aug} dominates, making such states short lived.

The possible existence of these metastable antiprotonic helium atoms had been theoretically predicted by Condo and Russell [71–75] 20 years before it was experimentally discovered [68] at the 12 GeV proton synchrotron of KEK, Japan. Since then they have been studied in detail at the Low Energy Antiproton Ring (LEAR) at CERN [2]. These studies

revealed the following remarkable features of $\bar{p}\text{He}^+$ atoms.

- (i) The $\bar{p}\text{He}^+$ atoms can be abundantly produced just by stopping antiprotons in a helium target. Then, about 3% of the stopped antiprotons automatically become trapped in the metastable states.
- (ii) The antiproton in the metastable orbits deexcite, initially, via radiative transitions, following a propensity rule of $\Delta n = -1$, $\Delta v = 0$, where $v = n - \ell - 1$ is the so-called vibrational quantum number. Once the antiproton reaches an Auger-dominated state, the one-remaining electron is ejected, producing an antiprotonic helium ion ($\bar{p}\text{He}^{2+}$). Since the ionic states are hydrogenic, Stark collisions quickly induce antiproton annihilation on the helium nucleus, as indicated in the left part of figure 5.
- (iii) The level spacings between the metastable states connected by electric dipole ($E1$) transitions, $(n, \ell) \rightarrow (n - 1, \ell - 1)$ as well as $(n, \ell) \rightarrow (n + 1, \ell - 1)$, are in the optical frequency region, making it possible to force transitions between those levels by laser irradiation. Note that we are not changing the electronic state as in ordinary atomic spectroscopy, but are inducing transitions between different antiproton orbits.
- (iv) The $\bar{p}\text{He}^+$ atoms are initially produced at epithermal energies, but they then collide with the surrounding helium atoms and become thermalized. If a low-temperature ($T \sim 10$ K) helium gas target is used, the thermalized $\bar{p}\text{He}^+$ atoms are well suited for high-precision spectroscopy (i.e. small Doppler width).

2.4. Theoretical considerations

2.4.1. Non-relativistic treatment. The laser spectroscopy of $\bar{p}\text{He}^+$ atoms determines the transition frequencies between (n, ℓ) and (n', ℓ') levels, which depends on the antiproton-to-electron mass ratio as

$$\nu_{n,\ell \rightarrow n',\ell'} = Rc \frac{m_{\bar{p}}^*}{m_e} Z_{\text{eff}}^2(n, \ell, n', \ell') \left(\frac{1}{n'^2} - \frac{1}{n^2} \right). \quad (8)$$

This is of course a simplified view, without relativistic, QED and spin effects. These effects are perturbatively treated, as are discussed later. If the system was a two-body antiprotonic helium ion, the nuclear charge Z is just 2, and hence calculating transition frequencies would be rather trivial. In the case of $\bar{p}\text{He}^+$, the effective nuclear charge Z_{eff} is less than 2 due to the charge screening by the remaining electron, and state-of-the-art three-body calculations are necessary.

It is in fact a non-trivial task to obtain the eigenenergies of three-body systems with better-than-ten-digit accuracies, but there are several issues which make the treatment of the antiprotonic helium atoms particularly difficult: (i) the total angular momentum is as high as ~ 40 , (ii) the excited states are not true bound states but are Feshbach resonances, (iii) the antiproton–electron correlation must be accurately taken into account, and (iv) adiabatic treatment is not appropriate when \bar{p} comes close to the helium nucleus.

The system can be either regarded as a molecule-like heavy–heavy–light two-center problem (but with one of the two centers having a negative charge) [76–79] or as an atom-like system (but with an ordinary and a ‘heavy’ electron) [80–82]. For this reason, $\bar{p}\text{He}$ was often called the *atomcule*. Note that the use of a molecular picture is appropriate when the \bar{p} orbital angular momentum is large, since the combined Coulomb-centrifugal potential for such states look similar to the Morse potential. Kino *et al* [83, 84] took three rearrangement channels (molecular channel, atomic channel and $\bar{p} - e^-$ correlation channel) and used a Gaussian expansion method. Most calculations solved the Schrödinger equation variationally, while a

finite-element method was also used [85]. We describe here the method of Korobov in some detail, which has so far attained the highest precision [81].

By using the coordinate system centered on the helium nucleus (atomic base), the non-relativistic Hamiltonian in atomic units can be written as

$$H_0 = -\frac{1}{2\mu_{12}}\nabla_1^2 - \frac{1}{2\mu_{13}}\nabla_2^2 - \frac{m_3}{m_1}\nabla_1\nabla_2 + \frac{z_1z_2}{r_{12}} + \frac{z_1z_3}{r_{13}} + \frac{z_2z_3}{r_{23}} \quad (9)$$

$$= -\frac{1}{2\mu_{12}}\nabla_{\mathbf{R}}^2 - \frac{1}{2\mu_{13}}\nabla_{\mathbf{r}}^2 - \frac{m_3}{m_1}\nabla_{\mathbf{R}}\nabla_{\mathbf{r}} - \frac{2}{R} - \frac{2}{r} + \frac{1}{|\mathbf{R}-\mathbf{r}|}, \quad (10)$$

$$\mu_{ij}^{-1} \equiv m_i^{-1} + m_j^{-1},$$

wherein the indices 1, 2 and 3, respectively, correspond to He, \bar{p} and e^- , while \mathbf{R} and \mathbf{r} are the position vectors of \bar{p} and e^- relative to the helium nucleus.

The wavefunction of a state of total angular momentum L and parity λ can be written as

$$\Psi_M^{L\lambda}(\mathbf{R}, \mathbf{r}) = \sum_{\ell+\ell_e=L} R^\ell r^{\ell_e} \{Y_\ell \otimes Y_{\ell_e}\}_{LM} G_{\ell\ell_e}^{L\lambda}(R, r, \theta), \quad (11)$$

where M is the z component of L , ℓ is the \bar{p} orbital angular momentum and ℓ_e is the electron angular momentum. Here $G_{\ell\ell_e}^{L\lambda}(R, r, \theta)$ can be expanded as

$$G_{\ell\ell_e}^{L\lambda}(R, r, \theta) = \sum_{i=1}^{\infty} C_i e^{-\alpha_i R - \beta_i r - \gamma_i |\mathbf{R}-\mathbf{r}|}. \quad (12)$$

where α_i , β_i and γ_i are complex parameters generated in a quasirandom manner [79].

As discussed above, the states which decay to the Auger daughter level with multipolarity $\Delta\ell \geq 4$ have microsecond-scale radiative lifetimes ($\sim 10^{-12}$ a.u.), and hence the Feshbach-type closed-channel solutions have high accuracies. On the other hand, the states having Auger-transition multipolarity of $\Delta\ell = 3$ have nanosecond-scale lifetimes ($\sim 10^{-8}$ – 10^{-9} a.u.), for which the wavefunction obtained within the closed-channel approximation have a relative accuracy of $\sim 10^{-4}$. This is insufficient for high-precision evaluation of relativistic and QED corrections.

To overcome this difficulty, all recent high-precision calculations employ the complex-coordinate-rotation (CCR) method [86], first introduced in the $\bar{p}\text{He}^+$ precision calculations by Kino *et al* [84]. The CCR is a powerful method to uncover resonant poles embedded in the continuum spectrum, by transforming the Hamiltonian with an operator $U(\alpha, \theta)$, which applies *complex scaling* $\mathbf{r} \rightarrow \alpha e^{i\theta} \mathbf{r}$ to the coordinates, wherein α and θ are real and positive. The complex-rotated Hamiltonian and the corresponding wavefunction are

$$H(\alpha, \theta) = U(\alpha, \theta) H U^{-1}(\alpha, \theta) \text{ and} \quad (13)$$

$$\Psi(\alpha, \theta) = U(\alpha, \theta) \Psi. \quad (14)$$

The resonance energy is determined by solving the complex eigenvalue problem for the rotated Hamiltonian,

$$(H(\alpha, \theta) - E)\Psi(\alpha, \theta) = 0. \quad (15)$$

An example of trajectories of the complex eigenvalues $E = \Re(E) + i\Im(E) = E_r - i\Gamma/2$ for different scaling parameters, α and θ , is shown in figure 6. As shown, trajectories converge to reveal a resonant pole. The position of the resonance can be determined by requiring the paths to be stationary ($\partial E/\partial\theta = \partial E/\partial\alpha = 0$). Korobov, using the quadruple-precision arithmetic, showed that non-relativistic energies as well as mean values of the delta-function operators, e.g. $\langle\delta(\mathbf{r}_i)\rangle$ stably converged by taking some 3500 basis sets [82]. Kino *et al* who used the double-precision arithmetic on a supercomputer and took a combination of the three rearrangement channels demonstrated convergence with about 7000 basis sets [87].

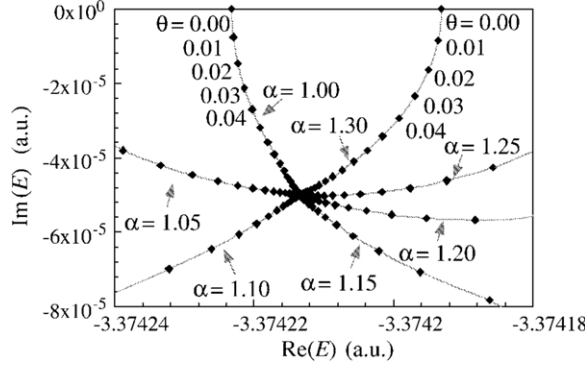


Figure 6. Complex eigenenergy trajectories [84] for the $(n, \ell) = (33, 30)$ state of $\bar{p}^4\text{He}^+$.

Table 3. Contributions from different relativistic and QED corrections (in atomic units) to the $(39, 35) \rightarrow (38, 34)$ transition of $\bar{p}^4\text{He}^+$ [82, 89].

ΔE_{nr}	=	501 972 347.9
ΔE_{rc}	=	-27 526.1
ΔE_{ae}	=	233.3
ΔE_{se}	=	3818.1
ΔE_{vp}	=	-122.5
ΔE_{kin}	=	37.3
ΔE_{exch}	=	-34.7
$\Delta E_{\text{recoil}}^{(3)}$	=	0.8
$\Delta E_{\text{two-loop}}$	=	0.9
ΔE_{nuc}	=	2.4
ΔE_{α^4}	=	-2.6
ΔE_{total}	=	501 948 754.9(1.3)(0.5)

2.4.2. Relativistic and QED corrections. After solving the non-relativistic Hamiltonian (11), relativistic [78] and quantum-electrodynamical [85, 88] corrections are perturbatively applied.

Table 3 shows an example of the breakdown of various terms contributing to the $(39, 35) \rightarrow (38, 34)$ transition of $\bar{p}^4\text{He}^+$ [81]. Here,

ΔE_{nr} is the non-relativistic part ($E_r^{(39,35)} - E_r^{(38,34)}$) obtained by solving the complex eigenvalue problem)

ΔE_{rc} is the relativistic correction for the bound electron

$$E_{\text{rc}} = \alpha^2 \left\langle -\frac{\nabla_3^4}{8m_3^3} + \frac{1}{8m_3^2} [z_1 4\pi \delta(\mathbf{r}_1) + z_2 4\pi \delta(\mathbf{r}_2)] \right\rangle, \quad (16)$$

ΔE_{ae} is the anomalous magnetic moment correction for the bound electron

$$\Delta E_{\text{ae}} = \alpha^2 \left\langle \frac{2a_3}{8m_3^2} [z_1 4\pi \delta(\mathbf{r}_1) + z_2 4\pi \delta(\mathbf{r}_2)] \right\rangle, \quad (17)$$

where a_3 is the anomalous magnetic moment of the electron,

ΔE_{se} is the one-loop self-energy correction

$$\Delta E_{\text{se}} = \alpha^3 \frac{4z_i}{3m_3^2} \langle \delta(\mathbf{r}_i) \rangle \left\{ \left[\ln \frac{1}{\alpha^2} - \beta + \frac{5}{6} - \frac{3}{8} \right] + (z_i \alpha) 3\pi \left(\frac{139}{128} - \frac{1}{2} \ln 2 \right) - \frac{3}{4} (z_i \alpha)^2 \ln^2 \frac{1}{(z_i \alpha)^2} \right\}, \quad (18)$$

where $\beta = \ln k_0(n)/R_\infty$ is the Bethe logarithm of the three-body state [90], ΔE_{vp} is the one-loop vacuum polarization

$$\Delta E_{\text{vp}} = \frac{4z_i\alpha^3}{3m_3^2} \left[-\frac{1}{5} + (z_i\alpha)\pi \frac{5}{64} \right] \langle \delta(\mathbf{r}_i) \rangle, \quad (19)$$

ΔE_{kin} is the relativistic corrections for heavy particles

$$\Delta E_{\text{kin}} = \alpha^2 \left\langle -\frac{\nabla_1^4}{8m_1^3} - \frac{\nabla_2^4}{8m_2^3} + \frac{(1+2a_2)z_2}{8m_2^2} 4\pi \delta(\mathbf{r}_2) \right\rangle, \quad (20)$$

where a_2 is the anomalous magnetic moment of the antiproton, ΔE_{exch} is the transverse photon exchange correction of the leading order α^2

$$\Delta E_{\text{exch}} = -\alpha^2 \frac{z_i}{2m_i m_3} \left\langle \frac{\nabla_i \nabla_3}{r_i} + \frac{\mathbf{r}_i (\mathbf{r}_i \nabla_i) \nabla_3}{r_i^3} \right\rangle, \quad (21)$$

ΔE_{nuc} is the finite nuclear size corrections

$$\Delta E_{\text{nuc}} = \frac{2\pi z_i (R_i/a_0)^2}{3} \langle \delta(\mathbf{r}_i) \rangle, \quad (22)$$

where R_i is the root-mean-square radius of the nuclear charge distribution, $\Delta E_{\text{recoil}}^{(3)}$ is the transverse photon exchange correction of order α^3

$$\Delta E_{\text{recoil}}^{(3)} = \frac{z_i\alpha^3}{m_i m_3} \left\{ \frac{2}{3} \left(-\ln \alpha - 4\beta + \frac{31}{3} \right) \langle \delta(\mathbf{r}_i) \rangle - \frac{14}{3} \langle Q(\mathbf{r}_i) \rangle \right\}, \quad (23)$$

where $Q(r)$ is the so-called Araki–Sucher term [91, 92], $\Delta E_{\text{two-loop}}$ is the two-loop QED corrections

$$\Delta E_{\text{two-loop}} = \alpha^4 \frac{z_i}{m_3^2 \pi} \left[-\frac{6131}{1296} - \frac{49\pi^2}{108} + 2\pi^2 \ln 2 - 3\zeta(3) \right] \langle \delta(\mathbf{r}_i) \rangle \quad (24)$$

and

ΔE_{α^4} is the order- α^4 relativistic correction (with an estimated accuracy of $\sim 10\%$),

$$\Delta E_{\alpha^4} \approx -\alpha^4 \frac{\pi}{2} \delta(\mathbf{r}_1). \quad (25)$$

The total transition energy ΔE_{total} is shown with two errors, the first being the uncertainty due to as yet uncalculated contributions of order $\alpha^5 \ln \alpha$ and higher, while the second being the numerical uncertainty.

Theoretical [82] as well as experimental [51, 93–95] precisions have improved over the years, as shown in figure 7. The theory improved by adding higher QED correction terms, and by improving the numerical precision in solving the non-relativistic Hamiltonian. The progress of experimental methods will be discussed in section 3.

2.4.3. Hyperfine splitting of the antiprotonic states. The levels of antiprotonic helium labelled by the principal quantum number n and the total angular momentum quantum number l exhibit a splitting which originates from the magnetic moments associated with the electron spin S_e , the antiproton orbital angular momentum $L_{\bar{p}}$ and the antiproton spin $S_{\bar{p}}$. The electron, which is predominantly in its ground state (hence $l = L$), has a magnetic moment given by its spin magnetic moment $\boldsymbol{\mu}_e = g_e \mu_B \mathbf{S}_e$. The antiproton magnetic moment consists of an orbital and a spin part $\boldsymbol{\mu}_{\bar{p}} = [g_\ell^{\bar{p}} L_{\bar{p}} + g_s^{\bar{p}} S_{\bar{p}}] \mu_N$, $g_\ell^{\bar{p}}$ and $g_s^{\bar{p}}$ being the corresponding orbital and spin g -factors. Because of the large angular momentum of \bar{p} in metastable states, the \bar{p} orbital

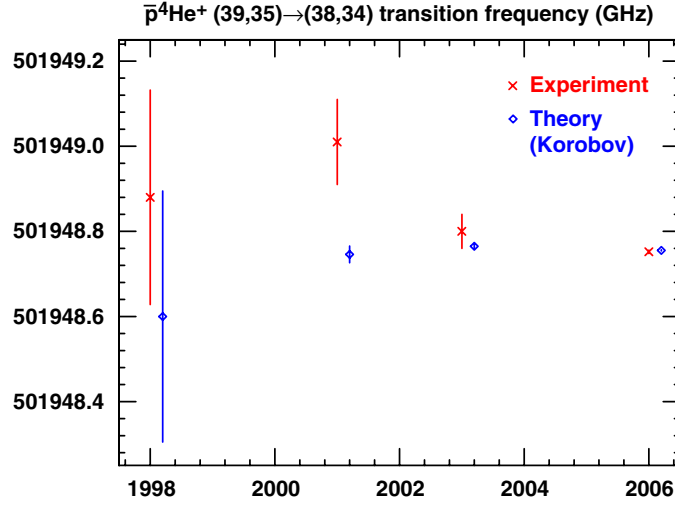


Figure 7. Comparison of measured and calculated transition frequencies for the (39, 35) \rightarrow (38, 34) transition of $\bar{p}^4\text{He}^+$.

magnetic moment is much larger than the spin one, and the angular momentum coupling scheme proceeds as follows:

$$\begin{aligned} \mathbf{F} &= \mathbf{L}_{\bar{p}} + \mathbf{S}_{\bar{e}}, \\ \mathbf{J} &= \mathbf{F} + \mathbf{S}_{\bar{p}} = \mathbf{L}_{\bar{p}} + \mathbf{S}_{\bar{e}} + \mathbf{S}_{\bar{p}}. \end{aligned} \quad (26)$$

Figure 8 (left) shows the resulting hyperfine splitting of $\bar{p}^4\text{He}^+$. The dominant splitting arising from the interaction of the antiproton angular momentum and the electron spin leads to a splitting into a doublet F^+ and F^- and is called a *hyperfine* (HF) splitting. The antiproton spin leads to a further, smaller splitting into a quadruplet J^{++} , J^{+-} , J^{-+} and J^{--} called *superhyperfine* (SHF) splitting.

In the case of $\bar{p}^3\text{He}^+$, each level splits into an octet as shown in figure 8 (right), due to an additional coupling to the ^3He (helion) nuclear spin \mathbf{S}_h [96]:

$$\begin{aligned} \mathbf{F} &= \mathbf{L}_{\bar{p}} + \mathbf{S}_{\bar{e}} \\ \mathbf{G} &= \mathbf{F} + \mathbf{S}_h = \mathbf{L}_{\bar{p}} + \mathbf{S}_{\bar{e}} + \mathbf{S}_h \\ \mathbf{J} &= \mathbf{G} + \mathbf{S}_{\bar{p}} = \mathbf{L}_{\bar{p}} + \mathbf{S}_{\bar{e}} + \mathbf{S}_h + \mathbf{S}_{\bar{p}}. \end{aligned} \quad (27)$$

Although the helion magnetic moment is smaller than the antiproton one, its overlap with the electron cloud is larger and therefore the coupling scheme shown above is more stable.

The hyperfine structure has been first calculated by Bakalov and Korobov (BK) [97] who showed that the HF splitting is in the order of $\nu_{\text{HF}} = 10\text{--}15$ GHz, while the SHF splitting is about two orders of magnitude smaller: $\nu_{\text{SHF}} = 0.1\text{--}0.3$ GHz. Note that in laser transitions, it is the difference between the two hyperfine splittings which comes into play. In the case of $(n, \ell) \rightarrow (n+1, \ell-1)$ transitions (unfavored transitions), the splitting is of the order of 1.5 Gz and can be partially resolved in the laser resonance profiles, while in the case of $(n, \ell) \rightarrow (n-1, \ell-1)$ transitions (favored transitions) it is less than 0.5 GHz and hence cannot be easily resolved. In order to determine the hyperfine splittings, it is necessary to induce microwave transitions as indicated by wavy lines in figure 8, as discussed in detail in section 5.

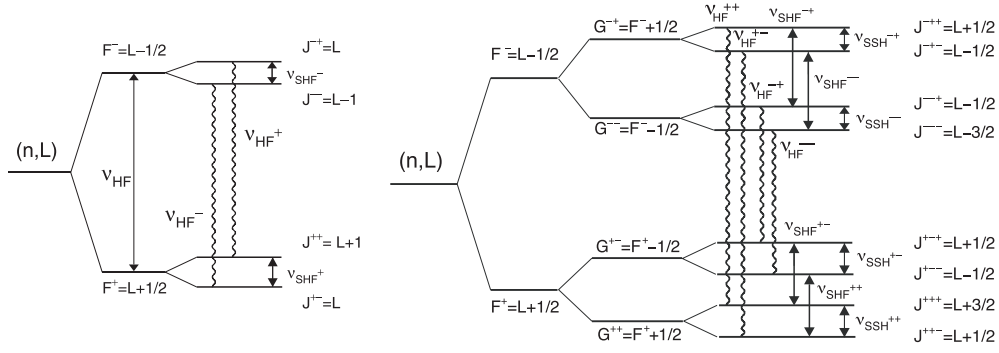


Figure 8. Hyperfine splitting of a state (n, L) of $\bar{p}^4\text{He}^+$ (left) and of $\bar{p}^3\text{He}^+$ (right). The wavy lines denote allowed M1 transitions that can be induced by microwave radiation.

According to BK, the interaction part of the three-body relativistic Hamiltonian has the form of a sum of pairwise Breit interaction operators, calculated up to terms of $O(\alpha^4)$ in the one-photon-exchange approximation

$$U = U_{12} + U_{13} + U_{23}. \quad (28)$$

The interaction of a pair of spin-1/2 particles can be written (in atomic units) as

$$U_{ij} = \alpha^2 \left\{ -\frac{8\pi}{3} \left(\frac{\mu_i}{m_i} \right) \left(\frac{\mu_j}{m_j} \right) (\mathbf{s}_i \cdot \mathbf{s}_j) \delta(\mathbf{r}) - \frac{1}{r^5} \left(\frac{\mu_i}{m_i} \right) \left(\frac{\mu_j}{m_j} \right) [3(\mathbf{r} \cdot \mathbf{s}_i)(\mathbf{r} \cdot \mathbf{s}_j) - r^2(\mathbf{s}_i \cdot \mathbf{s}_j)] \right. \\ \left. - (z_i - 2\mu_i) \frac{z_j}{2m_i^2 r^3} (\mathbf{r} \times \mathbf{p}_i) \cdot \mathbf{s}_i + \frac{z_i \mu_j}{m_i m_j r^3} (\mathbf{r} \times \mathbf{p}_i) \cdot \mathbf{s}_j \right. \\ \left. + (z_j - 2\mu_j) \frac{z_i}{2m_j^2 r^3} (\mathbf{r} \times \mathbf{p}_j) \cdot \mathbf{s}_j - \frac{z_j \mu_i}{m_i m_j r^3} (\mathbf{r} \times \mathbf{p}_j) \cdot \mathbf{s}_i \right\}, \quad (29)$$

and the interaction of a spin-1/2 particle with a spinless one is

$$U_{ij} = -\alpha^2 \left\{ (z_i - 2\mu_i) \frac{z_j}{2m_i^2 r^3} (\mathbf{r} \times \mathbf{p}_i) \cdot \mathbf{s}_i + \frac{z_j \mu_i}{m_i m_j r^3} (\mathbf{r} \times \mathbf{p}_j) \cdot \mathbf{s}_i \right\}. \quad (30)$$

Here, \mathbf{s}_i , \mathbf{p}_i , m_i , z_i and μ_i , respectively, are the spin vector, the momentum vector, mass, charge and magnetic moment of particle i , and $\mathbf{r} = \mathbf{r}_j - \mathbf{r}_i$ is the relative position vector.

After numerically integrating the interaction part of the Hamiltonian, equations (29) and (30), an effective Hamiltonian \mathcal{H}_{HF} is obtained, which in the case of antiprotonic ^4He takes the form

$$\mathcal{H}_{\text{HF}} = E_1(\mathbf{L}_{\bar{p}} \cdot \mathbf{S}_e) + E_2(\mathbf{L}_{\bar{p}} \cdot \mathbf{S}_{\bar{p}}) + E_3(\mathbf{S}_e \cdot \mathbf{S}_{\bar{p}}) \\ + E_4\{2L(L+1)(\mathbf{S}_e \cdot \mathbf{S}_{\bar{p}}) - 6[(\mathbf{L}_{\bar{p}} \cdot \mathbf{S}_e)(\mathbf{L}_{\bar{p}} \cdot \mathbf{S}_{\bar{p}})]\}. \quad (31)$$

The first term, the S_e - $L_{\bar{p}}$ interaction, gives the dominant HF contribution. Figure 9 shows the level ordering caused by the other terms, namely, the \bar{p} spin-orbit interaction (E_2), the scalar spin-spin (E_3) and the tensor spin-spin interaction (E_4). As can be seen, all splittings are of similar size, but one of the contributions has an opposite level order leading to an effective cancellation of two terms. The final level order is thus given by the spin-orbit interaction. Such cancellation effects make the theoretical predictions sensitive to small uncertainties and therefore call for a precise experimental determination of the hyperfine structure of antiprotonic helium.

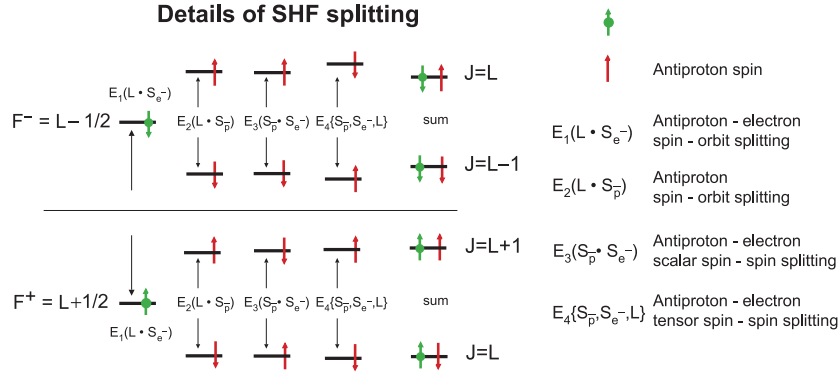


Figure 9. Individual contributions to the SHF splitting.

3. Laser spectroscopy of antiprotonic helium $\bar{p}\text{He}^+$ atoms

During the years 2000–2006, three generations of laser spectroscopy experiments on $\bar{p}\text{He}^+$ were carried out at the AD. These increased the fractional precision on the atom's transition frequency ν_{exp} , from $(1.3\text{--}1.6) \times 10^{-7}$ to $\sim 9 \times 10^{-9}$ (table 4: see subsequent sections for details on the experimental errors). Although the techniques, instrumentation, and sources of systematic errors in the three experiments were quite different, consistent results on ν_{exp} were obtained. This section outlines some of the basic principles of the laser spectroscopy (described in section 3.2) and the instrumentation used in these experiments. This includes the AD itself (section 3.1), the cryogenic target where the $\bar{p}\text{He}^+$ were synthesized, the laser system and detectors.

Most of these experimental efforts improved the following two factors which, as in other types of laser spectroscopy measurements involving normal atoms, limited the precision on ν_{exp} : (i) *spectral purity and accuracy of the spectroscopic laser*; the optical frequencies of the laser beams used here were calibrated and controlled to a precision of 1 part in $10^7\text{--}10^8$. Its linewidth (i.e. the energy spread of the photons) was narrowed to less than 1 part in $10^6\text{--}10^7$,

Table 4. Various sources of experimental error in three measurements of the $\bar{p}\text{He}^+$ transition frequencies, carried out using the 5.3 MeV antiproton beam of AD [94], the 100 keV beam of the RFQD [95] and using a cw pulse-amplified dye laser stabilized to an optical frequency comb generator [51].

Error source	AD only experiment [94] (MHz)	RFQD experiment [95] (MHz)	Frequency comb experiment [51] (MHz)
Density extrapolation	20–50	0.1–1	0.1–2
Statistical	20–40	20–200	3–13
Laser frequency calibration	70–140	20–50	<1
Frequency chirp in dye laser	—	—	2–4
Frequency chirp in SHG/THG	<10	<10	1–2
Magnetic effects	<1	<1	<1
Ac Stark effects	<1	<1	<1
HFS calculation uncertainties	<1	<1	<1
Total error	80–150	30–200	4–15

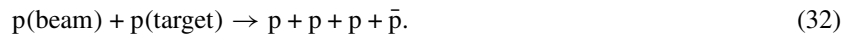
(ii) ‘quality’ of the $\bar{p}\text{He}^+$ target; if these atoms were to be studied by high-precision laser spectroscopy, they had to be cooled to Kelvin-scale temperatures and preferably isolated in low-density targets where their atomic energy levels would not be perturbed by collisions with the surrounding atoms. This was not easy to do, because antiprotons can only be produced by GeV-scale collisions (see section 3.1), and so a 13–14 orders of magnitude difference in the energy scale had to be first bridged to carry out these experiments.

The first generation of experiments (described in section 3.3) directly utilized the 5.3 MeV antiproton beam of AD to synthesize $\bar{p}\text{He}^+$ in a target of relatively high density (atomic density $\rho \geq 10^{21} \text{ cm}^{-3}$, corresponding to collision rates of several GHz). The spectroscopy was carried out with a type of pulsed dye laser which is widely used in other accelerator-based experiments. The second generation (sections 3.5 and 3.6) used a radiofrequency quadrupole post-decelerator (RFQD) to first slow down the AD antiprotons from 5.3 MeV to 60 keV, before stopping them in an ultra-low density ($\rho \leq 10^{17} \text{ cm}^{-3}$) target. This technique reduced the above GHz-rates of collisions that the resulting $\bar{p}\text{He}^+$ suffered with other helium atoms in the target to a few MHz. The third generation (sections 3.7 and 3.8) utilized new laser technologies, including an optical frequency comb, to further improve the spectral resolution and precision. To our knowledge, this constituted one of the first times when a comb was used in an accelerator experiment.

3.1. The Antiproton Decelerator at CERN

In order to produce antiprotonic atoms in the laboratory, we first need a supply of antiprotons with kinetic energies comparable to or less than the eV-scale binding energies of the atoms [53, 98–101]. These conditions were first realized at CERN (figure 10) by the construction of the Low Energy Antiproton Ring (LEAR) facility in 1982 [64, 102–104]. LEAR was later succeeded by the Antiproton Decelerator (AD) in 1999 [105–107], which is presently the world’s only source of low energy antiprotons (figure 11).

Antiprotons to be introduced into the AD for subsequent deceleration to energies suitable for these $\bar{p}\text{He}^+$ experiments were produced by directing a 26 GeV proton beam from the CERN Proton Synchrotron (PS) to a stationary metal target [102]. The following reaction (or a similar one involving target neutrons) can then occur under the constraints imposed by the conservation of energy, momentum and nucleon number:



We can easily see that the minimum kinetic energy (the ‘threshold’) of the incoming proton in the laboratory frame needed for the above reaction to take place is roughly equal to six proton masses, i.e. $E \sim 6 \text{ GeV}$. The antiproton and three protons must then each emerge from the reaction with laboratory kinetic energies of $\sim 1 \text{ GeV}$. In practice, the AD employs higher proton energies ($E = 26 \text{ GeV}$) to increase the production yield of antiprotons over its threshold value. The antiprotons thus emerge with energies $E \sim 3 \text{ GeV}$, and this must be subsequently reduced by eight orders of magnitude before they can be used to create antiprotonic atoms for laser spectroscopy experiments. A simple deceleration of a cloud containing N antiprotons, however, would lead to an adiabatic increase in its phase-space density D defined as

$$D = \frac{N}{\sqrt{E_h E_v} L \Delta p / p}, \quad (33)$$

wherein E_h and E_v denote the horizontal and vertical emittances of the cloud, L its longitudinal length and $\Delta p / p$ the spread of the antiproton’s momentum distribution. In fact, calculations show that D would become so small (more than 3 orders of magnitude) that hardly any antiprotons could be made to come to rest in a cm-sized experimental gas target [102].

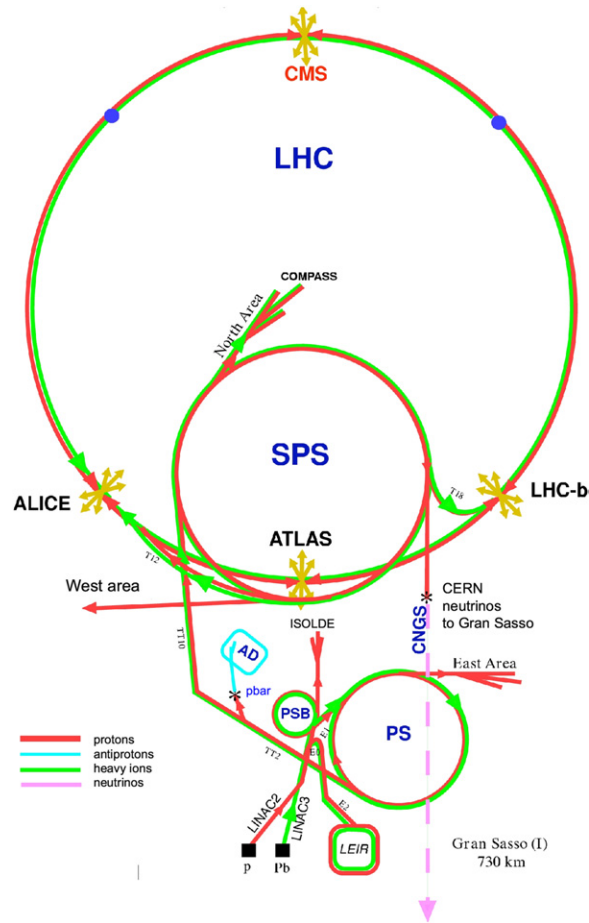


Figure 10. Schematic layout of CERN’s accelerator complex. The LINAC2 linear accelerator and the PSB booster feed protons into the PS proton synchrotron, which accelerates them to 25 GeV/ c and passes them to the experiments in the East Area or to the SPS super proton synchrotron for further acceleration and once every 100 s into an iridium target to produce antiprotons. The antiprotons are collected at 3.5 GeV/ c by the AD where they are decelerated in three steps to 100 MeV/ c . The PS also accelerates heavy ions for the SPS North Area experiments and until 2000 it accelerated electrons and positrons for the LEP Large Electron Positron collider. The latter was removed and in 2007 replaced by the LHC Large Hadron Collider.

The AD solves these problems by alternately decelerating and cooling the beam (i.e. reducing its phase-space and increasing the D -value) [105–107] over a 100 s cycle (figure 12 and table 5). Antiprotons of momentum $p \sim 3.6$ GeV/ c emerging from a 50 mm long iridium target placed in the path of the PS beam are first focused into a parallel beam by a horn-type lens. A bunch containing about 5×10^7 antiprotons can be collected in the 80 m diameter, oval-shaped AD ring (figure 11), per PS pulse of about 1.5×10^{13} protons. They initially have a large emittance $E_h \sim E_v \sim 200\pi$ mm mrad and momentum spread $\Delta p/p \sim 6\%$. RF bunch rotation fields are then applied to these antiproton pulses, to stretch their pulse-lengths from the initial value of $L = 30$ m (corresponding to $\Delta t = 25$ ns) to 180 m (150 ns). Since the longitudinal emittance $L\Delta p/p$ must be ideally conserved (see equation (33)), this reduces $\Delta p/p$ to $\sim 1.5\%$. Next, in the stochastic cooling and deceleration phase, a series of pickup electrodes detect the size and revolution frequency of the antiproton beam orbiting the AD.

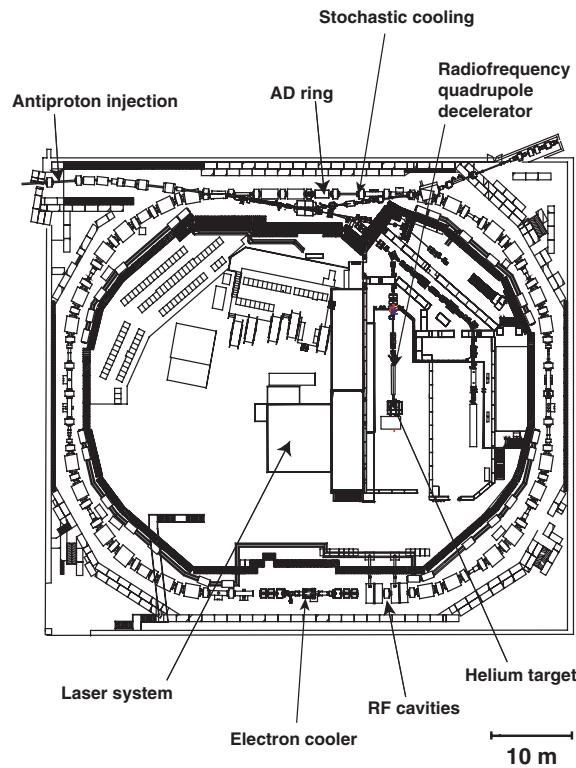


Figure 11. Schematic diagram of the Antiproton Decelerator, showing the locations of various components of the synchrotron, and the laser spectroscopy experiment of $\bar{p}\text{He}$ atoms.

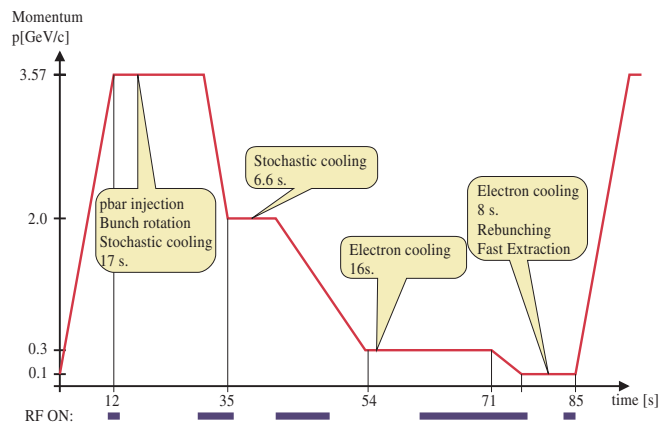


Figure 12. Typical machine cycle of the Antiproton Decelerator [106] showing the momentum of antiprotons as a function of the time elapsed. The times at which stochastic and electron cooling are applied are shown.

The high sensitivity and GHz-scale bandwidths allow these detectors to measure fluctuations Δp_i and Δx_i in the longitudinal momentum and transverse deviations of small subgroups N_i of antiprotons, relative to the mean values of all N orbiting antiprotons [108, 109]. These signals Δp_i and Δx_i are then used to correct the orbits of the corresponding subgroups, by applying

Table 5. Emittances and momentum spread of antiprotons in the AD, before and after the various bunch rotation and cooling steps. From [106].

p (GeV/c)	Initial emittances			Final emittances			t (s)
	ε_h (π mm mrad)	ε_v	$\Delta p/p$ (%)	ε_h (π mm mrad)	ε_v	$\Delta p/p$ (%)	
<i>Bunch rotation</i>							
3.5	180	200	6	200	200	1.5	
<i>Stochastic cooling</i>							
3.5	180	200	1.5	3	4	0.07	17
2.0	9	9	0.18	3	3	0.015	7
<i>Electron cooling</i>							
0.3	33	33	0.2	2.7	2.7	0.01	16
0.1	6	6	0.3	0.3	0.3	0.01	8

pulses to steering electrodes located in the opposite side of the AD. Repeated corrections of this kind in all subgroups cause the beam to ‘stochastically’ cool and converge to a single ideal orbit, such that the emittances are reduced to $3\text{--}4\pi$ mm mrad and $\Delta p/p$ to 0.07%. The antiprotons are then decelerated to $p = 2$ GeV/c by RF fields and cooled in the same way to 3π mm mrad and $\Delta p/p \sim 0.015\%$. Finally, after the deceleration to $p = 300$ MeV/c, they are subjected to electron cooling. The antiprotons are here allowed to merge with an electron beam of ampere-scale currents and a few centimetres diameter, in a collinear configuration over a 1.5 m long section of the ring [103, 110, 111]. The electron velocity (corresponding to an energy $E = 25.5$ keV) is matched to the antiproton’s, such that in the center-of-mass frame the antiprotons find themselves bathed in a stationary electron cloud of low temperature. Coulomb collisions transfer the ‘heat’ of the antiprotons to the electrons. By continuously replenishing cold electrons from a cathode gun into the antiproton beam and removing the hot electrons at the end of the interaction region, the antiprotons are cooled within a few seconds to $E_h \sim E_v \sim 2.7\pi$ mm mrad and $\Delta p/p \sim 0.01\%$. The antiprotons are finally decelerated to $p = 100$ MeV/c and electron-cooled to 0.3π mm mrad and $\Delta p/p \sim 0.01\%$.

At the end of the above cycle, the AD ejected a 100 ns long beam containing $(2\text{--}3) \times 10^7$ antiprotons of energy 5.3 MeV into one of the four experimental zones located inside the ring (figure 11). Of these, the ASACUSA collaboration has carried out several experiments on the antiprotonic helium described here and atomic [112–114] and nuclear collisions using antiprotons. Two other groups, ATRAP [49, 115–117] and ATHENA [48, 118–120], have synthesized cold antihydrogen atoms. ATRAP and a new experiment ALPHA are currently attempting to confine the antihydrogen atoms in magnetic multipole traps [121–123]. A fourth experimental group, ACE, measured the biological response of cells against antiproton irradiation [124].

3.2. Laser-induced annihilation spectroscopy

As described in section 2, experiments [68, 125] have revealed that some 3% of antiprotons that come to rest in helium targets form $\bar{p}\text{He}^+$ with microsecond-scale lifetimes against antiproton annihilation in the helium nucleus. The atomic $E1$ transitions of the antiprotons in these metastable states lie in the optical frequency region (the theoretical transition wavelengths [77, 81, 83, 126] of some of these are shown in figure 13 in nanometres). All these transitions can therefore be excited by resonant laser beams, but here the difficulty is in experimentally detecting such excitations. Although a variety of laser spectroscopic

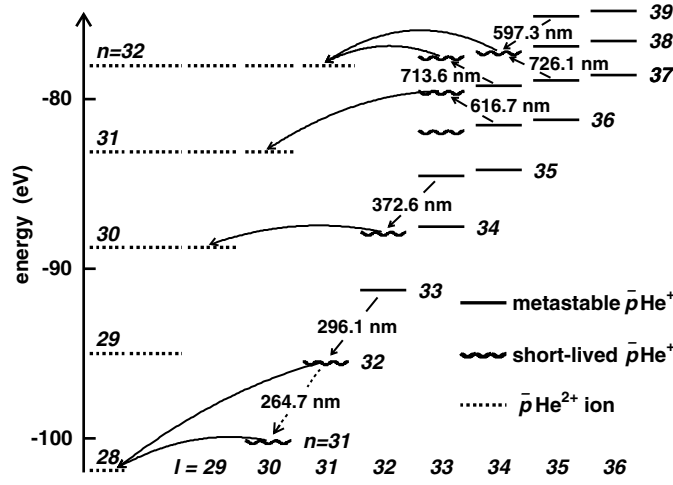


Figure 13. The level structure of $\bar{p}^4\text{He}^+$, with $E1$ transition wavelengths shown in nanometres [127]. The solid lines indicate radiation-dominated metastable states, the wavy lines Auger-dominated short-lived states. The broken lines indicate $\bar{p}\text{He}^{2+}$ ionic states formed after Auger emission, the curved arrows Auger transitions with minimum $|\Delta\ell|$. On the left-hand scale the theoretical absolute energy of each state is plotted relative to the three-body breakup threshold.

techniques (e.g. laser-induced fluorescence, absorption, or ionization) can be employed for normal atoms, they cannot be used in the $\bar{p}\text{He}^+$ case. Any such signal from a small number of $\bar{p}\text{He}^+$ atoms with short (microsecond-scale) lifetimes against annihilation would be practically invisible against the strong background (e.g. scintillation light and ionization) induced by the antiprotons slowing down or annihilating in an experimental target.

We instead use the clear, unambiguous signal produced by the annihilation of the antiprotons when they finally arrive in the helium nuclei [69, 70]. At $\bar{p}\text{He}^+$ formation, the antiproton initially occupies states with principle and angular momentum quantum numbers $n \sim 38$ and $\ell \sim n - 1$ [71–75, 128]. It then proceeds to deexcite spontaneously by traversing a constant- $v \equiv n - \ell - 1$ cascade of metastable states (indicated by arrows in figure 13). Finally the atom reaches a short-lived state (wavy lines) which leads to rapid Auger electron emission [76, 80, 129, 130] and annihilation of the antiproton on the nucleus. By detecting the charged pions emerging from these annihilations, a delayed annihilation time spectrum (i.e. the distribution of the number of annihilations as a function of the time elapsed since $\bar{p}\text{He}^+$ formation) can be obtained [68, 125, 131].

In the rest of this section, we use the $\bar{p}^4\text{He}^+$ transition $(n, \ell) = (39, 35) \rightarrow (38, 34)$ as an illustrative example to explain the experimental technique and the way in which the results can be interpreted. The delayed annihilation time spectrum for the spontaneous processes referred to above can be seen as a low-level background in figure 14(a) [132]. Atoms could be irradiated at any given instant during this time period with a pulsed laser, the wavelength of which was tuned to stimulate antiproton transitions from metastable states to the Auger-dominated short-lived states described above [70]. This would cause these otherwise long-lived antiprotons to annihilate immediately. The resonance condition between the laser beam and the atom was then revealed as a sharp peak in the annihilation rate. The example in figure 14(a) shows the transition $(39, 35) \rightarrow (38, 34)$ at a wavelength $\lambda = 597.256$ nm, with the laser pulse applied at $t = 1.3 \mu\text{s}$. The peak decays with the lifetime ($\tau \sim 15$ ns) of the Auger-dominated state $(38, 34)$, convoluted with the timing structure of the laser pulse. By plotting the peak intensity as a function of the laser wavelength, a resonance profile was obtained (figure 15 (top left)).

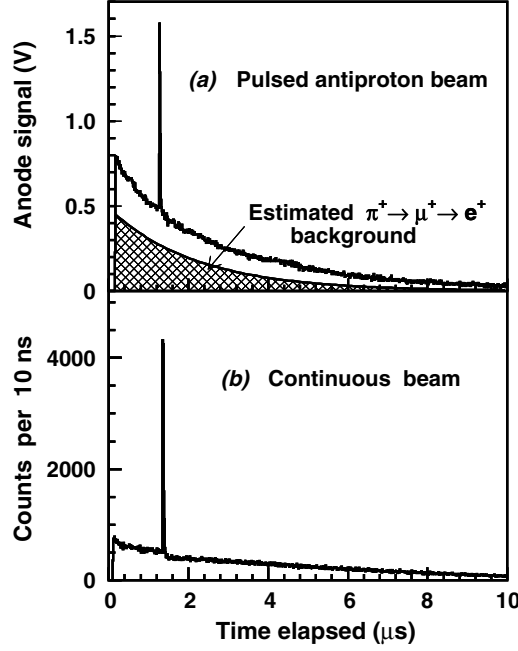


Figure 14. Delayed annihilation time spectrum measured using a pulsed antiproton beam [132], with the resonance transition $(n, \ell) = (39, 35) \rightarrow (38, 34)$ at wavelength $\lambda = 597.3$ nm induced at $t = 1.6 \mu\text{s}$ (a). The hatched area represents the estimated contribution of $\pi^+ \rightarrow \mu^+ \rightarrow e^+$ decay. The background-free spectrum measured using a continuous antiproton beam at the same target conditions, the spike induced at the same timing (b).

Now among the many $E1$ transitions involving $\bar{p}^4\text{He}^+$ states of $n \leq 40$, the following two types (some of which are shown in figure 15) are most amiable to laser spectroscopy.

- $(n, \ell) \rightarrow (n - 1, \ell - 1)$ (i.e. $\Delta v = 0$), which lie in the wavelength region $\lambda = 264.7\text{--}776.1$ nm. We call these ‘favored’ transitions, since they have the highest rates corresponding to transition dipole moments $\mu_{if} = 0.2\text{--}0.8$ D (1 Debye = 10^{-18} esu) [76, 80, 133].
- $(n, \ell) \rightarrow (n + 1, \ell - 1)$, characterized by $\Delta v = 2$, $\lambda = 395.6\text{--}1154.8$ nm and $\mu_{if} = 0.02\text{--}0.1$ D. The partial rates of these ‘unfavored’ transitions are ~ 100 times smaller than in the favored case.

Note that the dipole moment μ_{if} is related to the spontaneous radiation rate $1/\tau$ by the equation

$$\frac{1}{\tau} = \frac{\omega^3 \mu_{if}^2}{3\pi \epsilon \hbar c^3}, \quad (34)$$

wherein $\omega = 2\pi c/\lambda$ denotes the optical angular frequency of the laser and ϵ , \hbar and c the dielectric constant of vacuum, the Planck constant divided by 2π and the speed of light.

The expected time evolution of the antiproton populations in the resonant parent $(n, \ell) = (39, 35)$ and daughter $(38, 34)$ states under laser irradiation will reveal the laser intensity needed to drive the transition within the microsecond-scale lifetime of $\bar{p}\text{He}^+$. To calculate this, we integrate the optical Bloch equation for a single-photon transition induced

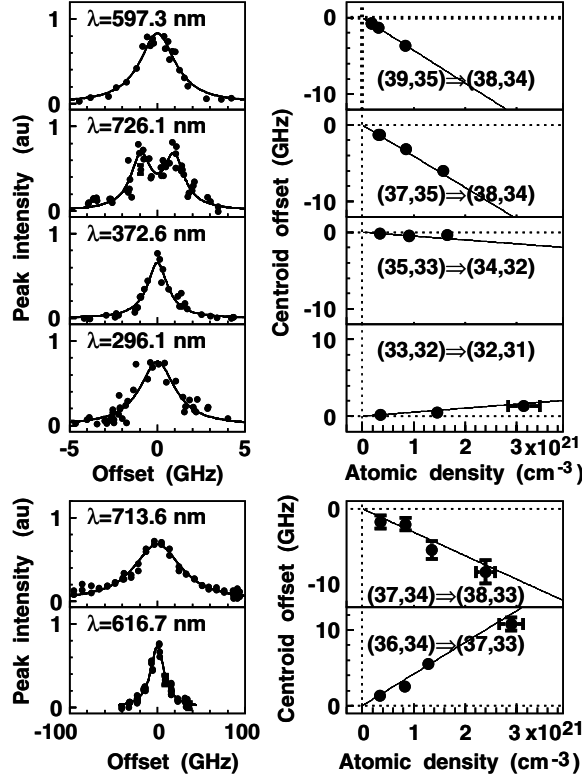


Figure 15. Six laser resonance profiles [94] of $\bar{p}^4\text{He}^+$ (left) measured using the 5.3 MeV antiproton beam of AD. Transition frequencies ν_{exp} measured at various target densities ρ (right). GHz-scale shifts in ν_{exp} which were linear with ρ were observed, caused by collisions between $\bar{p}\text{He}^+$ and helium atoms in the target.

by a linearly polarized laser beam [132],

$$\frac{d}{dt} \begin{pmatrix} P_1 \\ P_2 \\ P_x \\ P_y \end{pmatrix} = \begin{pmatrix} -\tau_{1m}^{-1} & 0 & 0 & \Omega_m/2 \\ 0 & -\tau_{2m}^{-1} & 0 & -\Omega_m/2 \\ 0 & 0 & -(\tau_1^{-1} + \tau_2^{-1})/2 - \Gamma_m & \Delta\omega \\ -\Omega_m & \Omega_m & -\Delta\omega & -(\tau_1^{-1} + \tau_2^{-1})/2 - \Gamma_m \end{pmatrix} \begin{pmatrix} P_{1m} \\ P_{2m} \\ P_{xm} \\ P_{ym} \end{pmatrix}, \quad (35)$$

where the populations in the parent and daughter states with a magnetic quantum number m are denoted by P_{1m} and P_{2m} and the real and imaginary parts of the off-diagonal terms in the density matrix by P_{xm} and P_{ym} . The state lifetimes are denoted by τ_{1m} ($\sim 1 \mu\text{s}$ [76, 127, 133, 134]) and τ_{2m} ($\sim 9 \text{ ns}$) and the detuning of the laser from the transition frequency by $\Delta\omega$. The rate of dephasing collisions caused by the GHz-scale collisions between $\bar{p}\text{He}^+$ and normal helium atoms in an experimental target is denoted by Γ_m [135]. These collisions lead to a broadening of the measured resonance profiles with a roughly Lorentzian shape.

The frequency $\Omega_m(t)/2\pi$ (in GHz) of Rabi oscillations of antiproton populations between states (n, ℓ, m) and $(n \pm 1, \ell - 1, m)$, induced by a linearly polarized laser pulse with a time

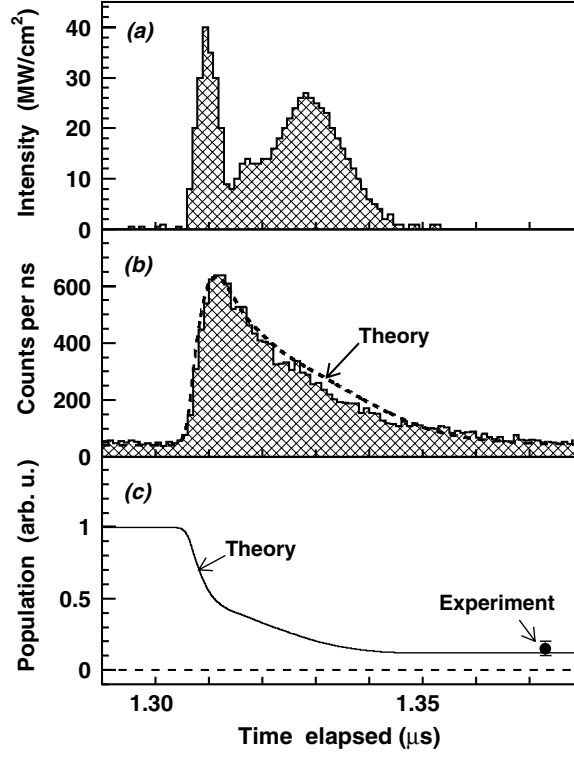


Figure 16. Typical temporal profile [132] of the laser pulse with an energy density $\Theta = 1 \text{ mJ cm}^{-2}$ (a). Experimental (solid line) and theoretical (dotted line) profiles of the 597.3 nm resonance spike (b). The simulated population evolution of the resonance parent state $(n, \ell)=(39, 35)$ during the laser pulse (—) and the measured depopulation efficiency (●) (c).

profile $\Theta(t)$ (in kilowatts per cm^2 , see figure 16(a)), can be calculated as,

$$\frac{\Omega_m(t)}{2\pi} = 0.44\mu \sqrt{\Theta(t) \frac{(\ell - m - 1)(\ell + m - 1)}{\ell(2\ell - 1)}}. \quad (36)$$

The dipole moment of this transition $\mu \sim 0.6\text{D}$ was obtained from the measured radiative lifetime [127] and equation (34).

In figure 16(c), the calculated time evolution of the population in state (39, 35) during laser irradiation on resonance, obtained by numerically integrating equation (35) and averaging over m , is shown. The laser pulse (figure 16(a)) used in this example has a 10 ns long timing structure. About $\varepsilon \sim 90\%$ of the antiprotons in the metastable parent state underwent laser-induced deexcitation to the daughter state [132], followed by Auger deexcitation and annihilation. In figure 17 (solid lines), the theoretical value of this efficiency ε of depopulating the antiproton population of state (39, 35) at laser energy densities $\Theta = 0$ and 2 mJ cm^{-2} is shown. These simulations show that resonance signals are maximized at $\Theta \sim 1 \text{ mJ cm}^{-2}$. In fact, these values are in good agreement with the results of experiments (plotted using filled circles) described below.

3.3. First experiments at AD

Laser spectroscopy experiments of $\bar{\text{pHe}}^+$ were carried out during the first few weeks following the commissioning of the AD in 2000 [94]. $\bar{\text{pHe}}^+$ were produced by extracting antiproton

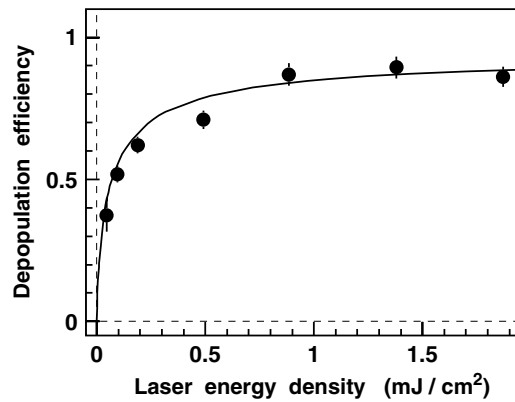


Figure 17. Experimental (●) and theoretical (—) depletion efficiencies of the laser pulse tuned to the transition $(39, 35) \rightarrow (38, 34)$ at wavelength $\lambda = 597.3$ nm at various energy densities of the laser [132].

pulses of energy $E = 5.3$ MeV from AD and bringing them to rest in a cryogenic helium gas target (figure 18). This was done by adjusting the thickness of a series of degrader foils located upstream of the target entrance window. This caused multiple scattering and range straggling in the antiproton beam. High densities ($\rho > 10^{20}$ cm⁻³) of the helium target were needed to ensure that most of the decelerated antiprotons of large emittance and momentum spread stopped in the cm-sized target. The spatial profile of the antiproton pulse was measured by a parallel plate secondary emission chamber [136], also placed upstream of the target. A series of magnetic elements in the transport beamline of AD were adjusted using this readout so as to focus the antiprotons within a 3 mm diameter spot at the target entrance. The target itself contained ⁴He gas at a temperature $T \sim 6$ K and pressure $P = 0.2$ – 2.5 bar.

Although most antiprotons annihilated promptly after stopping in the helium (i.e. within ~ 10 ns), about 3% of them formed $\sim 5 \times 10^5$ metastable atoms, in which their annihilation was delayed by an average lifetime of $\tau = 3$ – 4 μ s, because of their passage through the atomic cascade of states shown in figure 13. Charged particles (mostly π^+ and π^- , as well as electrons and positrons originating from the γ -rays undergoing pair production in the target chamber walls) emerging from all these annihilations produced Cherenkov light in two 2 cm thick plates of UV-transparent acrylic plates [94, 137]. These constituted the annihilation detectors which allowed us to detect the delayed annihilation time spectra referred to above. The plates were placed on either side of the target and covered a solid angle of 2π steradian seen from the target. The envelope of the resulting light pulse consisted first of a bright (peak power 5–20 mW), 200 ns long flash from the promptly annihilating antiprotons corresponding to the 97% that annihilate within a few picoseconds without forming metastable $\bar{p}\text{He}^+$; this was followed by a much longer but less intense tail from delayed annihilations of the metastable atoms. The pulse was detected by a photomultiplier in which the electron multiplication could be gated off during the prompt annihilation (thus preventing the detector from being blinded by the initial flash) and then turned back on (with a rise time of < 100 ns) to detect the delayed annihilation. The output pulse therefore included only delayed annihilations and had an amplitude of 0.2–0.3 V and a length of 15 μ s or more. The analog waveform of this pulse was recorded by a digital oscilloscope [137].

Considerable efforts were made to develop photomultipliers whose analog output signal would constitute a faithful representation of the annihilation spectrum of $\bar{p}\text{He}^+$. In fact, some initial experiments were hampered by spurious afterpulse signals (i.e. those signals produced

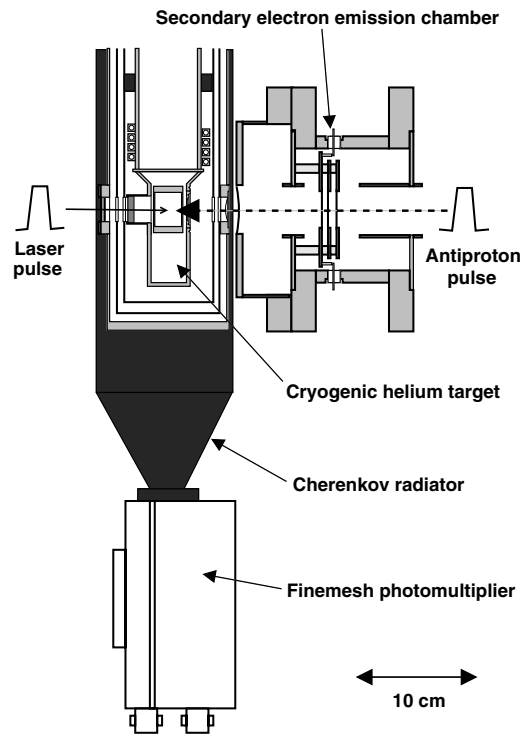


Figure 18. Layout of the laser spectroscopy experiment of $\bar{p}\text{He}^+$ carried out using the $E = 5.3$ MeV antiproton beam. The pulsed beam of antiprotons (right) come to rest in a cryogenic helium target, thereby producing $\bar{p}\text{He}^+$ [137]. The atoms are irradiated by a laser pulse entering the target (left) collinear with the antiproton beam. The pions emerging from the laser-induced annihilation of $\bar{p}\text{He}^+$ are detected by Cherenkov counters surrounding the target. The spatial profile of the antiproton beam is measured by a secondary electron emission chamber.

by ions accelerated inside the photomultiplier and striking the photocathode [137]) and by non-linearities in the recorded spectra. It was found that while all types of photomultipliers unavoidably produce these afterpulses, ‘fine mesh’ photomultipliers (i.e. those wherein the photoelectrons are amplified in a series of parallel mesh electrodes) do not produce sharp pulses [137]. The fine-mesh photomultipliers also showed a higher linearity compared with the line-focus ones. All these characteristics allowed it to be used in these high-precision measurements.

This ‘analog’ method of using a pulsed antiproton beam has several advantages [132], compared with other accelerator-based laser spectroscopy experiments which typically rely on the counting of individual particles in a continuous beam [139–142]: (i) here a single laser pulse simultaneously induced transitions in 10^3 – 10^4 $\bar{p}\text{He}^+$ atoms. This meant that large numbers of $\bar{p}\text{He}^+$ could be produced and studied at a high rate. (ii) The repetition rate of the pulsed laser needed to excite the $\bar{p}\text{He}^+$ was very low ($f_r \sim 0.01$ Hz). This relaxed requirement made it easier to design laser systems of high precision and spectral purity, compared with other experiments using a continuous beam that require f_r -values of 100–2000 Hz.

The largest disadvantage of the analog method lies in the fact that it cannot differentiate between the Cherenkov light produced by signal pions emerging from $\bar{p}\text{He}^+$ annihilations and the background caused by other relativistic charged particles striking the detector. This limited

the sensitivity of this method in $\bar{p}\text{He}^+$ laser transitions with weak intensities [137]. The largest background was caused by those low energy π^+ -mesons that emerged from the annihilations and stopped in the target walls or in the detector. These decayed into positive muons with a mean lifetime of $\tau = 26$ ns and further decayed into positrons with a $2.2 \mu\text{s}$ lifetime. Some of these positrons, whose mean energy was $E = 40$ MeV, then struck the detector and produced delayed photoelectrons. The delayed annihilation time spectrum shown in figure 14(a) was measured by stopping a pulse of 2×10^8 antiprotons in the helium target and stimulating the transition $(n, \ell) = (39, 35) \rightarrow (38, 34)$ at a wavelength of $\lambda = 597.26$ nm at $t = 1.6 \mu\text{s}$. The hatched area represents the estimated contribution from the $\pi^+ \rightarrow \mu^+ \rightarrow e^+$ background obtained from Monte-Carlo simulations, which constitutes 50–60% of the detected Cherenkov light.

It is informative to compare the analog signal of figure 14(a), with the spectrum measured previously at LEAR by the more orthodox method of using a continuous antiproton beam (figure 14(b)). In the LEAR experiment, the antiprotons entered the target one by one at a rate of $f \sim 10^4$ Hz. $\bar{p}\text{He}^+$ were thus produced and detected in an event-by-event manner, which allowed the antiprotons occupying individual metastable states to be accurately counted under background-free conditions. Comparisons between the two spectra showed the above 50–60% estimation for the background to be quite accurate. In practice, this factor of ~ 2 deterioration in the signal-to-noise ratio in the AD data was more than offset by the much higher rate of data accumulation.

The laser pulses of energy density $0.1\text{--}1$ mJ cm $^{-2}$ needed to induce the $\bar{p}\text{He}^+$ resonances were generated by a grating-stabilized dye laser [143], which was pumped by the second or the third harmonic ($\lambda = 532/355$ nm) of a Q-switched Nd:YAG laser. Dye lasers of similar design have been widely used in other accelerator experiments [139–141] that require megawatt-scale peak powers. The main advantage of these lasers lies in the ease by which their fundamental wavelength can be tuned to any of the $\bar{p}\text{He}^+$ resonances at $\lambda = 470\text{--}726$ nm, by simply changing the organic dye solution which serves as the lasing medium. The UV laser pulses $\lambda = 265\text{--}372$ nm needed to induce the resonances involving states of lower n -values ($n \leq 35$) were produced by frequency doubling the above fundamental light in a beta-barium borate (BBO) crystal. The 4 ns pulse length of the dye laser was defined by the Nd:YAG pump laser. By adjusting its triggering timing, the metastable atoms could be irradiated at any time $t = 0.2\text{--}15 \mu\text{s}$ after their birth.

The instrumentational linewidth (typically around $\Delta\nu \sim 0.5\text{--}5$ GHz) of these pulsed dye lasers, relative to the optical frequency ($\nu \sim 0.5$ PHz), usually limits the achievable resolution and precision of atomic or molecular spectroscopy experiments using them to around $\Delta\nu/\nu \sim 10^{-6}$. Two difficulties generally arise when attempting to reach higher precisions of $\sim 10^{-7}$. The first of these is caused by quantum fluctuations [138, 144, 145] in the laser mode structure (i.e. the Fourier transform of the optical frequency components in the laser pulses). An ideal laser, wherein all the photons are concentrated into a single longitudinal mode of the cavity, would provide the highest precision in the measured $\bar{p}\text{He}^+$ profiles. In practice, however, these pulsed dye lasers [143] are usually ‘multi-mode’, i.e. the first few photons emitted spontaneously from the dye that initiate the lasing process can proceed to occupy several longitudinal cavity modes. The laser output used here contained 2–3 modes spaced by frequency intervals $\Delta\nu = 500$ MHz, corresponding to the free spectral range $\Delta\nu = c/2L$ of a $L = 300$ mm long laser cavity. The number of photons in a given mode thus fluctuate from shot to shot, following an exponential probability distribution. The fact that the $\bar{p}\text{He}^+$ are irradiated by a laser beam containing 2–3 optical frequency components, the relative intensities of which fluctuate from shot to shot, has a detrimental effect on the experimental precision. The second difficulty here is in the accurate wavelength calibration of such multimode laser pulses.

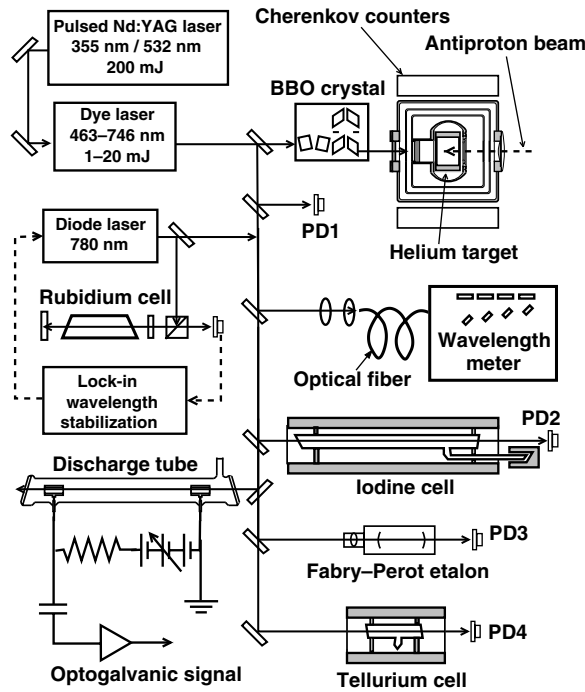


Figure 19. The setup of the laser system used in the $\bar{p}\text{He}^+$ spectroscopy experiment with the 5.3 MeV antiproton beam of AD [138]. Resonant laser pulses were generated by a dye laser pulsed by a Q-switched Nd : YAG laser. The laser wavelength was calibrated by carrying out optogalvanic spectroscopy of argon and neon or absorption spectroscopy of iodine. PDs; photodiodes.

Notwithstanding these difficulties, an absolute precision of $\sim 10^{-7}$ on the $\bar{p}\text{He}^+$ frequencies was achieved [94, 138] in the following way (figure 19). The wavelength and mode structure of each laser pulse was measured by a series of Fizeau interferometers (spectral resolution $\Delta\nu = 0.6$ GHz) constituting a wavelength meter. The fringe patterns of most of the laser pulses were broad ($\Delta\nu > 1$ GHz), but in 20–30% of the cases, the laser energy happened to be concentrated in a single longitudinal mode. Those broad-band laser pulses that deviated from a single mode were rejected; this effectively narrowed the laser linewidth to $\Delta\nu = 0.4\text{--}0.5$ GHz. During the 100 s intervals between the arrival of antiproton pulses, the laser wavelength was calibrated via ro-vibrational absorption spectroscopy of molecular iodine I_2 (relevant wavelengths $\lambda = 525\text{--}726$ nm) [146–148] or tellurium Te_2 (463–471 nm), or by optogalvanic spectroscopy [149] of neon or argon gas. The precision of the wavelength meter was continuously checked against a continuous-wave (cw) diode laser, the frequency of which was stabilized against hyperfine components of an ^{85}Rb transition by Doppler-free saturation spectroscopy [138].

Before the high-precision measurements of the $\bar{p}\text{He}^+$ transition frequencies could be carried out, the candidate resonances first had to be discovered. The energy level diagram of figure 20 indicates that more than a dozen laser transitions in $\bar{p}^3\text{He}^+$ and $\bar{p}^4\text{He}^+$ can in principle be detected, which would provide a most rigorous test of three-body QED calculations. The detection of any resonance critically depends on the existence of antiprotons populating the associated $\bar{p}\text{He}^+$ states. The state population is of course time-dependent and strongly varies according to the n - and ℓ -values. This is because, to first approximation, the antiproton is

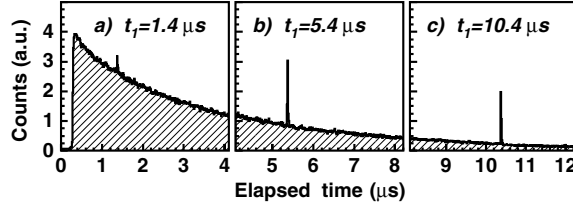


Figure 21. Three delayed annihilation time spectra of $\bar{p}^4\text{He}^+$ with laser-induced annihilation spikes of the transition $(n, \ell) = (33, 32) \rightarrow (32, 31)$ induced at $t_1 = 1.4 \mu\text{s}$ (a) $5.4 \mu\text{s}$ (b) and $10.4 \mu\text{s}$ (c). The spike intensities indicate the antiproton population in state $(33, 32)$ at each t [150].

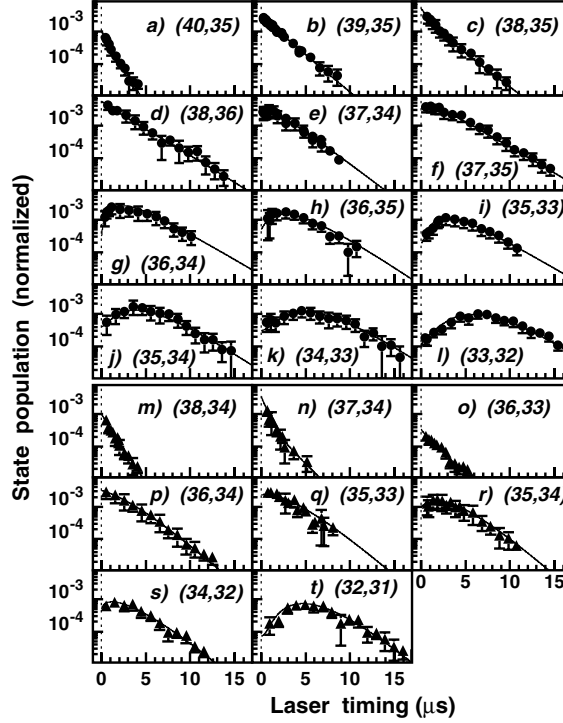


Figure 22. Time evolutions of the populations in twelve $\bar{p}^4\text{He}^+$ (filled circles with error bars in (a)–(l)) and eight $\bar{p}^3\text{He}^+$ (filled triangles in (m)–(t)) states. The best fit of a cascade model is shown in solid lines [150].

increasing the population of the latter. Those in $(38, 35)$ and $(38, 36)$ decreased with still longer ($\sim 2.2 \mu\text{s}$) lifetimes, because of spontaneous deexcitation from $(39, 36)$ and $(39, 37)$. The populations in $(37, 34)$ and $(37, 35)$ decreased with $3 \mu\text{s}$ -lifetimes, and had downward-bending profiles at early times caused by the large feeding from $(38, 35)$ and $(38, 36)$.

In contrast, very small primary populations were found in $\bar{p}^4\text{He}^+$ states in the $n \leq 36$ regions. The populations increased (figures 22(g)–(l)) as antiprotons deexcited from the higher, initially populated states, the time t_{max} at which the population reaches a maximum becoming progressively later for lower- n states. The longest-living antiprotons were found in the lowest metastable state $(33, 32)$ in the $v = 0$ cascade; since antiprotons captured in the $n \sim 38$ regions made 6–7 radiative transitions before reaching this state, a significant population ($\sim 0.01\%$) could be observed even at $t_1 = 16 \mu\text{s}$.

In $\bar{p}^3\text{He}^+$ atoms (figures 22(m)–(t)), the population in (38, 34) decreased with a $1.0\ \mu\text{s}$ lifetime, which indicates that the populations in the region $n \geq 39$ in the $v = 3$ cascade are very small. The largest populations ($P_{(n,\ell)}(t = 0) \sim 0.3\%$) were found in (36, 34), (36, 35), (37, 34), (37, 35) and (37, 36). In contrast to the $\bar{p}^4\text{He}^+$ case, significant primary populations were detected even in low- n regions, with the lowest metastable state in the $v = 1$ cascade having a value of $P_{(34,32)}(t = 0) = (0.06 \pm 0.02)\%$. The lowest state (32, 31) in the $v = 0$ cascade had, on the other hand, a negligible primary population.

The high-precision laser spectroscopy experiments described in the next section were carried out on six $\bar{p}^4\text{He}^+$ resonances which provided the highest intensity among those shown in figure 22. For each transition, the laser timing was adjusted to the value t_{max} which maximized the signal intensity.

3.4. Collisional frequency shifts in the $\bar{p}\text{He}^+$ transitions

The profiles of six $\bar{p}^4\text{He}^+$ transitions measured using the above methods are shown in figure 15 (left), each point corresponding to data collected from four antiproton pulses [94]. The resonances were typically 0.8–2.0 GHz wide, including contributions from the laser bandwidth (0.4–0.5 GHz, see above), the thermal Doppler broadening, collisional broadening and hyperfine splitting. The full-width-at-half-maximum value for the Doppler broadening of $\bar{p}\text{He}^+$ atoms thermalized to the temperature $T = 6\ \text{K}$ of the cryogenic helium target was calculated to be around $\Delta\nu_{\text{D}} = 0.3\text{--}0.8\ \text{GHz}$ using the equation

$$\Delta\nu_{\text{D}} \sim 2\sqrt{2\log(2)}\frac{v}{c}\sqrt{\frac{kT}{M}}, \quad (37)$$

wherein k denotes the Boltzmann constant and M the $\bar{p}\text{He}^+$ mass. Quantum chemical calculations [135] have estimated that the collisional broadening of these resonance lines to be between $\Gamma_m \sim 0.1$ and 2 GHz at the range of target densities studied here. The profile of the unfavored transition (37, 35) \rightarrow (38, 34) at $\lambda = 726.1\ \text{nm}$ [152], shows two peaks separated by an interval of $\Delta_{\text{HFS}} = 1.8 \pm 0.1\ \text{GHz}$; this is the hyperfine structure (see section 5 for a full description) which arises from the coupling between the orbital angular momentum of the antiproton and the electron spin. The above value of Δ_{HFS} is in good agreement with the theoretical one obtained from three-body QED calculations [96, 97, 153]. The splitting is much smaller ($\Delta_{\text{HFS}} \leq 0.5\ \text{GHz}$) for the other five favored ($\Delta n = -1$, $\Delta \ell = -1$) transitions, and therefore cannot be resolved within the spectral resolution shown in figure 15. In these initial experiments [94] of relatively low precision, the resonance centroid was obtained from these profiles by fitting two Voigt functions, superimposed on each other and separated by the theoretical value of the hyperfine splitting. Later experiments used a more sophisticated analysis technique as described below.

Collisions between $\bar{p}\text{He}^+$ and helium atoms in the target induced 100 MHz to GHz scale shifts in the measured transition frequencies ν [94, 93]. Quantum chemical calculations [135] indicated that these frequency shifts occur when collisions perturb the $\bar{p}\text{He}^+$ atomic orbitals and shift the energy levels involved in the laser transition. As the atomic density of the target was increased between $\rho = (0.1\text{--}3) \times 10^{21}\ \text{cm}^{-3}$, the frequencies of three resonances (39, 35) \rightarrow (38, 34) at a wavelength of $\lambda = 597.3\ \text{nm}$, (37, 35) \rightarrow (38, 34) at 726.1 nm and (37, 34) \rightarrow (38, 33) at 713.6 nm red-shifted with a gradient of $d\nu/d\rho = -3 \times 10^{-21}$ to $-4 \times 10^{-21}\ \text{GHz cm}^3$ (figure 15 (right)). The transitions at lower n -values, (35, 33) \rightarrow (34, 32) at $\lambda = 372.6\ \text{nm}$ and (33, 32) \rightarrow (32, 31) at 296.1 nm, had much smaller shifts $d\nu/d\rho = -(0.4 \pm 0.1) \times 10^{-21}$ and $(0.4 \pm 0.1) \times 10^{-21}\ \text{GHz cm}^3$, respectively. The experimental values of all five resonances lie within $\pm 20\%$ of the results of theoretical calculations [135].

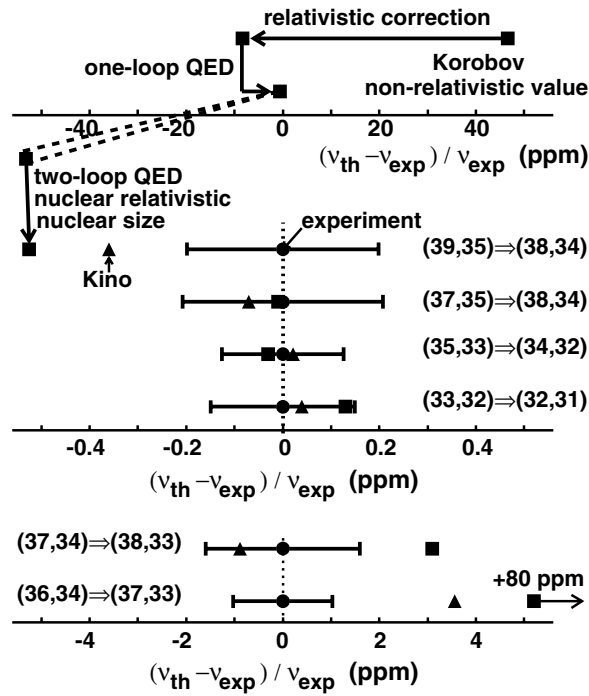


Figure 23. Comparisons between experimental (filled circles with errors) and theoretical (squares [156] and triangles [83]) values for six transition frequencies of antiprotonic helium [94]. Note the factor 10 and 100 differences in the axis scales. The various contributions from relativistic, QED, and finite-size corrections to the theoretical frequencies are indicated.

One transition $((36, 34) \rightarrow (37, 33))$ at $\lambda = 616.7$ nm, however, was experimentally found to blue-shift with a gradient $d\nu/d\rho = (3.8 \pm 0.5) \times 10^{-21}$ GHz cm³ which did not agree with the theoretical value of -1.90×10^{-21} GHz cm³. This resonance has a large linewidth $\Gamma = 15 \pm 4$ GHz [94, 155] which indicates a short lifetime $\tau = 11 \pm 3$ ps for the daughter state (37, 33). It was theoretically predicted [155] that such a short lifetime is caused by a strong coupling to an electronically excited $\bar{p}\text{He}^+$ state, where the electron occupies the 3d-orbital, and the antiproton the state (32, 31). The above disagreement between the theoretical and experimental values for $d\nu/d\rho$ may be due to the fact that the calculations [135] were made assuming only a single state of 1s electron configuration.

The zero-density frequencies ν_{exp} were obtained by linear extrapolation of the experimental data (figure 23). The various sources of experimental errors on ν_{exp} are shown in table 4. The above extrapolation to $\rho = 0$ introduced a systematic error 20–50 MHz. The statistical error in the spectroscopy signal arising from the small number of $\bar{p}\text{He}^+$ excited by the multimode laser beam was 20–40 MHz. The frequency calibration of the pulsed dye laser had a systematic error 70–140 MHz; better calibration techniques and modifications on the laser later improved this to 20–50 MHz. Any frequency shift due to the residual magnetic field in the target has been calculated to be negligibly small (<1 MHz). Ac Stark shifts (i.e. dynamic shifts in the energy levels caused by the strong laser field polarizing the atomic orbitals of $\bar{p}\text{He}^+$) are also estimated to be very small (<1 MHz). This is because the scalar (-3 to 2 a.u.) and tensor $((0.1-2) \times 10^{-3}$ a.u.) terms of the dynamic polarizability for these transitions are much smaller than for electronic transitions in normal atoms [89]. The final experimental errors are the quadratic sum of all these statistical and systematic errors.

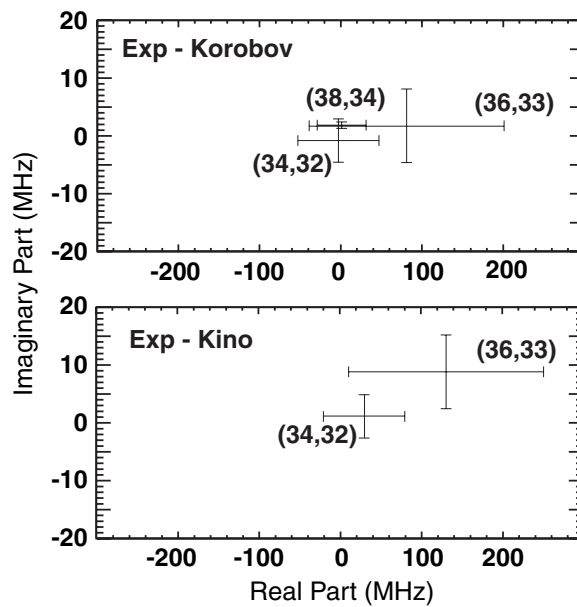


Figure 24. Precise comparison of the complex energies of five $\bar{p}^4\text{He}^+$ states [157]. The difference of the experimental values from the two theories [83, 156] are plotted in MHz. The imaginary part plotted here is half Auger width with negative sign, $-\frac{1}{2}(\Gamma_A/2\pi)$. The values used for the comparison of the real part are the transition energies from the parent metastable states, where the theoretical uncertainty should be very small.

The experimental frequencies of four transitions with natural widths $\Gamma < 50$ MHz agree with the theoretical values within $|\nu_{\text{th}} - \nu_{\text{exp}}|/\nu_{\text{exp}} \leq 5 \times 10^{-7}$, the experimental errors (80–150 MHz) being of the same order as the QED one-loop vacuum polarization effect [78,85]. The differences were much larger ($\geq 1 \times 10^{-6}$) for the two transitions $(37, 34) \rightarrow (38, 33)$ at 713.6 nm and $(36, 34) \rightarrow (37, 33)$ at 616.7 nm, which have linewidths $\Gamma \geq 15$ GHz. The latter transition is particularly difficult to calculate due to the coupling of the state $(37, 33)$ to a broad, electronically excited $\bar{p}\text{He}^+$ state. In figure 24, the difference between the experimental and theoretical complex energies of three $\bar{p}^4\text{He}^+$ states are compared. The real part is here derived from the measurement of the transition frequencies [94, 156], the imaginary part from the Auger width of the resonant daughter state [83, 157]. All of these show good agreement with three-body QED calculations.

It was found that some $\bar{p}^4\text{He}^+$ resonances cannot be observed at high densities ($\rho \geq 10^{20} \text{ cm}^{-3}$) of the helium target, as collisions destroy the antiprotonic populations in some states but not others. According to Auger calculations for a single isolated atom, the state $(32, 31)$ is expected to be the lowest-lying metastable state in the $\nu = 0$ cascade (figure 13). However, the corresponding UV transition $(32, 31) \rightarrow (31, 30)$ at $\lambda = 264.7$ nm could not be observed in this experiment. Instead, the transition $(33, 32) \rightarrow (32, 31)$ at 296.1 nm was detected, which shows that $(32, 31)$ has a short collisional lifetime against antiproton annihilation [94]. In fact, as we shall see below, this state recovered its metastability in experiments carried out at much lower densities $\rho \sim 10^{18} \text{ cm}^{-3}$ [95].

3.5. The radiofrequency quadrupole decelerator

The precision on the $\bar{p}\text{He}^+$ transition frequencies ν in the above experiment was limited by the collisional shifts $\Delta\nu$, and the errors associated with the extrapolation to zero density [94].

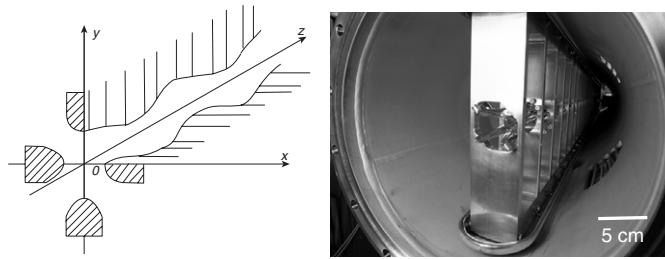


Figure 25. Schematic drawing of the electrode structure of an RFQ (left). Antiprotons injected axially into the ~ 1 cm diameter aperture between the rods are alternately focused and defocused in the two transverse planes. The peaks and troughs machined into the rods provide the decelerating force. Photograph of the RFQD electrodes (right).

Higher-precision measurements could only be carried out if the $\bar{p}\text{He}^+$ were produced in an ultra-low density (e.g. $\rho \sim 10^{17} \text{ cm}^{-3}$) target, where collisional shifts would become negligible compared with the 10 MHz scale natural widths of the transitions. Such experiments would require an antiproton beam of sufficiently low energy (e.g. $E \sim 100 \text{ keV}$) that could be efficiently stopped in the low-density target. For this purpose, the CERN PS division [158] with the ASACUSA collaboration developed a radiofrequency quadrupole decelerator (RFQD), which decelerated the 5.3 MeV antiprotons used above to energies $E = 10\text{--}120 \text{ keV}$.

The principle of the RFQD is as follows [158]. As described in the previous sections, deceleration of an antiproton beam implies an increase in its physical emittance. In the absence of cooling, the beam diameter would normally increase until the antiprotons strike the inner walls of the accelerator. One way to avoid these losses is to strongly focus the beam during deceleration, as is done in the RFQD. The RFQD [158] consisted of four 3.4 m long rod electrodes arranged in a quadrupole configuration, which were excited by a quadrupole RF field of $f \sim 202.5 \text{ MHz}$ (figure 25). The high field (corresponding to a voltage on the rod electrodes of $\sim 170 \text{ kV}$) was achieved by placing the rods in a cylindrical cavity which was suitably designed to resonate at the required TE₂₁₀ (i.e. transverse electric quadrupole) mode. Antiprotons injected axially into the ~ 1 cm diameter aperture between the rods were thus alternately focused and defocused in the two transverse planes (as in the case of a Paul trap or quadrupole mass spectrometer [159]) with a maximum electric field $\sim 30 \text{ MV m}^{-1}$. This ‘alternate gradient’ focusing resulted in a net confining effect, which ensured that the antiprotons followed orbits of small transverse diameter that oscillate around the RFQD axis.

To generate a longitudinal component of the RF field which decelerated the antiprotons, a series of peaks and troughs were machined on the surfaces of the rods. The axial positions of the peaks were the same for opposing pairs of rods, but shifted by half a period between neighboring rods. This deviated the originally transverse electric fields into the longitudinal direction and gave rise to a standing wave along the RFQD axis, the wavelength λ_r of which was determined by the pitch of these rod undulations. The λ_r -value was adjusted to correspond to the flight distance of an antiproton during a single 202.5 MHz RF cycle, which gradually decreased as the beam was decelerated from $E = 5.3 \text{ MeV}$ to 65 keV along the RFQD. Antiprotons injected into the RFQD with the correct timing relative to the RF phase were thus decelerated each time they traversed a rod undulation (figure 26).

The RFQD was operated in the following way. A RF bunching cavity first shaped the antiproton beam extracted from AD into a train of micropulses, with a pulse length ($\Delta t = 300 \text{ ps}$) and relative timing to the RF phase, which were compatible with the above requirements for deceleration. The antiprotons then entered the RFQD, and some $\sim 30\%$ were

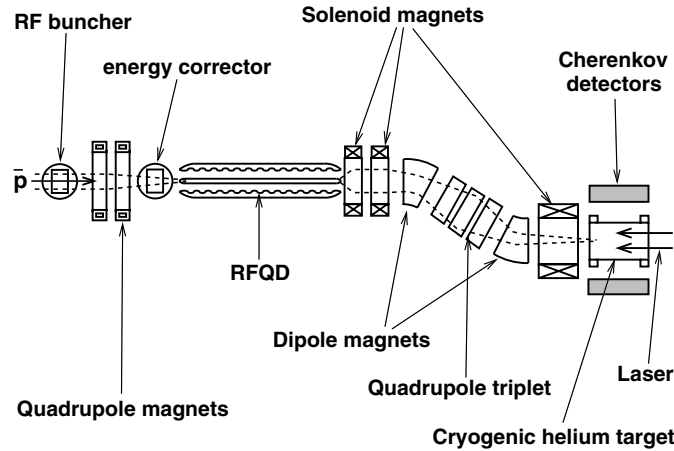


Figure 26. Experimental layout of the radiofrequency quadrupole decelerator and the laser spectroscopy experiment of $\bar{p}\text{He}^+$. Antiprotons decelerated to energy $E \sim 100$ keV in the RFQD are transported by the achromatic momentum analyzer to the cryogenic helium target [95]. The $\bar{p}\text{He}^+$ produced in the target are irradiated by a resonant laser beam. Dashed lines indicate trajectories of the antiproton beam. Drawing not to scale.

emitted with energy $E = 65$ keV; the remaining 70% emerged with little or no deceleration. The antiproton output energy could be varied between $E = 10$ and 120 keV by biasing the electrodes of the RFQD with a dc potential. An energy-correcting RF cavity at the input of the RFQD was used to compensate for the changes in the energy of the incident beam resulting from this biasing, and variations in the energy of the antiprotons extracted from the AD.

3.6. Direct measurement of the transition frequencies of isolated $\bar{p}\text{He}^+$

The RFQD enabled direct measurements of the transition frequencies ν of isolated $\bar{p}\text{He}^+$ at target density $\rho \sim 5 \times 10^{17} \text{ cm}^{-3}$ (i.e. under idealized conditions wherein the collisional shifts $\Delta\nu$ became negligible), as follows. A beam of 100 keV antiprotons emitted from the RFQD was first diverted by an achromatic momentum analyzer connected to its output, and focused into the entrance of a cryogenic helium target. This diversion eliminated the large background that the undecelerated antiprotons would have otherwise produced. The spatial profiles of antiproton pulses along the beam line were measured non-destructively by micro-wire secondary electron emission detectors [160]. To ensure that the antiprotons would stop in the low-density helium gas (corresponding to pressure $P = 0.7\text{--}2$ mbar and temperature $T = 12\text{--}30$ K), the target volume was made much larger (diameter $d = 15$ cm, length $l = 30$ cm) than in the 5.3 MeV experiments described above. The antiprotons which entered through a $0.8 \mu\text{m}$ thick polyethylene window mounted on one end of the chamber formed $\bar{p}\text{He}^+$ atoms filling the entire volume of the target. These atoms were irradiated by a 5 cm diameter laser beam which entered through a fused silica window. The other details (Cherenkov counters and lasers) were similar to the above 5.3 MeV experiments.

At the very low densities studied in these experiments ($\rho = 5 \times 10^{17} \text{ cm}^{-3}$), the $\bar{p}^4\text{He}^+$ (figure 27(a)) and $\bar{p}^3\text{He}^+$ had average lifetimes against annihilation of $\tau_{\text{avg}} = 5 \mu\text{s}$ and $4 \mu\text{s}$, respectively. This is $1\text{--}2 \mu\text{s}$ longer than the values measured in the above experiments carried out at higher densities $\rho > 10^{20} \text{ cm}^{-3}$. Laser spectroscopy revealed that certain states became long-lived, due to the reduced rate of collisions. For example, as described above the $\bar{p}^4\text{He}^+$

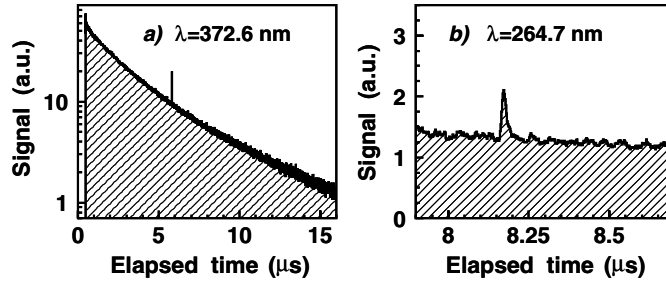


Figure 27. Delayed annihilation time spectra of $\bar{p}^4\text{He}^+$ measured at ultra-low densities $\rho \sim 5 \times 10^{17} \text{ cm}^{-3}$, with laser-induced annihilation spikes of the transitions $(35, 33) \rightarrow (34, 32)$ (a) and $(32, 31) \rightarrow (31, 30)$ (b). The latter transition could not be observed at higher densities [95].

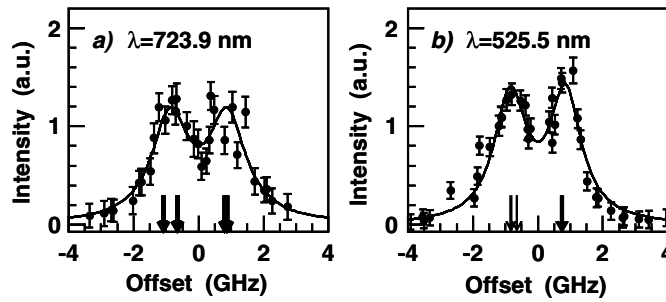


Figure 28. Frequency profiles of $\bar{p}^3\text{He}^+$ transitions $(36, 34) \rightarrow (37, 33)$ (a) and $(34, 33) \rightarrow (35, 32)$ (b). Arrows denote theoretical positions of the substructure due to spin interactions. Here there are eight, partially overlapping hyperfine components, arranged in three groups [162].

transition $(32, 31) \rightarrow (31, 30)$ at 264.7 nm could not be previously detected because state $(32, 31)$ was found to have a lifetime two orders of magnitude shorter than the theoretically expected value. It was detected at the low densities of the RFQD experiment, however, indicating the recovery of its metastability. This result showed that the $\bar{p}\text{He}^+$ are now indeed produced in a near-isolated condition.

In figure 28(a), the resonance profile of the $\bar{p}^3\text{He}^+$ transition $(n, \ell) = (36, 34) \rightarrow (37, 33)$ at $\lambda = 723.9 \text{ nm}$ is shown. As in the above $\bar{p}^4\text{He}^+$ case, the hyperfine splitting $\Delta_{\text{HFS}} = 1.8 \pm 0.1 \text{ GHz}$ between the two peaks caused by the dominant interaction between the antiproton magnetic moment and the electron spin agreed with theoretical calculations [96, 161]. In figure 28(b), the profile of the transition $(34, 33) \rightarrow (35, 32)$ at 525.5 nm is shown, with a corresponding splitting $\Delta_{\text{HFS}} = 1.6 \pm 0.1 \text{ GHz}$. Now the theoretical discussion in section 2.4.3 and figure 8 shows that these profiles are a superposition of eight partially overlapping lines arranged in three groups, the calculated positions of which are shown in arrows. These further hyperfine structures cannot be resolved here due to the Doppler broadening effect in the observed spectra and the limited resolution of the laser. However in the case of the $\lambda = 525.5 \text{ nm}$ resonance, the resolution is slightly better than the 723 nm case and reveals an asymmetry in the profile caused by the uneven spacings among the peaks. This asymmetry was clearly observed in later experiments (see below).

The spin-independent transition frequencies ν_{exp} were extracted from these spectra, by fitting the profiles with four (in the case of the $\bar{p}^4\text{He}^+$ data) or eight ($\bar{p}^3\text{He}^+$) Voigt functions (solid lines), superimposed on each other and separated by the theoretical hyperfine splittings.

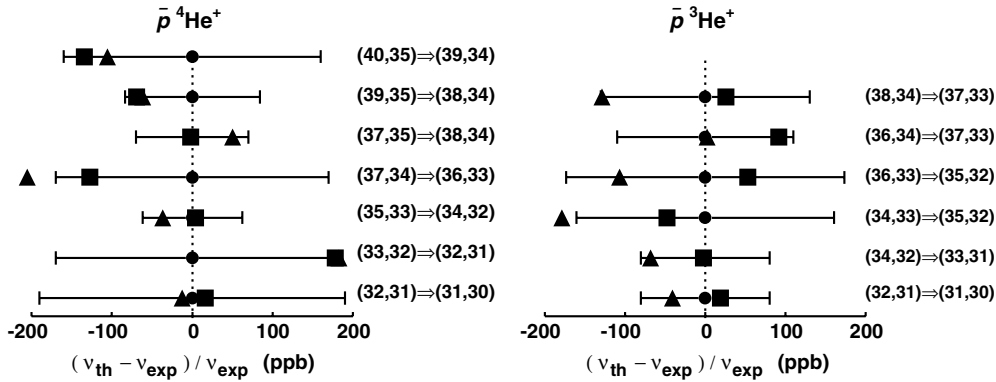


Figure 29. Comparisons between experimental ν_{exp} (filled circles with errors) and theoretical ν_{th} (squares [81] and triangles [96]) transition frequencies [95].

Compared with the initial measurements [94] using the direct 5.3 MeV beam of AD, this new series of experiments using the RFQD improved the precision by nearly eliminating the systematic error associated with the density extrapolation (table 4). Nevertheless, there remained a small collisional shift of around 0.1–4 MHz depending on the transition, which was corrected to obtain the final *in vacuo* result. The precision of the laser frequency calibration was also slightly improved. All other sources of statistical and systematic errors remained at a similar level, which finally led to an experimental precision of $(6\text{--}19) \times 10^{-8}$, the highest being for the $\bar{p}^4\text{He}^+$ transition $(35, 33) \rightarrow (34, 32)$ at 372.6 nm. In figure 29, the frequencies are compared with the results ν_{th} of theoretical calculations [77, 81, 96, 163], the precisions of which have been improved compared with those of those shown in figure 23. In the previous 5.3 MeV experiment [94], a theory–experiment difference of $|(\nu_{\text{th}} - \nu_{\text{exp}})/\nu_{\text{exp}}| \sim (5\text{--}7) \times 10^{-7}$ was observed in the $\bar{p}^4\text{He}^+$ transition $(39, 35) \rightarrow (38, 34)$ at 597.3 nm; as a result of these experimental and theoretical improvements, the difference was now reduced to $< 8 \times 10^{-8}$.

3.7. Higher precision: cw pulse-amplified laser locked to a frequency comb

Having thus eliminated the collisional shift in the measured $\bar{p}\text{He}^+$ frequencies, further improvements in the experimental precision (table 4) now required a higher-precision laser system and more advanced techniques to stabilize the optical frequency. As we have seen in figure 17, only pulsed lasers can provide the megawatt-scale intensities needed to induce the $\bar{p}\text{He}^+$ transitions. Pulsed lasers are, however, characterized by large fluctuations in their frequency and linewidth, and it is difficult to calibrate them over the wide range of $\bar{p}\text{He}^+$ wavelengths $\lambda = 264.7\text{--}726.1$ nm [138]. These problems were circumvented in the latest series of $\bar{p}\text{He}^+$ experiments [51], which were based on a continuous-wave (cw) laser whose frequency could be stabilized with a precision $< 4 \times 10^{-10}$ against an optical frequency comb generator [164–166]. Its intensity was then amplified [167–169] by a factor of 10^6 to produce a pulsed beam with an accuracy and resolution of 1–2 orders of magnitude higher (table 4) than before.

Many commercially available cw lasers can easily achieve a spectral resolution of < 4 MHz, and even $\ll 100$ kHz with appropriate modifications to the laser cavity. This is why they are used to carry out laser spectroscopy at the highest precision (e.g. on the 1s–2s transition of atomic hydrogen [170]). It is the continuous nature of the laser output which enables this precision; the frequency stabilization in cw lasers is typically carried out by monitoring the

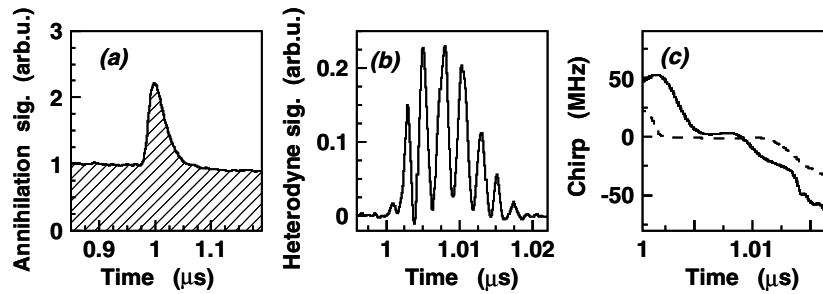


Figure 31. (a) Delayed annihilation time spectrum of $\bar{p}^4\text{He}^+$ with laser-induced transition $(n, \ell) = (39, 35) \rightarrow (38, 34)$, (b) heterodyne beat signal of the pulsed dye laser, (c) time evolution of frequency chirp with (broken line) and without (solid) chirp compensation [51].

of, e.g. molecular hydrogen [171, 172], helium [167, 173], muonium [174, 175], and positronium [176]. These methods have now been employed [51] to measure 12 transitions in $\bar{p}\text{He}^+$, the annihilation peak of one ($\bar{p}^4\text{He}^+$ resonance $(n, \ell) = (39, 35) \rightarrow (38, 34)$ at wavelength $\lambda = 597.3$ nm) of which is shown in figure 31(a). The time evolution of the chirp $\Delta\nu_c(t)$ in the laser pulse used to excite this transition was derived in the following way. Part of the seed laser was diverted into an acousto-optic modulator (AOM), which shifted its frequency by precisely $\nu_{\text{aom}} = 400$ MHz. The resulting cw and pulsed dye laser beams of frequencies $\nu_{\text{cw}} + \nu_{\text{aom}}$ and ν_{pl} were merged and superimposed on a photodiode. The heterodyne beat signal (figure 31(b)) measured by the photodiode contained the difference frequency between the two lasers, i.e. $\nu_{\text{pl}} - \nu_{\text{cw}} - \nu_{\text{aom}}$, which was isolated by Fourier analysis [167, 168]. Under idealized conditions of zero frequency chirp $\Delta\nu_c = 0$, the carrier frequency of the beat signal (figure 31(b)) would be equal to $\nu_{\text{aom}} = 400$ MHz. Any non-zero value of $\Delta\nu_c$, however, would appear as a deviation from 400 MHz, which can then be precisely measured. In figure 31(c), the chirp in a 597.3 nm laser pulse obtained in this way is shown in solid lines. It changed from $\Delta\nu_c(t) = 50$ to -70 MHz over its 20 ns duration.

The chirp can be minimized by using an electro-optic modulator (EOM) to apply an artificial frequency shift of opposite sign to the cw seed laser before amplification. This ‘anti-chirp’ cancels the subsequent chirp (broken lines) induced in the dye cells [167, 169, 175], so that the effective $\Delta\nu_c(t)$ -value is reduced to <10 MHz over most of the pulse. Any remaining effect that the small residual chirp $\Delta\nu_c(t)$ has on the measured $\bar{p}\text{He}^+$ profile can then be evaluated and corrected by numerical simulation (see below), so that the transition frequency ν_{exp} can be precisely determined.

We now describe the absolute calibration of the cw laser frequency ν_{cw} . Until recently, the only practical way of calibrating laser frequencies with precision $<10^{-7}$ in such accelerator-based experiments was to compare them against secondary atomic or molecular standards, as was done in the previous two $\bar{p}\text{He}^+$ measurements [94, 95]. This method has the following constraints; however, (i) the frequency of the reference line must of course be known with sufficiently high accuracy, but relatively few such lines with precisions $<10^{-7}$ exist, (ii) laser spectroscopy of this atomic or molecular reference line must be carried out during the $\bar{p}\text{He}^+$ experiment. The many possible systematic errors from, e.g. collisional or power shifts in the I_2 or Rb spectroscopy [148] must be minimized, (iii) the reference line must typically lie within a few tens of GHz of the target $\bar{p}\text{He}^+$ one. In fact, it was found that very few $\bar{p}\text{He}^+$ lines had any corresponding reference which would allow spectroscopy at precisions $<10^{-7}$. One of the authors (MH) therefore began constructing a portable laser spectroscopy system, which could be transported between CERN in Geneva and, e.g. NIST in Colorado, to calibrate all 12 $\bar{p}\text{He}^+$

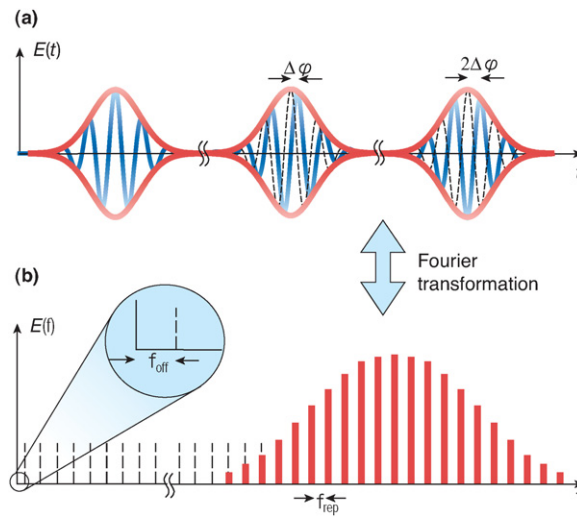


Figure 32. (a) Train of consecutive laser pulses with repetition rate f_{rep} generated by the optical frequency comb. The optical carrier wave in successive laser pulses are shifted by a phase angle $\Delta\phi$. (b) Frequency spectrum of comb, with the cycle slip frequency $f_{\text{off}} = \Delta\phi f_{\text{rep}}$ [164].

lines. These efforts became obsolete, however, with the invention of the optical frequency comb in 1999–2000, which provided an accurate frequency standard over the entire optical region.

The frequency comb [164, 166] (figure 32(a)) essentially consists of a laser cavity of length L , within which circulates a single laser pulse of optical carrier frequency f_c and femtosecond duration (i.e. much shorter than the nanosecond-scale round-trip time $T_r = 2L/c$ of the laser light in the cavity). The output of this laser is therefore a train of pulses with identically shaped envelopes, which are separated by a repetition rate $f_{\text{rep}} = T_r^{-1}$. When we carefully examine each pulse, however, we find that the optical carrier waves in successive laser pulses are shifted by increments of the phase angle $\Delta\phi$ with respect to the pulse envelope. This shift arises from dispersion effects in the optical components in the cavity, which causes a slight difference in the carrier and group velocities of the laser pulse circulating inside. The essential point here is that both f_{rep} and $\Delta\phi$ can be measured and precisely stabilized by adjusting the pump power of the femtosecond laser, and some optical elements in the laser cavity [165].

Fourier transformation of this train of laser pulses reveals a series of sharp spikes in the optical frequency domain, which are separated by an interval f_{rep} (figure 32(b)). This comb structure corresponds to many thousands of modes in the laser cavity oscillating in unison. The mode positions are shifted from being exact harmonics of the carrier frequency f_c by an offset $f_{\text{off}} = \Delta\phi f_{\text{rep}}$ (figure 32(b)); we call this the cycle slip frequency. The frequency of the n th mode of the comb is then

$$f_n = f_{\text{off}} + n f_{\text{rep}}. \quad (39)$$

By stabilizing both f_{off} and f_{rep} against an atomic clock, the optical frequency of the comb modes can reach absolute accuracies better than 1 part in 10^{15} [177].

The comb (Menlo Systems GmbH FC-8004) used in these experiments (figure 30) consisted [165] of a mode-locked Ti:sapphire laser pumped by a cw Nd:YVO₄ laser (A), which produced a train of 15 fs long laser pulses of repetition rate $f_{\text{rep}} = 200$ MHz, cycle slip frequency $f_{\text{off}} = 20$ MHz and a spectral width extending between $\lambda = 750$ and 850 nm. This

infrared light was sent through a microstructure fiber [164–166], wherein non-linear effects broadened the spectral width of the comb over the entire region $\lambda = 500\text{--}1100$ nm needed to calibrate all the $\bar{p}\text{He}^+$ lines.

The frequency ν_{cw} of the cw seed laser was compared [51, 165] with the above comb and stabilized to a value,

$$\nu_{\text{cw}} = n_c f_{\text{rep}} + f_{\text{off}} + f_{\text{dif}}, \quad (40)$$

which was $f_{\text{dif}} = 20$ MHz above the n_c th mode of the comb. The laser frequencies used to measure these $\bar{p}\text{He}^+$ transitions corresponded to mode numbers $n_c = 1\,592\,190\text{--}2\,607\,811$ of the comb. All radio frequencies f_{rep} , f_{off} and f_{dif} were synchronized to a quartz oscillator, which was stabilized to a reference clock provided by global positioning satellites. The seed (and consequently the pulsed dye) laser was scanned over a region ± 4 GHz around the $\bar{p}\text{He}^+$ resonances by changing the repetition rate of the femtosecond laser from $f_{\text{rep}} = 200.000$ to 200.004 MHz to which it was stabilized. Doppler-free spectroscopy of Rb and I_2 in the seed beam indicated that its frequency precision was $< 4 \times 10^{-10}$ [178]. A thermally stabilized, hermetically sealed housing permitted 24 h operation of the comb during these months-long experiments, and motorized stages optimized the alignment and polarization of the beam coupled into the fiber during the 100 s intervals between antiproton pulses [51].

3.8. Parts-per-billion-scale laser spectroscopy of $\bar{p}\text{He}^+$

The above laser system was used in conjunction with the RFQD to measure 12 transition frequencies in $\bar{p}^3\text{He}^+$ and $\bar{p}^4\text{He}^+$ to fractional precisions between 9 and 16 parts in 10^9 [51]. All the experiments were carried out using a linearly polarized laser beam. A typical profile of the resonance $(n, \ell) = (36, 34) \rightarrow (37, 33)$ in $\bar{p}^3\text{He}^+$ is shown in figure 34(a), and demonstrates the much higher resolution and precision compared with the previous such measurements of figures 28 and 15. The width of this profile is now dominated by the thermal Doppler broadening of ~ 400 MHz, which is probed by a laser of much higher (~ 60 MHz) resolution. The two peaks separated by 1.8 GHz and asymmetry due to the hyperfine structure can be clearly resolved.

At the higher levels of precision involved in this measurement, it was no longer sufficient to simply fit the profile with Voigt functions as in previous experiments [94, 95] to determine the spin-averaged transition frequency ν_{exp} . A more sophisticated simulation was made to obtain the exact shape of the profile. Each state (n, ℓ) in $\bar{p}^3\text{He}^+$ has eight hyperfine substates [96, 161], which are distinguished by the configurations of the electron, antiproton, and ^3He spins. The profile of figure 34(a) therefore contains eight intense lines (the calculated position [161] of which are indicated by arrows), corresponding to $E1$ transitions between the eight substates of the states $(36, 34)$ and $(37, 33)$ involving no spin-flip. In addition, there are 12 lines which are weaker by more than 2 orders of magnitude, wherein one of the constituent particles flips its spin. The theoretical lineshape was obtained by integrating a series of optical Bloch equations (equation (35)) for all such possible $E1$ transitions. The equations for hundreds of laser transitions between the many magnetic m -substates were simultaneously solved [179]. The frequency chirp $\Delta\nu_c(t)$ introduced a time dependence to the driving laser frequency when performing the Bloch equation integration. The Doppler broadening laser power broadening, and dephasing collision effects were also taken into account. This lineshape was then fitted to the profile (solid line) to determine ν_{exp} . The ν_{exp} -values of $\bar{p}^4\text{He}^+$ resonances (figure 34(b)), which contain four intense, non-spin-flip hyperfine lines and four weak, spin-flip ones were obtained similarly.

All transitions heretofore accessible to precision laser spectroscopy involved a daughter state with a short Auger lifetime, the natural width $\Gamma_n \geq 20$ MHz [81, 126] of which would

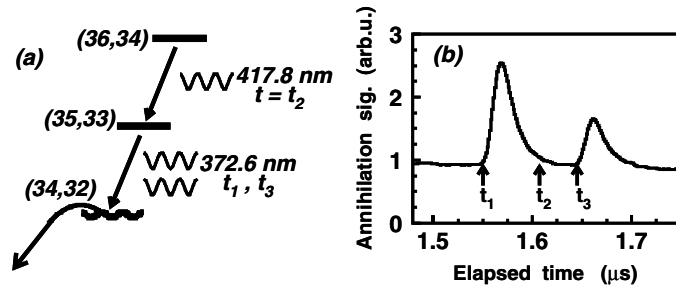


Figure 33. (a) Portion of energy level diagram of $\bar{p}^4\text{He}^+$, (b) delayed annihilation time spectrum with three lasers fired at t_1 – t_3 to measure 417.8 nm transition (see text) [51].

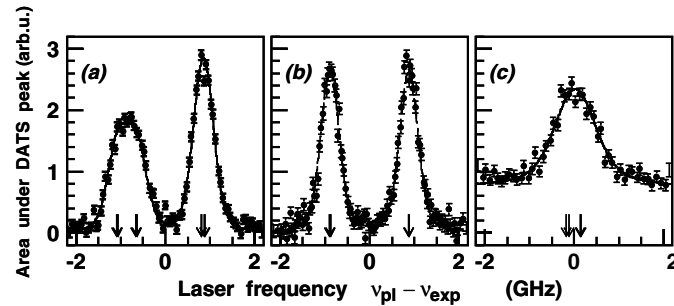


Figure 34. Frequency profiles of the transition (a) $(36, 34) \rightarrow (37, 33)$ in $\bar{p}^3\text{He}^+$, (b) $(37, 35) \rightarrow (38, 34)$ and (c) $(36, 34) \rightarrow (35, 33)$ in $\bar{p}^4\text{He}^+$, measured using cw pulse-amplified dye laser stabilized to an optical frequency comb [51].

ultimately limit the achievable precision on ν_{exp} to around $\sim 10^{-9}$. A different technique was introduced to extend the studies to a $\bar{p}^4\text{He}^+$ transition $(36, 34) \rightarrow (35, 33)$ between two metastable states with $\Gamma_n \sim 100$ kHz. This implies an ultimate precision of $\sim 10^{-12}$, although these experiments are Doppler rather than natural width limited. To measure this transition, the following three-laser method was developed (figure 33(a)), (i) an additional dye laser (E in figure 30) pumped by a 355 nm Nd:YAG laser (D) first irradiated the $\bar{p}\text{He}^+$ with a 372.6 nm laser pulse. This depleted the population in state (35, 33) at t_1 by inducing the transition $(35, 33) \rightarrow (34, 32)$ to a short-lived state, and thereby producing the first peak in figure 33(b), (ii) at $t = t_2$, the cw pulse-amplified laser tuned to $(36, 34) \rightarrow (35, 33)$ at $\lambda = 417.8$ nm equalized the population in the parent and daughter states, (iii) another 372.6 nm dye laser (F) pumped by the same Nd:YAG laser after a 100 ns delay probed the increased population of (35, 33) at $t = t_3$ resulting from the transitions stimulated by the 417.8 nm laser pulse, and produced an annihilation peak at $t = t_3$. The profile of the $(36, 34) \rightarrow (35, 33)$ resonance obtained by plotting the intensity of this peak against the frequency of the 417.8 nm laser is shown in figure 34(c).

The *in vacuo* values $\nu_{exp}(\rho = 0)$ were obtained by correcting the experimental results using shift between $\Delta\nu = -14$ and 1 MHz corresponding to target density $\rho \sim 2 \times 10^{18} \text{ cm}^{-3}$. As described above, theoretical calculations [89] show that shifts due to the ac Stark effect or residual magnetic fields in the target are negligibly small (table 4). The experimental 1-standard deviation error σ_{exp} was the quadratic sum of the statistical component associated with the above fit (3–13 MHz), together with the systematic component σ_{syst} arising from the

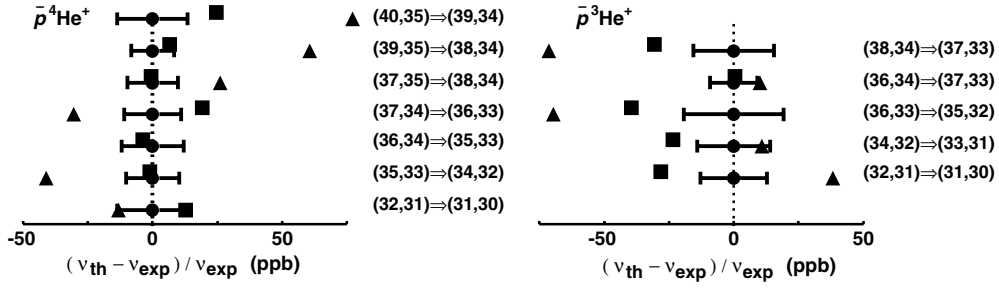


Figure 35. Experimental ν_{exp} (circles with 1σ errors) versus theoretical ν_{th} (triangles [126] and squares [82, 89]) transition frequencies [51].

chirp (2–4 MHz), collisional shifts (0.1–2 MHz) and any possible shift due to the harmonic generation (1–2 MHz).

The ν_{exp} -values agree with the two previous experiments [94, 95] within the order of magnitude lower precision of the latter. They are compared with the two sets of theoretical values ν_{th} [82, 126] in figure 29; the latest values of [82] claims a precision $\sigma_{\text{th}} = 1\text{--}2$ MHz. The older values of [126] is claimed by the authors to have σ_{th} -values of between 5 and 100 MHz, because of technical difficulties in evaluating their variational trial functions near the origin (where the distance r between the constituent particles approaches zero). Indeed, unpublished results from the authors have recently moved by 3–100 MHz from those of [126]. Only the values of [82] claim precisions consummate with our experimental errors, and were therefore used in the *CPT*-related analysis described in the next section.

When compared with experiment, the values from [126] scatter within 7–8 standard deviations of ν_{exp} . Those of [82, 89] agree within $<1 \times 10^{-8}$ with the four highest-precision measurements in $\bar{p}^4\text{He}^+$, and (36, 34) \rightarrow (37, 33) in $\bar{p}^3\text{He}^+$. Four calculated $\bar{p}^3\text{He}^+$ -frequencies were lower than the ν_{exp} -values by ~ 2 standard deviations (figure 35).

4. The mass and charge of the antiproton

From the comparison of the measured transition frequencies ν_{exp} and the theoretically calculated ones [82] ν_{th} using the 2002 CODATA recommended values for the fundamental constants [50], the mass (and charge) of the antiproton can be deduced. This is done by varying $m_{\bar{p}}$ in the theoretical model, initially set to the m_p value, and performing the χ^2 -minimization.

We here examine two possibilities to utilize the $\bar{p}\text{He}^+$ data (1) to determine \bar{p} -to-electron mass ratio (and then compare the value with m_p/m_e) and (2) to test *CPT*. There are subtle but important differences between the two.

When deducing the \bar{p} -to-electron mass ratio, we assume that the *CPT* invariance is not violated yet at the present experimental precision. We therefore set $Q_p + Q_{\bar{p}} = 0$, and vary $m_{\bar{p}}/m_e$ in the theory model, and seek for the best fit. The obtained $m_{\bar{p}}/m_e$, if enough precision is attained, can be used together with the current m_p/m_e values in the future CODATA adjustments of the fundamental constants.

On the other hand, in the *CPT* test, we test if there is any difference between m_p and $m_{\bar{p}}$ and between Q_p and $|Q_{\bar{p}}|$. We therefore let $m_{\bar{p}}$ to vary relative to m_p (which implies that $m_{\bar{p}}$ is also changed relative to m_{He}) and let $|Q_{\bar{p}}|$ to vary relative to Q_p . The minimization procedure makes it possible to set a *CPT* bound in the $\delta m_{\bar{p}} - \delta Q_{\bar{p}}$ two-dimensional plane.

Let us first discuss the case 1, determination of $m_{\bar{p}}/m_e$.

4.1. Determination of the antiproton-to-electron mass ratio

For a small possible variation of $m_{\bar{p}}$ which is being studied, it is possible to evaluate the sensitivity coefficients, $\partial E/\partial(\delta m_{\bar{p}})$ for each (n, ℓ) state of $\bar{p}\text{He}^+$, and use a linearized expression when performing the χ^2 minimization.

The non-relativistic Hamiltonian of $\bar{p}\text{He}^+$ in atomic units, equation (11) can be rewritten by defining symbols for mass ratios, such that $\eta_{32} \equiv m_3/m_2(=m_e/m_{\bar{p}})$ and $\eta_{21} \equiv m_2/m_1(=m_{\bar{p}}/m_{\text{He}})$. With these definitions, the reduced masses in the Hamiltonian equation (11) can be written as [82]

$$\frac{1}{2\mu_{12}} = \frac{(1 + \eta_{21})\eta_{32}}{2}, \quad \frac{1}{2\mu_{13}} = \frac{1 + \eta_{21}\eta_{32}}{2} \quad \text{and} \quad \frac{m_3}{m_1} = \eta_{21}\eta_{32}. \quad (41)$$

Then the derivatives of the level energy with respect to the particle-mass changes become

$$\frac{\partial E_0}{\partial \eta_{32}} = -\frac{1 + \eta_{21}}{2} \langle \nabla_1^2 \rangle - \frac{\eta_{21}}{2} \langle \nabla_2^2 \rangle - \eta_{21} \langle \nabla_1 \nabla_2 \rangle, \quad (42)$$

$$\frac{\partial E_0}{\partial \eta_{21}} = -\frac{\eta_{32}}{2} \langle \nabla_1^2 \rangle - \frac{\eta_{32}}{2} \langle \nabla_2^2 \rangle - \eta_{32} \langle \nabla_1 \nabla_2 \rangle. \quad (43)$$

where $\langle \dots \rangle$ s denote expectation values.

In terms of fractional changes such as $\Delta\eta_{32}/\eta_{32}$, the level energy shift ΔE_0 becomes

$$\Delta E_0 = a_{32} \left(\frac{\Delta\eta_{32}}{\eta_{32}} \right) + a_{21} \left(\frac{\Delta\eta_{21}}{\eta_{21}} \right), \quad (44)$$

where we have defined the sensitivity coefficients a_{32} and a_{12} as

$$a_{32} \equiv \eta_{32} \left(\frac{\partial E_0}{\partial \eta_{32}} \right) \quad \text{and} \quad a_{21} \equiv \eta_{21} \left(\frac{\partial E_0}{\partial \eta_{21}} \right). \quad (45)$$

With these coefficients, the change in the transition energy ΔE from the initial state (i) to the final state (f) can be written as

$$\Delta E = \Delta E_0^i - \Delta E_0^f = \left[(a_{32}^i - a_{32}^f) \left(\frac{\Delta\eta_{32}}{\eta_{32}} \right) + (a_{21}^i - a_{21}^f) \left(\frac{\Delta\eta_{21}}{\eta_{21}} \right) \right], \quad (46)$$

or in terms of the fractional frequency change,

$$\frac{\Delta\nu}{\nu} = \alpha_{23}^{\text{if}} \left(\frac{\Delta\eta_{23}}{\eta_{23}} \right) + \alpha_{21}^{\text{if}} \left(\frac{\Delta\eta_{21}}{\eta_{21}} \right), \quad (47)$$

where the α s in the last equation are

$$\alpha_{23}^{\text{if}} = -\frac{(2R_{\infty}c)(a_{32}^i - a_{32}^f)}{\nu} \quad (48)$$

and

$$\alpha_{21}^{\text{if}} = \frac{(2R_{\infty}c)(a_{21}^i - a_{21}^f)}{\nu}, \quad (49)$$

and note that we used η_{23} instead of η_{32} (and hence α_{23} has an opposite sign with respect to a_{32}) since we will be deducing the (anti)proton-to-electron mass ratio in what follows.

The first term of equation (47) expresses the sensitivity of the transition frequency on the antiproton(2)-to-electron(3) mass ratio, while the second term is that on the antiproton(2)-to-helium(1) mass ratio. In the present framework of $m_{\bar{p}}/m_e$ determination, only the first term is relevant.

Table 6. The CODATA2002 recommended values for the mass ratios relevant to $\bar{p}\text{He}$: m_α —alpha particle mass, m_h —helion (${}^3\text{He}$ nucleus) mass, m_p —proton mass and m_e —electron mass.

Quantity	Value	Relative standard uncertainty
m_α/m_p	3.972 599 689 07(52)	1.3×10^{-10}
m_h/m_p	2.993 152 667 1(58)	1.9×10^{-9}
$m_p/m_e \equiv \eta_{23} \equiv 1/\eta_{32}$	1836.152 672 61(85)	4.6×10^{-10}

Table 7. Comparison of measured transition frequencies (in MHz) with Korobov's calculated ones. The α s and β s are the mass and charge sensitivity coefficients (see text).

n_i	ℓ_i	n_f	ℓ_f	$\nu_{\text{exp}}(\sigma_{\text{tot.}})(\sigma_{\text{stat.}})(\sigma_{\text{syst.}})$	$\nu_{\text{th}}(\sigma_{\text{th}})(\sigma_{\text{num.}})$	α_{23}^{if}	α_{21}^{if}	β_2^{if}
For $\bar{p}{}^4\text{He}^+$								
40	35	39	34	445 608 558(6)(6)(3)	445 608 568.6(1.2)(0.8)	1.86	-0.37	3.10
39	35	38	34	501 948 752(4)(4)(2)	501 948 754.9(1.3)(0.5)	1.80	-0.36	3.03
37	35	38	34	412 885 132(4)(3)(2)	412 885 132.0(2.3)(0.3)	2.61	-0.53	4.01
37	34	36	33	636 878 139(8)(6)(4)	636 878 151.6(1.3)(0.3)	1.63	-0.33	2.83
36	34	35	33	717 474 004(10)(9)(4)	717 474 001.2(1.3)(0.4)	1.55	-0.31	2.73
35	33	34	32	804 633 059(8)(7)(4)	804 633 058.1(1.0)(0.3)	1.47	-0.29	2.63
32	31	31	30	1 132 609 209(15)(14)(7)	1 132 609 223.5(1.2)(0.2)	1.27	-0.25	2.38
For $\bar{p}{}^3\text{He}^+$								
38	34	37	33	505 222 296(8)(8)(2)	505 222 280.1(1.3)(0.3)	1.82	-0.46	3.05
36	34	37	33	414 147 508(4)(3)(2)	414 147 508.0(2.2)(0.2)	2.64	-0.66	4.05
36	33	35	32	646 180 434(12)(11)(4)	646 180 407.7(1.4)(0.4)	1.65	-0.41	2.85
34	32	33	31	822 809 190(12)(11)(4)	822 809 170.7(1.2)(0.2)	1.47	-0.37	2.64
32	31	31	30	1 043 128 609(13)(13)(4)	1 043 128 579.6(1.1)(0.1)	1.32	-0.33	2.45

To be more precise, in this treatment, it is the electron mass which is being varied with respect to *both* \bar{p} and helium nucleus, as we keep the \bar{p} -to-helium mass ratio constant. This makes sense since the proton (and hence antiproton) to α mass ratio is known to a better precision than the proton-to-electron mass ratio as shown in table 6. It is the electron mass which is less well known with respect to others⁴.

Table 7 compares the experimentally obtained transition frequencies ν_{exp} to Korobov's theory values ν_{th} calculated with the 2002 CODATA recommended values. The experimental values ν_{exp} are shown together with statistical ($\sigma_{\text{stat.}}$), systematic ($\sigma_{\text{syst.}}$) and total ($\sigma_{\text{tot.}} = \sqrt{\sigma_{\text{stat.}}^2 + \sigma_{\text{syst.}}^2}$) errors, the details of which were discussed in the previous section. The theoretical values ν_{th} are shown together with uncertainties due to yet-to-be-calculated higher-order terms (σ_{th}) and numerical uncertainties ($\sigma_{\text{num.}}$). The table also shows the α_{23}^{if} and α_{21}^{if} sensitivity coefficients for the transition frequencies, as well as the charge sensitivity factor β_2^{if} which will be discussed in the next section. In calculating the α and β factors listed in table 7, we made use of a complete set of mass and charge sensitivity factors calculated for each (n, ℓ) level, provided by Korobov [180] and are tabulated in table 8.

Figure 36 shows how $(\nu_{\text{th}}(\Delta\eta_{23}) - \nu_{\text{exp}})/\nu_{\text{exp}}$ changes when the \bar{p} -to-electron mass ratio ($\eta_{23} \equiv 1/\eta_{32}$) is varied, for one of the $\bar{p}{}^4\text{He}^+$ favored transitions $(36, 34) \rightarrow (35, 33)$ and an

⁴ Table 6 however reveals that this is not so for the helion (${}^3\text{He}$ nucleus) mass. In the 1998 CODATA recommended values, $m_h/m_p^{(1998)}$ was 2.993 152 658 50(93), relative uncertainty of 3.1×10^{-10} , nearly as precise as that for $m_\alpha/m_p^{(1998)}$ of 2.8×10^{-10} . The large increase of the helion mass uncertainty is due to the discovery of an error in the earlier experimental results, as discussed in [50]. In the χ^2 fit, the uncertainty in the helion mass was propagated by making use of the α_{21} coefficients.

Table 8. The a_{32} , a_{12} and b_2 sensitivity coefficients calculated by Korobov [180].

For $\bar{p}^4\text{He}^+$					For $\bar{p}^3\text{He}^+$				
n	ℓ	a_{32}	a_{12}	b_2	n	ℓ	a_{32}	a_{12}	b_2
31	30	2.8170	0.5661	-4.8170	30	29	2.8238	0.7066	-4.8310
32	31	2.5991	0.5223	-4.4072	31	30	2.5985	0.6503	-4.4071
33	31	2.3811	0.4786	-4.0206	33	30	2.1691	0.5429	-3.6539
34	31	2.1793	0.4380	-3.6692	32	31	2.3888	0.5979	-4.0179
33	32	2.3957	0.4815	-4.0298	33	31	2.1776	0.5450	-3.6507
34	32	2.1904	0.4403	-3.6726	34	31	1.9822	0.4962	-3.3161
35	32	1.9994	0.4019	-3.3464	35	31	1.8078	0.4525	-3.0283
36	32	1.8241	0.3667	-3.0616	33	32	2.1923	0.5487	-3.6591
34	33	2.2048	0.4432	-3.6811	34	32	1.9935	0.4990	-3.3206
35	33	2.0112	0.4043	-3.3509	35	32	1.8094	0.4530	-3.0125
36	33	1.8313	0.3682	-3.0494	36	32	1.6402	0.4106	-2.7337
37	33	1.6652	0.3348	-2.7755	37	32	1.4885	0.3727	-2.4898
38	33	1.5224	0.3061	-2.5303	34	33	2.0073	0.5025	-3.3272
35	34	2.0247	0.4070	-3.3577	35	33	1.8201	0.4557	-3.0154
36	34	1.8421	0.3703	-3.0527	36	33	1.6476	0.4125	-2.7327
37	34	1.6732	0.3364	-2.7752	37	33	1.4901	0.3731	-2.4781
38	34	1.5182	0.3053	-2.5242	38	33	1.3477	0.3375	-2.2505
39	34	1.3775	0.2770	-2.2987	35	34	1.8323	0.4587	-3.0194
36	35	1.8543	0.3728	-3.0571	36	34	1.6565	0.4147	-2.7327
37	35	1.6822	0.3382	-2.7759	37	34	1.4957	0.3745	-2.4745
38	35	1.5242	0.3065	-2.5215	38	34	1.3502	0.3381	-2.2435
39	35	1.3806	0.2776	-2.2928	39	34	1.2201	0.3056	-2.0384
40	35	1.2514	0.2517	-2.0886	36	35	1.6664	0.4172	-2.7333
37	36	1.6923	0.3403	-2.7771	37	35	1.5019	0.3761	-2.4709
38	36	1.5308	0.3078	-2.5188	38	35	1.3531	0.3388	-2.2365
39	36	1.3841	0.2783	-2.2868	39	35	1.2201	0.3056	-2.0286
40	36	1.2521	0.2518	-2.0799	40	35	1.1025	0.2762	-1.8456
41	36	1.1346	0.2282	-1.8967	37	36	1.5087	0.3778	-2.4672
38	37	1.5381	0.3093	-2.5161	38	36	1.3560	0.3396	-2.2287
39	37	1.3877	0.2791	-2.2803	39	36	1.2198	0.3055	-2.0177
40	37	1.2525	0.2519	-2.0703	40	36	1.0997	0.2755	-1.8325
41	37	1.1326	0.2278	-1.8848	38	37	1.3589	0.3403	-2.2201
39	38	1.3914	0.2798	-2.2730	39	37	1.2189	0.3053	-2.0054
40	38	1.2526	0.2519	-2.0595	40	37	1.0960	0.2745	-1.8178
41	38	1.1298	0.2273	-1.8715	39	38	1.2171	0.3048	-1.9912
40	39	1.2521	0.2518	-2.0471	40	38	1.0909	0.2733	-1.8007
41	39	1.1260	0.2265	-1.8562	40	39	1.0839	0.2715	-1.7807
41	40	1.1207	0.2254	-1.8383					

unfavored transition $(37, 35) \rightarrow (38, 34)$. The width of each band reflects the experimental error σ_{exp} . Here, $\nu_{\text{th}}(\Delta\eta_{23})$ takes the form

$$\nu_{\text{th}} \left(1 + \alpha_{23} \left(\frac{\Delta\eta_{23}}{\eta_{23}} \right) \right),$$

and for a small fractional change ϵ of $m_{\bar{p}}/m_e$ with respect to the CODATA $m_{\bar{p}}/m_e$ value, $\Delta\eta_{23}/\eta_{23}$ is

$$\frac{\Delta\eta_{23}}{\eta_{23}} = \frac{m_{\bar{p}}/m_e - m_{\bar{p}}/m_e}{m_{\bar{p}}/m_e} = \frac{m_{\text{p}}(1 + \epsilon) - m_{\text{p}}}{m_{\text{p}}} \equiv \epsilon. \quad (50)$$

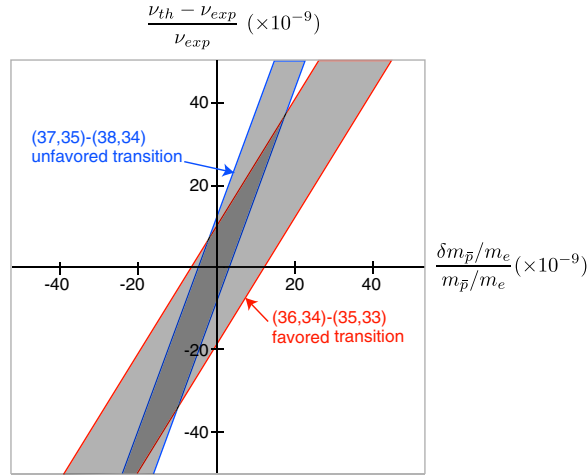


Figure 36. Dependence of the fractional frequency change $\delta\nu/\nu$ on \bar{p} -to-electron mass ratio plotted for one of the $\bar{p}^4\text{He}^+$ favored transitions $(36, 34) \rightarrow (35, 33)$ and an unfavored transition $(37, 35) \rightarrow (38, 34)$.

To obtain the $m_{\bar{p}}/m_e$ value, we minimize the χ^2

$$\chi^2 = \sum \frac{(\nu_{\text{th}}(\Delta\eta_{23}) - \nu_{\text{exp}})^2}{\sigma_{\text{exp}}^2 + \sigma_{\text{th}}^2}. \tag{51}$$

The best-fit values are

	$m_{\bar{p}}/m_e$
$\bar{p}^4\text{He}^+$	1836.152 666(4)
$\bar{p}^3\text{He}^+$	1836.152 697(9)
All	1836.152 674(5)

where we show the results obtained using the $\bar{p}^4\text{He}^+$ data, those with the $\bar{p}^3\text{He}^+$, and the combined result.

4.2. CPT constraints on the \bar{p} mass and charge

Let us now turn to case (2), and examine to what extent we can constrain the mass and charge of the antiproton, if we let both \bar{p} mass and charge to vary with respect to those of the proton.

To this end, we extend equation (47) to include a sensitivity factor β_2^{if} on the \bar{p} charge:

$$\frac{\Delta\nu}{\nu} = \alpha_{23}^{\text{if}} \left(\frac{\Delta\eta_{23}}{\eta_{23}} \right) + \alpha_{21}^{\text{if}} \left(\frac{\Delta\eta_{21}}{\eta_{21}} \right) + \beta_2^{\text{if}} \left(\frac{\Delta z_2}{z_2} \right). \tag{52}$$

Here, the charge sensitivity factor β_2 is obtained by taking a partial derivative of the Hamiltonian (equation (11)) with respect to z_2 (i.e. antiproton charge), and takes the form

$$\beta_2^{\text{if}} = \frac{(2R_\infty c)(b_2^i - b_2^f)}{\nu}, \tag{53}$$

with

$$b_2 \equiv z_2 \left(\frac{\partial E_0}{\partial z_2} \right) = z_2 \left(\left\langle \frac{z_1}{r_{12}} \right\rangle + \left\langle \frac{z_3}{r_{32}} \right\rangle \right), \tag{54}$$

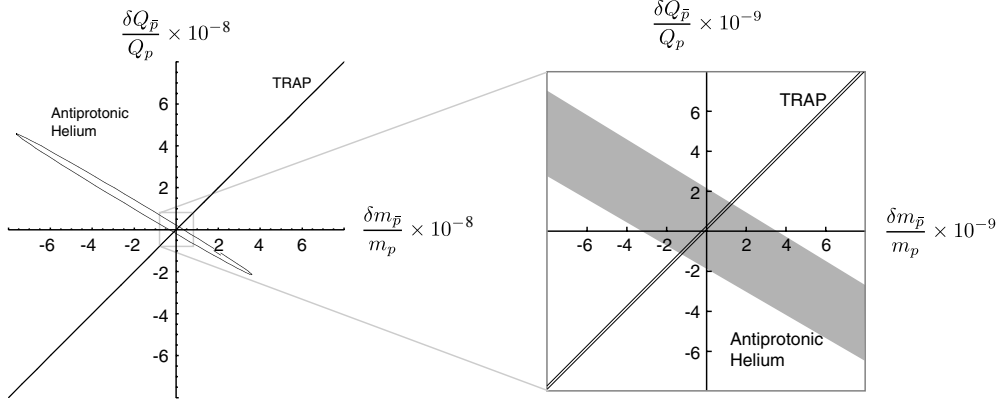


Figure 37. A 90% confidence limit contour on the antiproton mass and charge deduced from the $\bar{p}\text{He}^+$ laser spectroscopy is shown.

where z_1, z_2, z_3 , respectively, are 2, -1 and -1 . The numerical values of β_2^{if} have already been included in table 7.

Naïvely, since the $\bar{p}\text{He}^+$ binding energies (and hence transition frequencies) are roughly proportional to $m_{\bar{p}} Q_{\bar{p}}^2$, we expect see a correlation between the fractional mass change $\delta m_{\bar{p}}/m_p$ versus $\delta Q_{\bar{p}}/Q_p$ such as

$$\delta m_{\bar{p}}/m_p = -2\delta Q_{\bar{p}}/Q_p,$$

as was discussed in [2].

We now calculate the χ^2 value by varying both the antiproton mass and charge according to equation (52). Note that in case (1) when we derived the antiproton-to-electron mass ratio, the second term of equation (52) did not come into play, but since we are now testing the possible deviations of \bar{p} mass and charge with respect to those of the proton, the second term of equation (52) does contribute, since if the \bar{p} mass is different from the p mass, both η_{23} (\bar{p} -to-electron mass ratio) and η_{21} (\bar{p} -to-helium mass ratio) are affected. The 90% confidence level contour in the δm - δQ plane obtained in this way is shown in figure 37.

As was expected, the CPT bounds on charge and mass obtained by the antiprotonic helium atoms are correlated along the $\delta m_{\bar{p}}/m_p \approx -2\delta Q_{\bar{p}}/Q_p$ direction, so that it is not possible to individually constrain $\delta m_{\bar{p}}/m_p$ and $\delta Q_{\bar{p}}/Q_p$. By combining the $\bar{p}\text{He}^+$ results with the proton-to-antiproton cyclotron frequency comparison of the TRAP group [32, 33], a much tighter bound on the equality of antiproton mass and charge with those of the proton of 2×10^{-9} (90% confidence level).

5. The magnetic moment of the antiproton

The term ‘ \bar{p} magnetic moment’ is commonly used for the spin magnetic moment connected to the antiproton spin, $\mu_{\bar{p}}^s = g_s^{\bar{p}} S_{\bar{p}} \mu_N$ with $g_s^{\bar{p}}$ being the spin g -factor of the antiproton. This is known from the spectroscopy of heavy antiprotonic atoms with an accuracy of only 0.3% [5, 67], much worse than the one of the proton. An improvement of this quantity would yield a good test of CPT symmetry. Since antiprotonic helium contains an electron, these magnetic moments lead to a hyperfine structure the measurement of which might allow a more accurate determination of $\mu_{\bar{p}}^s$. The hyperfine structure of $\bar{p}\text{He}^+$, however, is very unique due to the fact that the antiproton in metastable states has a very large orbital angular momentum

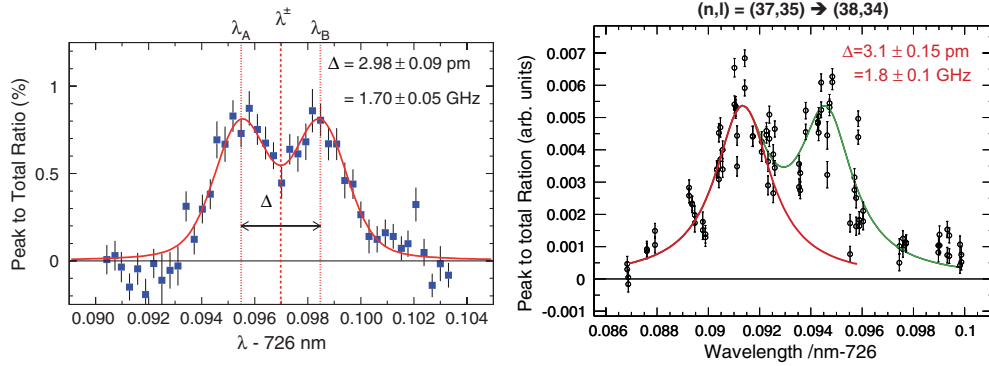


Figure 38. Laser resonance scan of the $(n, L) = (37, 35) \rightarrow (38, 34)$ transitions at 726 nm at LEAR [152] (left) and at the AD [94] (right). In both cases only the HF transitions are resolved.

and a determination of μ_p^s requires the comparison of experimental results with three-body QED calculations. The experiment described in the following has so far not reached a higher precision for μ_p^s than the Particle Data Group (PDG) value, although the individual transitions have been measured with a precision of about 30 ppm. An improved experiment is therefore being prepared at the AD which will be described in section 6.

5.1. HF structure in laser transitions

The hyperfine structure of $\bar{p}^4\text{He}^+$ was first experimentally observed in a laser spectroscopy experiment at LEAR in the transition $(n, L) = (37, 35) \rightarrow (38, 34)$ at 726 nm [152] (cf figure 38(left)). The calculations of BK [97] showed, that the difference of HF splittings is rather small in favored laser transitions along $\Delta v = 0$ cascades, but significantly larger in unfavored $\Delta v = 2$ transitions as the 726 nm one. A laser transition between two levels is shown in figure 39. Due to the large band width of the laser used in 1996 (~ 1.2 GHz), only transitions between the HF doublets could be resolved leading to the doublet structure in figure 38(left). The observed splitting of $\Delta\nu_{\text{HF}} = (1.75 \pm 0.05)$ GHz corresponding to the difference in HF splitting of the (37,35) and (38,34) states was in good agreement with the value of BK of 1.77 GHz, but the achievable precision in a laser scan is limited to a few per cent due to the large laser band width of the pulsed dye lasers used. Also with the new pulsed laser system used in the beginning at the AD (cf. section 3.3), the situation did not improve much (cf figure 38(right)) although the laser bandwidth was reduced to ~ 0.6 GHz.

5.2. Laser-microwave-laser resonance method

In order to measure the HF splitting of the (37,35) state more precisely, we devised a laser-microwave-laser resonance method [181] to directly measure the allowed M1 transitions ν_{HF}^+ and ν_{HF}^- (cf figure 39) within a HF quadruplet using ~ 13 GHz microwave radiation. In order to detect a microwave-induced transition between the F^+ and F^- doublets, first a population asymmetry between them has to be created. This is done by a first laser pulse at time t_1 tuned to one line of the HF doublets, i.e. f_+ (cf figure 40) which predominantly depopulates the F^+ doublet (note that due to the large laser band width compared with the HF splitting, the F^- state is also partially affected). A microwave pulse resonant to ν_{HF}^- or ν_{HF}^+ will move part of the population of the F^- doublet to F^+ . A second laser pulse of frequency f_+ at time t_2 then

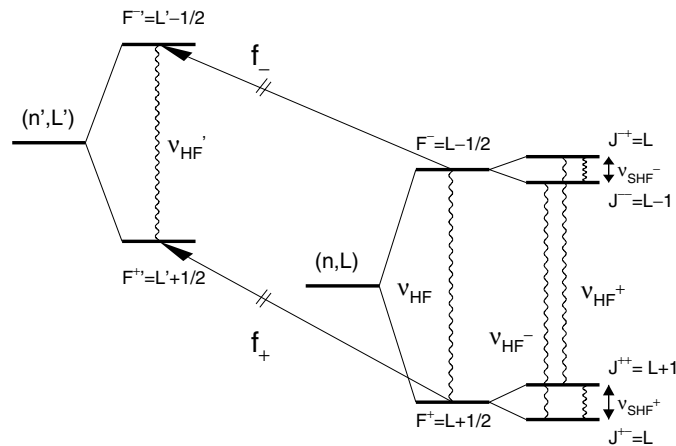


Figure 39. Laser transition between two quadruplet HF states.

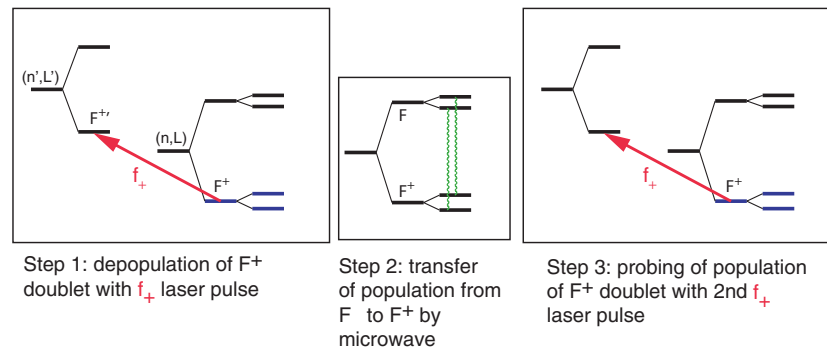


Figure 40. Explanation of the laser-microwave-laser method.

measures the population of the F^+ doublet. A scan is performed by keeping the laser frequency constant and scanning the microwave frequency.

A numerical solution of the optical Bloch equations describing the laser and microwave transition process was performed to estimate the expected signal [182]. Figure 41(left) shows the populations of the four SHF states as a function of time during the experiment. The grey shaded areas below denote the population of the short-lived daughter states in the laser transition, which corresponds to the annihilation signal we observe in the ADATS spectra. Figure 41(right) shows an experimental ADATS with the two peaks. As the simulation indicates, the difference of the microwave on and off cases leads to a rather small change in intensity of the spikes of order 10%. Since this is comparable to typical fluctuations of the antiproton intensity from one AD shot to another, a large number of shots has to be averaged in order to achieve the needed sensitivity.

5.3. Experiment

The necessary apparatus to perform the microwave-laser-microwave experiment is complex and requires to stop antiprotons in a cavity filled with helium gas at cryogenic temperatures. We used the same cryostat as for the initial laser spectroscopy experiments using the AD beam

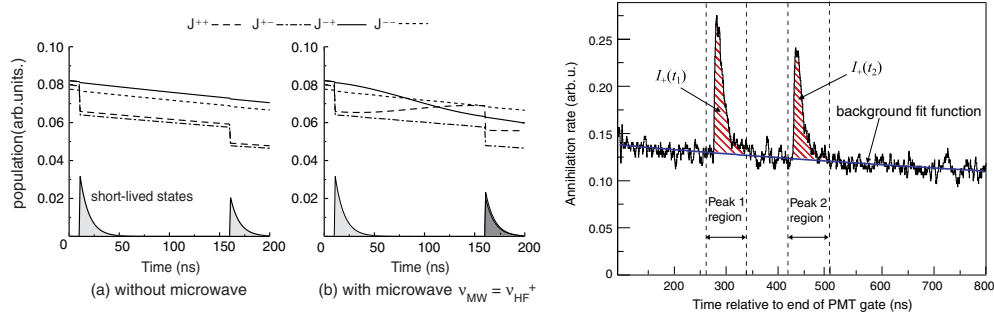


Figure 41. Left: (a) Simulated diagrams of the populations of each SHFS state and those of the short-lived daughter states of the laser transition, for the microwave-off case. (b) Simulated diagrams of the populations, with microwave field of $\nu_{\text{MW}} = \nu_{\text{HF}}^+$. The dark-gray area in the $t = t_2$ peak of short-lived population corresponds to that of case (a), and the states in case (b) have a little more population due to the microwave-induced transition [183]. Right: part of ADATS spectrum showing the two spikes caused by the laser pulses at times t_1 and t_2 . The intensities $I_+(t_1)$ and $I_+(t_2)$ are proportional to the population of the (37,35) state at the corresponding time. The figure also shows the fit background curve and the fit range used in the analysis to extract the peak intensities [181].

(cf section 3) and added a cylindrical microwave cavity which had both faces made of meshes to allow both the laser beam and the antiprotons to enter.

The cavity was connected to a rectangular wave guide and immersed into the cryogenic helium gas target ($T \sim 6.1$ K). Outside the cryostat, the waveguide was connected to a triple stub tuner that was used to adjust the resonance frequency without needing movable parts at low temperatures [184]. The microwave radiation was generated by a network analyzer and amplified by a traveling wave tube amplifier before being introduced into the wave guide. The annihilation signal of the antiprotons was recorded as usual using two Čerenkov counters read out by a digital oscilloscope.

The laser radiation at 726.1 nm was created by one pulsed dye laser. In order to obtain two consecutive pulses, the laser beam was split in a 50% beam splitter, and one pulse was delayed using multiple reflexions between mirrors located about 12 m apart (cf figure 42). This limited the delay time to $\Delta t \approx 160$ ns so as not to degrade the transverse beam profile too much. The two laser beams were merged and focused into the helium target through a quartz window.

5.4. Results

An experiment was performed in 2001 at the AD. The microwave power was set to the optimum value (15 W) corresponding to an oscillating field strength of $B_1 = 7$ G inside the cavity as obtained from computer simulations. In order to reduce systematic effects such as fluctuations in the overlap of laser and \bar{p} beams or the \bar{p} intensity, which might affect both peaks identically, we calculated the ratio $R^{++} \equiv I_+(t_2)/I_+(t_1)$ (cf figure 41) and plotted it against the microwave frequency ν_{MW} .

We performed several microwave scans at two different densities of the helium medium. The off-resonance level varied from data set to data set due to uncontrollable systematic effects associated mainly with laser misalignments. To compensate this, the data sets were normalized to their individual ‘microwave-off’ value R_{off}^{++} obtained from points with very low microwave power included in all scans. Each data set was then fitted by a sum of two Lorentzian functions with identical width and amplitude, plus a constant background. The results for ν_{HF}^+ and ν_{HF}^-

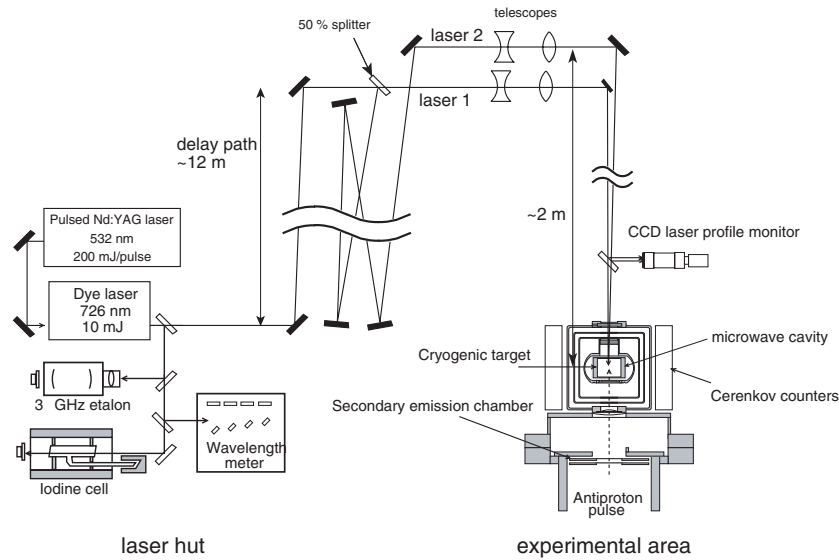


Figure 42. Experimental setup (top view) of the laser system and the laser beam path to the helium target.

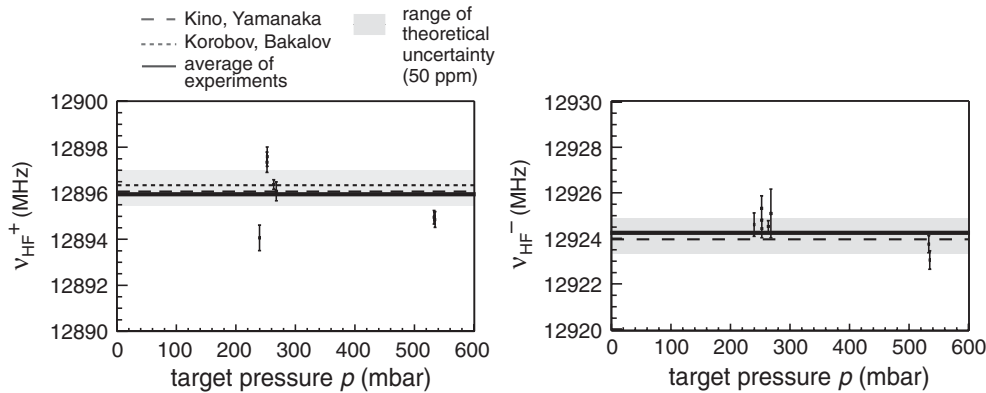


Figure 43. Fit results for the two central frequencies ν_{HF}^+ and ν_{HF}^- of the two peaks in the individual microwave scans as a function of density [184]. Shown are also the theoretical predictions and the averaged value with its error (solid line and grey areas).

as well as the width of the Lorentzians agreed within the error bars and did not show any dependence on the target density (cf figure 43). This is consistent with theoretical arguments presented by Korenman [185, 186] and Bakalov [187] that the shift of the line centers with density is very small, and that the collisional broadening at our densities is at maximum of the order of MHz [185, 186] or as small as 10 kHz [187].

We therefore combined all data sets and averaged points within 0.7 MHz to give the final spectrum shown in figure 44. The measured line width $\gamma_{\text{exp}} = 5.3 \pm 0.7$ MHz is close to the expected width given from the Fourier limit of the 160 ns observation time window, $\gamma_{\text{obs}} \approx 1/160 \text{ ns} = 6.25$ MHz. The natural width of the (37, 35) state of $\gamma_{(37,35)} = 0.12$ MHz is much smaller, and other contributions coming either from collisions, the inhomogeneity of

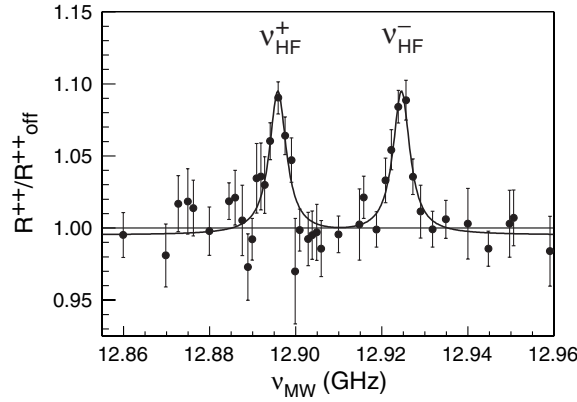


Figure 44. Average of all microwave scans showing clearly two resonance lines as predicted. The width of the lines of ~ 6 MHz corresponds to 5×10^{-4} of the central frequency [181].

Table 9. Experimental values for the HF transition frequencies of the state (37, 35) in GHz compared with theoretical results. The relative experimental error δ_{exp} and the difference $\Delta_{\text{th-exp}} \equiv (\nu_{\text{th}} - \nu_{\text{exp}})/\nu_{\text{exp}}$ are given in ppm.

	ν_{HF}^+ (GHz)	δ_{exp} (ppm)	ν_{HF}^- (GHz)	δ_{exp} (ppm)
Exp.	12.895 96(34)	27	12.924 67(29)	23
		$\Delta_{\text{th-exp}}$		$\Delta_{\text{th-exp}}$
BK [97]	12.895 97	0.6	12.923 94	-57
KB [188]	12.896 346 2	30	12.924 2428	-33
YK [153]	12.898 977	234	12.926 884	171
K [96]	12.896 073 91	8.6	12.923 963 79	-55

the magnetic field over the stopping distribution of \bar{p} , or the fact that the many substates with magnetic quantum numbers $m = -J \dots J$ each have different Rabi frequencies seem not to contribute significantly to the observed width.

The final results for ν_{HF}^+ and ν_{HF}^- obtained from fitting two Lorentzians plus a constant background to the spectrum of figure 44 are presented in table 9 and compared with theoretical calculations by two groups. The theoretical values for ν_{HF}^+ and ν_{HF}^- distribute over a much wider range (~ 100 ppm) than the laser transition energies (~ 0.1 ppm) calculated by the same groups (see comparison in [94]), reflecting a higher sensitivity of the hyperfine coupling terms to the details of the wave functions involved. Nevertheless, the experimental values are in excellent agreement with the results of Korobov and Bakalov (both their initial values BK [97] and their most recent ones KB [188]) as well as the latest values of Kino *et al* (K [96]).

The agreement of the experimental values ν_{HF}^+ and ν_{HF}^- with the most updated theoretical values KB and K is about 6×10^{-5} or better, on the level of the accuracy of the calculations. These do not include contributions of relative order $\alpha^2 \approx 10^{-4}$ or higher. Presently, the experimental error is about 3×10^{-5} , slightly exceeding the theoretical precision. The excellent agreement between experiment and theory proves the validity of the theoretical expressions of Bakalov and Korobov for the HFS of $\bar{p}\text{He}^+$. The microwave resonance frequencies, ν_{HF}^+ and ν_{HF}^- , themselves are primarily depending on the dominant \bar{p} orbital magnetic moment $g_{\ell}^{\bar{p}} \mathbf{L}_{\bar{p}} \mu_N$. Thus, the agreement between theory and experiment can be interpreted as an experimental

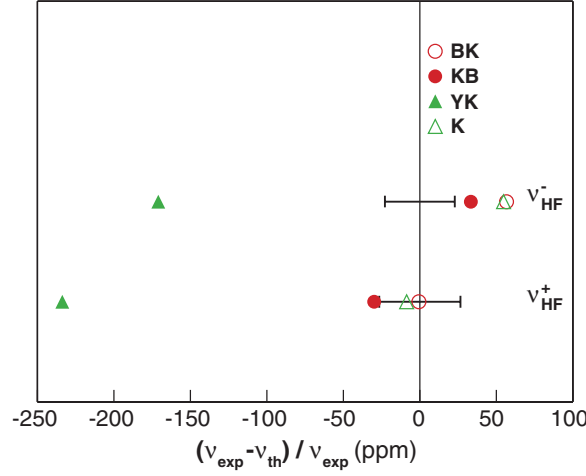


Figure 45. Experimental result (error bars) and relative difference to several theoretical calculations.

proof of $g_{\ell}^{\bar{p}} = 1$ with a relative precision of $\sim 6 \times 10^{-5}$. We note that no experimental value exists for $g_{\ell}^{\bar{p}}$ for the proton because no atoms with an orbiting proton exist in the world of ordinary matter (figure 45).

Because the SHF splittings (which are caused by the spin magnetic moment $\mu_{\bar{p}}^s$ of the antiproton) in the F^+ and F^- doublets are different, the observed microwave frequencies also exhibit a dependence on $\mu_{\bar{p}}^s$. The sensitivity depends strongly on the details of the individual levels and has been evaluated by Bakalov and Widmann [189, 190]. They calculated sensitivity factors $S_{nLFJ} = \partial v_{nLFJ} / \partial \mu$, where v_{nLFJ} is the frequency difference of a SHF substate to the spin-averaged center value. The sensitivities of the observed transitions on $\mu_{\bar{p}}^s$ are then given by the difference of the sensitivities of parent and daughter states.

The error $\Delta\mu$ in the \bar{p} spin magnetic moment can then be obtained from

$$\Delta v = \frac{\partial v_{nLFJ}}{\partial \mu} \Delta\mu \rightarrow \Delta\mu[\mu_N] = \frac{\Delta v(\text{GHz})}{S[\text{GHz}/\mu_N]}, \quad (55)$$

where the values in square brackets denote the units of the different quantities.

For a determination of $\mu_{\bar{p}}^s$ it is necessary that the theoretical uncertainty of the calculated transition frequency is at least as small as the experimental one. For the measured transitions ν_{HF}^+ and ν_{HF}^- which are primarily sensitive to the \bar{p} orbital magnetic moment this turns out not to be the case. The only quantity experimentally accessible by the current method is the difference $\Delta\nu_{\text{HF}} = \nu_{\text{HF}}^- - \nu_{\text{HF}}^+ = \nu_{\text{SHF}}^+ - \nu_{\text{SHF}}^-$ which is directly sensitive to $\mu_{\bar{p}}^s$. Because it is defined and measured as a difference, both the theoretical uncertainty is an order of magnitude worse than for ν_{HF}^+ and ν_{HF}^- , and the experimental error is large: $\Delta\nu_{\text{HF}}^{(37,35)} = (27.97 \pm 0.45)$ MHz corresponding to an error of 1.6%. Together with the sensitivity factor $S = 10.1$ MHz/ μ_N from [190] this results in an absolute error of $\mu_{\bar{p}}^s$ of $0.045 \mu_N$ or a relative error of also 1.6%. This is consistent with an earlier determination of $\mu_{\bar{p}}^s = 2.800 \pm 0.008 \mu_N$ (relative error 0.3%) from a fine structure measurement of antiprotonic lead [67].

Possible improvements of the experiment in order to increase the accuracy of the spin magnetic moment of the antiproton will be described in the following section.

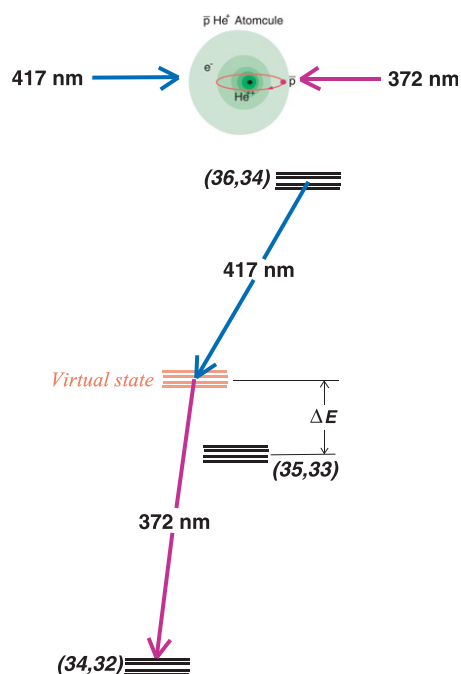


Figure 46. Portion of the energy level diagram of $\bar{p}^4\text{He}^+$, indicating the principle of sub-Doppler two-photon spectroscopy.

6. Future prospects

6.1. Doppler-free two-photon laser spectroscopy of antiprotonic helium

The precision of the laser spectroscopy experiments to determine the optical transition frequencies ν_{exp} of $\bar{p}^4\text{He}^+$ is limited by the thermal Doppler broadening of several hundred MHz (equation (37)) in the observed lines (figure 34). Further improvements in the experimental precision of ν_{exp} requires that this broadening be reduced or eliminated. Laser spectroscopy of normal atoms at the highest precision utilize two laser beams arranged in a counterpropagating geometry, to effectively eliminate the Doppler broadening to first order (see section 1). For example, the frequency of the 1s–2s two-photon transition in atomic hydrogen has been measured to precisions of $\sim 10^{-14}$, by irradiating the atoms with two counterpropagating laser beams of the same wavelength $\lambda = 243$ nm equal to half the 1s–2s interval [170]. It is not possible, however, to directly apply this Doppler-canceling technique to our $\bar{p}^4\text{He}^+$ experiments, because the transition probabilities involved in any non-linear two-photon transition of the antiproton is many orders of magnitude smaller than, e.g. the electron case in hydrogen. Indeed, calculations reveal that the laser intensities that would be needed to excite such a $\bar{p}^4\text{He}^+$ transition within the microsecond-scale lifetime of the atom, using two photons of equal wavelength are much greater than those available from any tunable laser.

We intend to solve these problems by utilizing a near-resonant two-photon excitation (figure 46). The two counterpropagating laser beams irradiating the $\bar{p}^4\text{He}^+$ can have non-equal frequencies ν_1 and ν_2 , adjusted such that (i) their combined frequencies $\nu_1 + \nu_2$ is tuned to the two-photon transition $(n, \ell) = (36, 34) \rightarrow (34, 32)$ involving an angular momentum change of $\Delta\ell = 2$, (ii) the virtual intermediate state involved in the two-photon transition is tuned to

within a few GHz of a real state $(n, \ell) = (35, 33)$. The nearness of the virtual state to a real one should lead to an enhancement of the two-photon transition probability by several orders of magnitude compared with the case $\nu_1 = \nu_2$; theoretical calculations indicate that laser energy densities of $\sim 1 \text{ mJ cm}^{-2}$ would then be needed to efficiently drive the two-photon transition. Under these conditions, the observed width $\Delta\nu_{2\gamma}$ of the resonance line will decrease by factor 20 compared with the thermal Doppler width $\Delta\nu_D$ according to the equation,

$$\Delta\nu_{2\gamma} = \left| \frac{\nu_1 - \nu_2}{\nu_1 + \nu_2} \right| \Delta\nu_D. \quad (56)$$

The ASACUSA collaboration is currently developing the two high-power pulsed lasers and experimental target needed to carry out this experiment. These solid-state lasers are expected to have a much smaller frequency chirp and higher spectral resolution compared with the dye ones used previously. Systematic studies will be made of ac Stark effects, which can reach $\sim 1 \text{ MHz}$ at the high laser powers used here. The experimental precision on the $\bar{p}\text{He}^+$ transition frequencies that can be finally achieved by this method would likely be limited to a few MHz by the residual first-order Doppler width, and the systematic error arising from the frequency chirp.

6.2. Microwave spectroscopy of antiprotonic helium

6.2.1. Improved experimental setup. The hyperfine structure of antiprotonic helium is due to the interaction of the antiproton spin with its angular momentum and electron spin. As described in section 5, the current result of the laser-microwave-laser experiment of the $(37, 35)$ state of antiprotonic helium yields a determination of the \bar{p} magnetic moment $\mu_{\bar{p}}^s$ with an error of 1.6%. This accuracy is about a factor 5 worse than the current PDG value which has an error of 0.3% [5].

The previous experiment was limited by two factors which are both related to the pulsed dye lasers used up to 2003 in ASACUSA:

- (i) the maximum time difference $\Delta t = 160 \text{ ns}$ between the two laser pulses leads to a line broadening by the Fourier limit of $\Delta\nu = 1/\Delta t \approx 6 \text{ MHz}$. This time difference is limited by the fact that we need to use one dye laser, split the output and delay one laser beam for $\sim 20 \text{ m}$ in order to avoid uncorrelated frequency fluctuations if we used two dye lasers.
- (ii) The large band width of the pulsed dye lasers leads to an overlap of the HF lines, so if the laser is set to one HF line, it still partly depopulates the other HF state. This causes a reduction of the signal to noise in our measurement.

These limitations can be overcome by using the newly developed pulse-amplified laser system developed for the 2004 measurements. Using a setup as sketched in figure 47, two laser pulses of arbitrary time delay but correlated frequency can be obtained. In addition, the band width of the new laser system ($\sim 100 \text{ MHz}$) is much less as compared with the HF splitting in the laser transition used ($\sim 1.8 \text{ GHz}$), so that the two HF lines will be completely separated. Thus, an experiment using the same method but replacing the laser system should yield a microwave scan with much smaller line width and much higher signal-to-noise ratio. Numerical simulations and first tests show that an improvement of the experimental accuracy of one order of magnitude is feasible, thus a measurement of $\mu_{\bar{p}}^s$ with an accuracy of 0.1%, a factor 3 better than the current PDG value, seems reachable.

6.2.2. Sensitivity of transitions to $\mu_{\bar{p}}^s$ and possible improvements. In order to determine the magnetic moment of the antiproton from microwave spectroscopy of $\bar{p}\text{He}^+$, the comparison

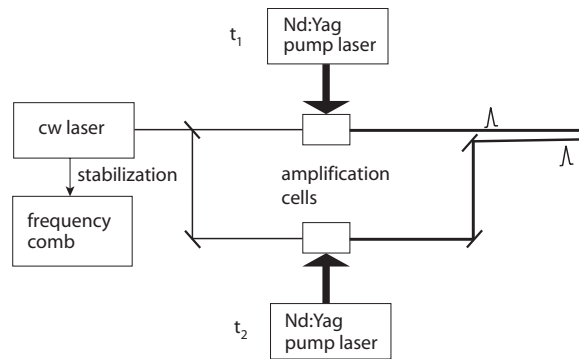


Figure 47. Schematic setup of the lasers for an improved laser-microwave-laser experiment using two independently triggered pulse-amplification stages seeded by the same cw laser.

Table 10. Theoretical (Δ_q) and experimental (δ_{exp}) errors, sensitivity to the antiproton magnetic moment (δ_μ), and maximum improvement factors Δ_q/Δ_μ of the measurement of $\Delta\nu_{\text{HF}}$ for various states (n, L) of antiprotonic helium.

(n, L)	(35,33)	(37,34)	(39,35)	(33,32)	(36,34)	(37,35)	(35,34)	(34,33)	(38,35)
$\Delta_q \times 10^4$	6	11	3	8	23	12	6	4	5
δ_μ (kHz)	180	90	270	510	50	90	210	360	190
Δ_q/Δ_μ	5.0	2.7	8.9	3.6	1.3	2.7	5.4	8.4	6.0
δ_{exp} (kHz)	36	33	30	142	38	33	39	43	32

of measured transition frequencies with three-body QED calculations is necessary. A recent paper by Bakalov and Widmann (BW) [190] investigated this issue more closely. For the calculations, the limiting factor comes from the Breit approximation used, which neglects contributions to the HFS Hamiltonian of relative order $\alpha^2 \sim 10^{-4}$. Since the observable transitions ν_{HF}^+ and ν_{HF}^- only indirectly depend on $\mu_{\bar{p}}^s$ (cf section 5), the theoretical accuracy is not good enough to obtain sensitivity to the \bar{p} magnetic moment. Most sensitive are the SHF transitions ν_{SHF}^+ and ν_{SHF}^- , but they are very difficult to measure due to the much smaller transition matrix element which would require excessively high radio-frequency power in a frequency region (100–300 MHz) where the use of high- Q cavities is not possible.

Without a further theoretical improvement (going beyond the Breit approximation, which appears extremely difficult), the only measurable quantity with sensitivity to $\mu_{\bar{p}}^s$ is the *difference* of HF transitions $\Delta\nu_{\text{HF}} = \nu_{\text{HF}}^- - \nu_{\text{HF}}^+ = \nu_{\text{SHF}}^+ - \nu_{\text{SHF}}^-$. Since it is a difference, both the experimental and theoretical errors are larger. A summary of the theoretical situation for various states (n, L) of $\bar{p}\text{He}^+$ is given in table 10. Here, Δ_q stands for the estimated relative accuracy of the QED calculations, which is significantly larger than 10^{-4} . The row δ_μ indicates the absolute accuracy to which $\Delta\nu_{\text{HF}}$ needs to be measured for a given state to achieve the current accuracy of the antiproton magnetic moment. As a consequence, the ratio Δ_q/Δ_μ defines the maximum improvement factor to the current known precision of the antiproton magnetic moment. δ_{exp} is the corresponding absolute experimental precision required to reach the limit of the accuracy of the theory.

Thus measuring the hyperfine structure of the (37,35) state to a resolution of 30 kHz will result in a factor of 3 improvement to the known antiproton spin magnetic moment. 30 kHz corresponds to a factor 10 improvement of our current precision which is—as described above—feasible with the new laser system. Furthermore, other states offer a higher

improvement factor up to 9 while the absolute experimental precision is always around 30 kHz. This comes from the fact that for these states, the splitting $\Delta\nu_{\text{HF}}$ is larger. Thus, measuring, e.g. the HFS of the (39, 35) state with the same experimental accuracy, the value of $\mu_{\bar{p}}^s$ can ultimately be improved by about one order of magnitude with the existing theoretical calculations. In addition to testing *CPT*, this will constitute a severe test of the validity of three-body QED calculations. If these calculations are some day improved beyond the Breit approximation, higher precision will become possible.

6.3. Two-body antiprotonic helium ions

One of the interesting by-products of these RFQD studies was the synthesis [162] of cold ($T \sim 10$ K), long-lived antiprotonic helium ions ($\bar{p}\text{He}^{2+}$) [191, 192]. This is a singly charged, two-body system composed of an antiproton and a helium nucleus, and its spectroscopic properties can therefore be calculated analytically. In future experiments, the ASACUSA collaboration hopes to measure the transition frequencies of this ion by laser spectroscopy.

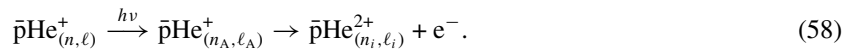
Recent experiments produced the Rydberg forms of the $\bar{p}^4\text{He}^{2+}$ and $\bar{p}^3\text{He}^{2+}$ isotopes, wherein the antiproton occupies circular states with large principal and orbital angular momentum quantum numbers $n_i = 28\text{--}32$ and $\ell_i = n_i - 1$. As in the case of the three-body $\bar{p}\text{He}^+$ atom, the probability density of these antiprotonic orbitals have very little overlap with the helium nucleus. A single isolated ion (i.e. an ion that does not suffer collisions with surrounding atoms) thus has lifetimes near $n_i = 30$ and $\ell \sim n - 1$ of a few hundred nanoseconds against annihilation. The antiproton undergoes a series of radiative transitions [193] of the type $\Delta n_i = \Delta \ell_i = -1$, and is finally absorbed from the $n \leq 3$ or $\ell \leq 2$ regions [194].

In addition to the above analytic nature of $\bar{p}\text{He}^{2+}$, QED and relativistic effects cause only negligible shifts (of order $\leq 10^{-8}$) in its energy levels, on account of the large mass and small magnetic moment of the antiproton. These Rydberg ions thus constitute ideal semiclassical Bohr systems whose spin-independent parts of the energy levels (left side of figure 13) can be theoretically calculated to very high precision ($\sim 10^{-8}$) using the simple equation [193],

$$E_n = -\frac{4R_\infty hc}{n_i^2} \frac{M}{m_e} \frac{Q_{\bar{p}}^2}{e^2}, \quad (57)$$

where the reduced mass of the system is denoted by M , the electron mass by m_e , the Rydberg constant by R_∞ and the antiproton and electron charges by $Q_{\bar{p}}$ and e . The simplicity of the system, when coupled with the long (100 ns scale) lifetimes necessary for laser spectroscopy, in principal makes this ion a good candidate for determining the properties of antiprotons (e.g. its mass and charge) at the highest precision.

In these experiments [162], cold ions which selectively populated states (n_i, ℓ_i) were produced by a two-step method of (i) first cooling a three-body $\bar{p}\text{He}^+$ atom occupying a high- (n, ℓ) state by atomic collisions, (ii) removing the electron of $\bar{p}\text{He}^+$ by inducing a laser transition to an Auger-dominated state (n_A, ℓ_A) . Auger emission will then produce the nearest ionic state (n_i, ℓ_i) :



As described above, the Auger decay lifetime $\tau_{(n_A,\ell_A)}^A$ was visible as the tail of the sharp peak (figure 48) in the delayed annihilation time spectrum that appeared when the laser induced a transition to state (n_A, ℓ_A) . Normally, collisions once again immediately destroy any ion produced subsequently by Auger process, in which case the length of the tail measures $\tau_{(n_A,\ell_A)}$ directly (folded with the timing resolution of the laser pulse). We expected, however, that as the target density (i.e. collision rate) was reduced to extremely low values, the $\bar{p}\text{He}^{2+}$ ion's

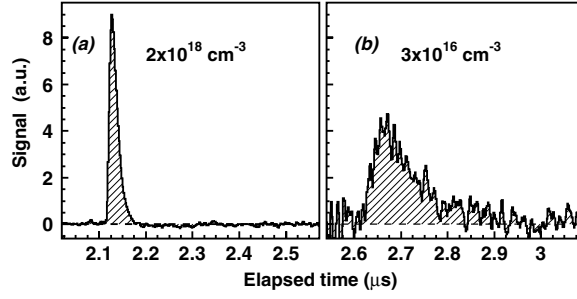


Figure 48. Annihilation spike produced by inducing the $\bar{p}^4\text{He}^+$ transition $(n, \ell) = (39, 35) \rightarrow (38, 34)$, measured at a high target density (a). The tail extended at ultra-low densities (b), indicating the formation of long-lived $\bar{p}^4\text{He}^{2+}$ ions populating state $(n_i, \ell_i) = (32, 31)$ [162].

own lifetime would begin to compete with the Auger lifetime of its parent $\bar{p}\text{He}^+$ state. This would be seen as a lengthening of the tail, and should therefore be an unambiguous signature of the production of cold, long-lived ions.

The time spectra of figure 48 measured using the RFQD confirm the reasoning outlined above concerning the tails of spikes in the annihilation distributions. Figure 48(a) was measured at the high density $\rho = 2 \times 10^{18} \text{ cm}^{-3}$ by inducing the $\bar{p}^4\text{He}^+$ transition at $\lambda = 597.3 \text{ nm}$ from state $(n, \ell) = (39, 35)$ with lifetime $\tau_{(39,35)} \sim 1.4 \mu\text{s}$, to state $(38, 34)$ with a short Auger lifetime $\tau_{(38,34)}^A \sim 9 \text{ ns}$ [127]. Auger emission (curved arrow in figure 13) then produced the $\bar{p}\text{He}^{2+}$ ionic state $(n_i, \ell_i) = (32, 31)$. The annihilation spike decayed with lifetime $\tau_{\text{obs}} \sim (9 \pm 1) \text{ ns}$, which indicates that the ion was destroyed by collisions in a short time relative to the $\bar{p}\text{He}^+$ Auger lifetime $\tau_{(38,34)}^A \sim 9 \text{ ns}$. When the same transition was measured at a 100 times lower density $\rho = 3 \times 10^{16} \text{ cm}^{-3}$, however, the lifetime increased by an order of magnitude to $\tau_{\text{obs}} \sim (90 \pm 20) \text{ ns}$ (figure 48(b)), due to the prolonged collisional lifetime τ_i of the ion initially occupying $(n_i, \ell_i) = (32, 31)$. This spectrum, representing data accumulated from $\sim 10^{10}$ antiprotons stopped in the target, includes $\sim 10^6$ such ions. The $\bar{p}\text{He}^{2+}$ ions produced subsequently have roughly the same temperature $T \sim 10 \text{ K}$ as the parent $\bar{p}\text{He}^+$ atom. This is because the kinetic energy of the emitted Auger electron ($E_{(38,34)}^A = 0.8 \text{ eV}$, corresponding to the energy difference between the Auger-dominated $\bar{p}\text{He}^+$ - and final $\bar{p}\text{He}^{2+}$ -states, see figure 13) is very low. This results in a $\sim 100 \mu\text{eV}$ recoil energy for the ion.

Now according to equation (57), the $E1$ transitions $(n, \ell) \rightarrow (n+1, \ell+1)$ between circular $\bar{p}\text{He}^{2+}$ ionic states with n - and ℓ -values of 29–33 are characterized by UV transition wavelengths $\lambda = 200\text{--}310 \text{ nm}$, and dipole moments $D \sim 0.1 \text{ Debye}$. Hence these ionic transitions are readily induced by pulsed UV laser beams with intensities similar to those used in the $\bar{p}\text{He}^+$ atom experiments. The difficulty in any laser spectroscopy experiment of $\bar{p}\text{He}^{2+}$, however, lies in the detection of these laser transitions. The ASACUSA collaboration is examining the possibilities of carrying out these laser spectroscopy experiments in the future.

7. Summary

Antiprotonic helium atoms ($\bar{p}\text{He}^+ \equiv e^- - \bar{p} - \text{He}^{++}$), serendipitously discovered at KEK (1991) and subsequently studied (1992–1996) at CERN's low energy antiproton ring (LEAR), have been further studied (1999–2007) using high-precision laser-spectroscopic methods at CERN's Antiproton Decelerator facility (AD). Experimental methods were successively developed to measure the laser transition frequencies between (n, ℓ) and $(n \pm 1, \ell - 1)$ states of $\bar{p}\text{He}^+$

($n \sim 40$ and $\ell \lesssim n - 1$ are the principal and orbital quantum numbers of the antiproton) to progressively higher precisions, from the initial LEAR value of 3 parts in 10^6 , to the most recent value of 9 parts in 10^9 .

The first major advance was brought about by using of pulsed beams of antiprotons in high precision measurements of the $\bar{p}\text{He}^+$ transition frequencies at high precision. Under this new experiment mode, a single laser pulse of high spectral purity induce transitions in $\sim 10^3$ – 10^4 $\bar{p}\text{He}^+$ atoms simultaneously. This allowed large numbers of $\bar{p}\text{He}^+$ to be produced and studied at a higher rate and precision than was possible using continuous antiproton beams. The next advance was introduced by the construction of the radio-frequency quadrupole decelerator (RFQD), a post-decelerator to the AD, which can decelerate antiprotons from 5.3 MeV to ~ 100 keV with an efficiency of $\sim 20\%$. The RFQD made it possible to stop antiprotons in a helium gas target at very low densities of $\rho \sim 10^{17} \text{ cm}^{-3}$, some 10^4 times lower than those previously used, and to study $\bar{p}\text{He}^+$ atoms under near-vacuum conditions. This eliminated the need for the zero-density extrapolation, a large source of errors in previous measurements, thereby improving the experimental precision by nearly an order of magnitude. Another order of magnitude improvement was recently achieved by using a femtosecond optical frequency comb and continuous-wave pulse-amplified laser. The new laser system made it possible to reduce systematic uncertainties in absolute frequency determination to a few MHz level, better than the statistical uncertainties of 3–13 MHz.

This progress in experimental technique was matched by similar advances in the theoretical methods employed in high-precision three-body QED calculations. Methods have been developed to obtain complex eigenvalues of the three-body Hamiltonian to 1 MHz scale precisions, and QED corrections have been applied up to the order of α^5 .

Comparisons of experimental ν_{exp} and theoretical ν_{th} frequencies for twelve transitions, seven in $\bar{p}^4\text{He}^+$ and five in $\bar{p}^3\text{He}^+$, yielded an antiproton-to-electron mass ratio of $m_{\bar{p}}/m_e = 1836.152\,674(5)$, which agrees with the known proton-to-electron mass ratio at the level of $\sim 2 \times 10^{-9}$. The experiment also set a limit on any *CPT*-violating difference between the antiproton and proton charges and masses, $(Q_{\bar{p}} - |Q_{\bar{p}}|)/Q_p \sim (m_p - m_{\bar{p}})/m_p < 2 \times 10^{-9}$ to a 90% confidence level. If on the other hand we assume the validity of *CPT* invariance, the $m_{\bar{p}}/m_e$ result can be taken to be equal to m_p/m_e . The present result has in fact contributed to the improvement of the relative standard uncertainty in the proton–electron mass ratio from 0.46 ppb (2002 CODATA values) [50] to 0.43 ppb (2006 CODATA values) [195].

Further improvements in the experimental precision would be possible if the thermal Doppler broadening could be reduced. With a near-resonant two-photon excitation method, currently being developed, it appears possible to determine the antiproton-to-electron mass ratio with a precision comparable to that of the proton-to-electron mass ratio ($\sim 0.5 \times 10^{-9}$). Achieving much higher precisions of $< 10^{-10}$ however would be difficult unless a new higher-quality low-energy antiproton beam becomes available and a spectroscopic method based on cw lasers can be developed.

Each (n, ℓ) level of $\bar{p}^4\text{He}^+$ in fact has a quadruplet hyperfine structure, due to the coupling of the antiproton orbital angular momentum, the antiproton spin and the electron spin. At the AD, the hyperfine splittings of one $\bar{p}^4\text{He}^+$ level were measured by a laser-microwave-laser technique with a precision of some 30 ppm. By comparing the measured frequencies with the results of three-body QED calculations, the antiproton spin magnetic moment was deduced to a fractional precision of 1.6%. Although this method has so far not reached a higher precision for $\mu_{\bar{p}}$ than the PDG value of 0.3%, a new series of experiments under preparation is likely to achieve a precision better than 0.1%, thereby setting a new limit on the possible difference between the proton and antiproton magnetic moments. This is an independent *CPT* test.

Acknowledgments

We thank D Bakalov, Y Kino and V I Korobov for theoretical discussions, and the members of the ASACUSA spectroscopy group, especially T Yamazaki, J Eades, D Barna, A Dax, B Juhász, W Pirkel and H A Torii for many years of fruitful collaboration. We are deeply indebted to the CERN AB division for their great efforts in constructing and operating the Antiproton Decelerator and radiofrequency quadrupole decelerator facilities. This work was supported by Monbukagakusho (grant no. 15002005), by the Hungarian National Research Foundation (OTKA T046095) and by the FP6 project MKTD-CT-2004-509252.

References

- [1] Halzen F and Martin A D 1984 *Quarks and Leptons: An Introductory Course in Modern Particle Physics* (New York: Wiley)
- [2] Yamazaki T, Morita N, Hayano R S, Widmann E and Eades J 2002 Antiprotonic helium *Phys. Rep.* **366** 183–329
- [3] Cohen A G, De Rujula A and Glashow S L 1998 A matter-antimatter universe? *Astrophys. J.* **495** 539–49 (Preprint [astro-ph/9707087](#))
- [4] Weinberg S 2005 *The Quantum Theory of Fields* vol 1 (Cambridge: Cambridge University Press)
- [5] Particle Data Group W-M Yao *et al* 2006 Review of physics *J. Phys. G: Nucl. Phys.* **33** 1
- [6] Lee T D and Yang C N 1956 Question of parity conservation in weak interactions *Phys. Rev.* **104** 254–8
- [7] Wu C S, Ambler E, Hayward R W, Hoppes D D and Hudson R P 1957 Experimental test of parity conservation in beta decay *Phys. Rev.* **105** 1413–14
- [8] Garwin R L, Lederman L M and Weinrich M 1957 Observations of the failure of conservation of parity and charge conjugation in meson decays: the magnetic moment of the free muon *Phys. Rev.* **105** 1415–17
- [9] Colladay D and Kostelecký V A 1997 CPT violation and the standard model *Phys. Rev. D* **55** 6760–74
- [10] Colladay D and Kostelecký V A 1998 Lorentz-violating extension of the standard model *Phys. Rev. D* **58** 116002 (Preprint [hep-ph/9809521](#))
- [11] Kostelecký V A 2001 Topics in Lorentz and CPT violation 2001 *The Role of Neutrinos, Strings, Gravity, and Variable Cosmological Constant in Elementary Particle Physics (Coral Gables, Ft. Lauderdale, FL, 14–17 December 2000)* pp 57–68 (Preprint [hep-ph/0104227](#))
- [12] Kostelecký V A 2004 Gravity, Lorentz violation, and the standard model *Phys. Rev. D* **69** 105009
- [13] Kostelecký V A and Lehnert R 2001 Stability, causality, and Lorentz and CPT violation *Phys. Rev. D* **63** 065008
- [14] Lehnert R 2006 CPT- and Lorentz-symmetry breaking: a review Preprint [hep-ph/0611177](#)
- [15] Mavromatos N E 2005 CPT violation and decoherence in quantum gravity *Lect. Notes Phys.* **669** 245–320
- [16] Klinkhamer F R and Rupp C 2004 Spacetime foam, CPT anomaly, and photon propagation *Phys. Rev. D* **70** 045020
- [17] Mavromatos N E 2005 CPT violation: theory and phenomenology *Int. Conf. on Exotic Atoms (EXA 2005) (Vienna, Austria, 21–25 February 2005)* pp 361–72 (Preprint [hep-ph/0504143](#))
- [18] Mavromatos N E 2006 CPT and quantum mechanics tests with kaons: theory Preprint [hep-ph/0607320](#)
- [19] Barenboim G and Mavromatos N 2004 Decoherent neutrino mixing, dark energy, and matter-antimatter asymmetry *Phys. Rev. D* **70** 93015
- [20] Greenberg O 2002 CPT violation implies violation of Lorentz invariance *Phys. Rev. Lett.* **89** 231602
- [21] Aguilar A *et al* 2001 Evidence for neutrino oscillations from the observation of $\bar{\nu}_e$ appearance in a $\bar{\nu}_\mu$ beam *Phys. Rev. D* **64** 112007
- [22] Murayama H and Yanagida T 2001 LSND, SN1987A, and CPT violation *Phys. Lett. B* **520** 263–8
- [23] Barenboim G, Beacom J F, Borissov L and Kayser B 2002 CPT violation and the nature of neutrinos *Phys. Lett. B* **537** 227–32 (Preprint [hep-ph/0203261](#))
- [24] Kostelecký V A and Mewes M 2004 Lorentz and CPT violation in neutrinos *Phys. Rev. D* **69** 016005
- [25] Barenboim G, Mavromatos N, Sarkar S and Waldron-Lauda A 2006 Quantum decoherence and neutrino data *Nucl. Phys. B* **758** 90–111 (Preprint [hep-ph/0603028](#))
- [26] Klinkhamer F R 2006 Possible new source of T and CP violation in neutrino oscillations *Phys. Rev. D* **73** 057301
- [27] Auerbach L B *et al* 2005 Tests of Lorentz violation in $\bar{\nu}_\mu \rightarrow \bar{\nu}_e$ oscillations *Phys. Rev. D* **72** 076004
- [28] Aguilar-Arevalo A A *et al* 2007 A search for electron neutrino appearance at the $\delta m^2 \sim 1 \text{ eV}^2$ scale *Phys. Rev. Lett.* submitted (Preprint [0704.1500](#))
- [29] Katori T, Kostelecký V A and Tayloe R 2006 Global three-parameter model for neutrino oscillations using Lorentz violation *Phys. Rev. D* **74** 105009

- [30] Kostelecký V A (ed) 2004 CPT and Lorentz symmetry *Proc. 3rd Meeting (Bloomington, USA, 4–7 August, 2004) (Prepared for 3rd Meeting on CPT and Lorentz Symmetry (CPT 04) (Bloomington, IN, 4–7 August 2004))*
- [31] Dehmelt H, Mittleman R, Van Dyck R S Jr and Schwinberg P 1999 Past electron-positron g-2 experiments yielded sharpest bound on CPT violation for point particles *Phys. Rev. Lett.* **83** 4694
- [32] Gabrielse G, Khabbaz A, Hall D S, Heimann C, Kalinowsky H and Jhe W 1999 Precision mass spectroscopy of the antiproton and proton using simultaneously trapped particles *Phys. Rev. Lett.* **82** 3198–201
- [33] Thompson J, Rainville S and Pritchard D 2004 Cyclotron frequency shifts arising from polarization forces *Nature* **430** 58–61
- [34] Bluhm R, Kostelecký V A and Russell N 1998 CPT and Lorentz tests in Penning traps *Phys. Rev. D* **57** 3932–43
- [35] Hughes V W, Perdekamp M G, Kawall D, Liu W, Jungmann K and zu Putlitz G 2001 Test of CPT and Lorentz invariance from muonium spectroscopy *Phys. Rev. Lett.* **87** 111804
- [36] Phillips D F, Humphrey M A, Mattison E M, Stoner R E, Vessot RFC and Walsworth R L 2001 Limit on Lorentz and CPT violation of the proton using a hydrogen maser *Phys. Rev. D* **63** 111101
- [37] Bear D, Stoner R E, Walsworth R L, Kostelecký V A and Lane C D 2000 Limit on Lorentz and CPT violation of the neutron using a two-species noble-gas maser *Phys. Rev. Lett.* **85** 5038–41
- [38] Canè F, Bear D, Phillips D, Rosen M, Smallwood C, Stoner R, Walsworth R and Kostelecký V 2004 Bound on Lorentz and CPT violating boost effects for the neutron *Phys. Rev. Lett.* **93** 230801
- [39] Aubert B *et al* and (The BaBar Collaboration) 2006 Search for CPT and Lorentz violation in $B^0 - \bar{B}^0$ oscillations with inclusive dilepton events *Preprint hep-ex/0607103*
- [40] Leonidopoulos C 2001 $B_d^0 \bar{B}_d^0$ mixing and CPT tests at BELLE *Preprint hep-ex/0107001*
- [41] Kostelecký V A 1998 Sensitivity of CPT tests with neutral mesons *Phys. Rev. Lett.* **80** 1818
- [42] Feng B, Li M, Xia J Q, Chen X and Zhang X 2006 Searching for CPT violation with WMAP and Boomerang *Phys. Rev. Lett.* **96** 221302 (*Preprint astro-ph/0601095*)
- [43] Kostelecký A and Mewes M 2007 Lorentz-violating electrodynamics and the cosmic microwave background *Preprint astro-ph/0702379*
- [44] Ellis J R, Mavromatos N E, Nanopoulos D V, Sakharov A S and Sarkisyan E K G 2006 Robust limits on Lorentz violation from gamma-ray bursts *Astropart. Phys.* **25** 402–11
- [45] The Antiproton Decelerator at CERN <http://psdoc.web.cern.ch/PSdoc/acc/ad/index.html>
- [46] Niering M *et al* 2000 Measurement of the hydrogen 1S–2S transition frequency by phase coherent comparison with a microwave cesium fountain clock *Phys. Rev. Lett.* **84** 5496–9
- [47] Bluhm R, Kostelecký V A and Russell N 1999 CPT and Lorentz tests in hydrogen and antihydrogen *Phys. Rev. Lett.* **82** 2254–7
- [48] Amoretti M *et al* 2002 Production and detection of cold antihydrogen atoms *Nature* **419** 456–9
- [49] Gabrielse G *et al* 2002 Background-free observation of cold antihydrogen with field-ionization analysis of its states *Phys. Rev. Lett.* **89** 213401
- [50] Mohr P J and Taylor B N 2005 CODATA recommended values of the fundamental physical constants: 2002 *Rev. Mod. Phys.* **77** 1–107
- [51] Hori M *et al* 2006 Determination of the antiproton-to-electron mass ratio by precision laser spectroscopy of $\bar{\text{p}}\text{He}^+$ *Phys. Rev. Lett.* **96** 243401
- [52] Tomonaga S and Araki G 1940 Effect of the nuclear Coulomb field on the capture of slow mesons *Phys. Rev.* **58** 90–1
- [53] Fermi E and Teller E 1947 The capture of negative mesotrons in matter *Phys. Rev.* **72** 399–408
- [54] Wightman A 1950 Moderation of negative mesons in hydrogen: I. Moderation from high energies to capture by an H_2 molecule *Phys. Rev.* **77** 521–8
- [55] Jensen T S and Markushin V E 2003 Atomic cascade and precision physics with light muonic and hadronic atoms *Lect. Notes Phys.* **627** 37–58
- [56] Day T B, Snow G A and Sucher J 1960 High-orbital s-state capture of π^- mesons by protons *Phys. Rev.* **118** 864–6
- [57] Lenz S *et al* 1998 A new determination of the mass of the charged pion *Phys. Lett. B* **416** 50–5
- [58] Gall K P *et al* 1988 Precision measurements of the K^- and Σ^- masses *Phys. Rev. Lett.* **60** 186–9
- [59] Denisov A S *et al* 1991 New measurements of the mass of the K^- meson *JETP Lett.* **54** 558–63
- [60] Mohr P J and Taylor B N 2000 CODATA recommended values for the physical constants: 1998 *Rev. Mod. Phys.* **72** 351–495
- [61] Farnham D L, Van Dyck R S Jr and Schwinberg P B 1995 Determination of the electron's atomic mass and the proton/electron mass ratio via Penning trap mass spectroscopy *Phys. Rev. Lett.* **75** 3598–601
- [62] Van Dyck R S Jr, Farnham D L and Schwinberg P B 1995 Precision mass measurements in the UW-PTMS and the electron's 'atomic mass' *Phys. Scr.* **59** 134

- [63] Beier T, Häffner H, Hermanspahn N, Karshenboim S G, Kluge H J, Quint W, Stahl S, Verdú J and Werth G 2001 New determination of the electron's mass *Phys. Rev. Lett.* **88** 11603
- [64] Eades J and Hartmann F J 1999 Forty years of antiprotons *Rev. Mod. Phys.* **71** 373–419
- [65] Liu W *et al* 1999 High precision measurements of the ground state hyperfine structure interval of muonium and of the muon magnetic moment *Phys. Rev. Lett.* **82** 711–14
- [66] Hertzog D W *et al* 1988 Exotic-atom measurement of the magnetic dipole moment of the σ^- hyperon *Phys. Rev. D* **37** 1142–52
- [67] Kreissl A *et al* 1988 Remeasurement of the magnetic moment of the antiproton *Z. Phys. C* **37** 557–61
- [68] Iwasaki M *et al* 1991 Discovery of antiproton trapping by long-lived metastable states in liquid helium *Phys. Rev. Lett.* **67** 1246–9
- [69] Morita N, Ohtsuki K and Yamazaki T 1993 Laser spectroscopy of metastable antiprotonic helium atomcules *Nucl. Instrum. Methods Phys. Res. A* **330** 439–46
- [70] Morita N *et al* 1994 First observation of laser-induced resonant annihilation in metastable antiprotonic helium atoms *Phys. Rev. Lett.* **72** 1180–3
- [71] Condo G T 1964 On the absorption of negative pions by liquid helium *Phys. Lett.* **9** 65
- [72] Russell J E 1969 Metastable states of $\alpha\pi^-e^-$, αK^-e^- , and $\alpha\bar{p}e^-$ atoms *Phys. Rev. Lett.* **23** 63
- [73] Russell J E 1969 Interactions of an αK^-e^- atom with a He atom *Phys. Rev.* **188** 187
- [74] Russell J E 1970 Structure of neutral mesonic atoms formed in liquid helium *Phys. Rev. A* **1** 721
- [75] Russell J E 1970 Distortion of the electron wave function in $\alpha\pi^-e^-$, αK^-e^- , and $\alpha\bar{p}e^-$ atoms *Phys. Rev. A* **1** 735
- [76] Shimamura I 1992 Moleculelike metastable states of antiprotonic and mesic helium *Phys. Rev. A* **46** 3776–88
- [77] Korobov V I 1996 Variational calculation of energy levels in $\bar{p}\text{He}^+$ molecular systems *Phys. Rev. A* **54** R1749–52
- [78] Korobov V I and Bakalov D D 1997 Energies and relativistic corrections for the metastable states of antiprotonic helium atoms *Phys. Rev. Lett.* **79** 3379–82
- [79] Korobov V I, Bakalov D and Monkhorst H J 1999 Variational expansion for antiprotonic helium atoms *Phys. Rev. A* **59** R919–21
- [80] Yamazaki T and Ohtsuki K 1992 Atomic core-polarization effects in metastable hadronic helium atoms *Phys. Rev. A* **45** 7782–6
- [81] Korobov V I 2003 Metastable states in the antiprotonic helium atom decaying via Auger transitions *Phys. Rev. Lett.* **67** 62501
- Korobov V I 2003 Metastable states in the antiprotonic helium atom decaying via Auger transitions *Phys. Rev. A* **68** 019902 (erratum)
- [82] Korobov V I 2005 Precise spectroscopy of antiprotonic helium and sensitivity of transitions to the antiproton mass *Proc. Int. Conf. on Exotic Atoms and Related Topics (EXA'05) (Vienna, 2005)* ed A Hirtl *et al* (Vienna: Austrian Academy of Sciences Press) pp 391–400
- [83] Kino Y, Kamimura M and Kudo H 1999 Non-adiabatic high-precision calculation of antiprotonic helium atomcules *Hyperfine Interact.* **119** 201–6
- [84] Kino Y, Yamanaka N, Kamimura N, Froelich P and Kudo H 2001 High-precision calculation of the energy levels and Auger decay rates of the metastable states of the antiprotonic helium atoms *Hyperfine Interact.* **138** 179–82
- [85] Elander N and Yarevsky E 1997 Finite-element calculations of the antiprotonic helium atom including relativistic and QED corrections *Phys. Rev. A* **56** 1855–64
- Elander N and Yarevsky E 1998 Finite-element calculations of the antiprotonic helium atom including relativistic and QED corrections *Phys. Rev. A* **57** 2256 (erratum)
- [86] Ho Y 1983 The method of complex coordinate rotation and its applications to atomic collision processes *Phys. Rep.* **99** 1–68
- [87] Kino Y, Kudo H and Kamimura M 2003 High-precision coulomb three-body calculation of antiprotonic helium atoms *Mod. Phys. Lett. A* **18** 388–97
- [88] Korobov V I 2001 Antiprotonic helium 'atomcule': relativistic and QED effects *Lect. Notes Phys.* **570** 517–20
- [89] Korobov V I 2006 private communication
- [90] Korobov V and Korobov S 1999 Bethe logarithm for the 1^1S and 2^1S states of helium *Phys. Rev. A* **59** 3394–6
- [91] Araki G 1957 Quantum-electrodynamical corrections to energy-levels of helium *Prog. Theor. Phys.* **17** 619–42
- [92] Sucher J 1958 Energy levels of the two-electron atom to order α^3 ry; ionization energy of helium *Phys. Rev.* **109** 1010–11
- [93] Torii H A *et al* 1999 Laser measurements of the density shifts of resonance lines in antiprotonic helium atoms and stringent constraint on the antiproton charge and mass *Phys. Rev. A* **59** 223–9
- [94] Hori M *et al* 2001 Sub-ppm laser spectroscopy of antiprotonic helium and a CPT-violation limit on the antiproton charge and mass *Phys. Rev. Lett.* **87** 093401

- [95] Hori M *et al* 2003 Direct measurements of transition frequencies of isolated $\bar{p}\text{He}^+$ atoms, and new CPT violation limits on the antiproton charge and mass *Phys. Rev. Lett.* **91** 123401
- [96] Kino Y, Yamanaka N, Kamimura M and Kudo H 2003 High precision calculation of the fine and hyperfine structure of antiprotonic helium-3,4 atoms *Hyperfine Interact.* **146–147** 331–6
- [97] Bakalov D and Korobov V I 1998 Hyperfine structure of antiprotonic helium energy levels *Phys. Rev. A* **57** 1662–7
- [98] Leon M and Miller J H 1977 Atomic capture of negative mesons (II). Fuzzy Fermi-Teller model *Nucl. Phys. A* **282** 461
- [99] Cohen J S 1983 Slowing down and capture of negative muons by hydrogen: classical-trajectory Monte Carlo calculation *Phys. Rev. A* **27** 167
- [100] Sakimoto K 2002 Antiproton, kaon, and muon capture by atomic hydrogen *Phys. Rev. A* **66** 032506
- [101] Cohen J S 2004 Capture of negative exotic particles by atoms, ions, and molecules *Rep. Prog. Phys.* **67** 1769
- [102] Möhl D 1997 Production of low-energy antiprotons *Hyperfine Interact.* **109** 33
- [103] Baird S *et al* 1998 Overview of the recent operation of the AAC and LEAR for the low-energy antiproton physics programme *Proc. 1997 Particle Accelerator Conf. (Vancouver)* p 982
- [104] Klempt E, Bradamante F, Martin A and Richard J M 2002 Antinucleon-nucleon interaction at low energy: scattering and protonium *Phys. Rep.* **368** 119
- [105] Maury S 1997 The antiproton decelerator: AD *Hyperfine Interact.* **109** 43
- [106] Belochitskii P and Eriksson T 2001 The CERN Antiproton Decelerator (AD) operation, progress, and plans for the future *PBAR01 (Aarhus, Denmark, 14–15 September 2001)*
- [107] Belochitskii P, Eriksson T and Maury S 2004 The CERN antiproton decelerator (AD) in 2002: status, progress and machine development results *Nucl. Instrum. Methods Phys. Res. B* **214** 176
- [108] van der Meer S 1985 Stochastic cooling and the accumulation of antiprotons *Rev. Mod. Phys.* **57** 689
- [109] Möhl D, Petrucci G, Thorndahl L and van der Meer S 1980 Physics and technique of stochastic cooling *Phys. Rep.* **58** 73–119
- [110] Poth H 1990 Electron cooling: theory, experiment, application *Phys. Rep.* **196** 135
- [111] Bosser J, Chanel M, Ley R, Möhl D, Ollenhauer F and Tranquille G 1990 Status of electron cooling experiments at LEAR *Workshop on Electron Cooling and New Cooling Techniques (Legnaro, Italy, 15–17 May 1990)*
- [112] Møller S P, Csete A, Ichioka T, Knudsen H, Uggerhøj U I and Andersen H H 2002 Antiproton stopping at low energies: confirmation of velocity-proportional stopping power *Phys. Rev. Lett.* **88** 193201
- [113] Møller S P, Csete A, Ichioka T, Knudsen H, Uggerhøj U I and Andersen H H 2004 Stopping power in insulators and metals without charge exchange *Phys. Rev. Lett.* **93** 42502
- [114] Kuroda N *et al* 2005 Confinement of a large number of antiprotons and production of an ultraslow antiproton beam *Phys. Rev. Lett.* **94** 023401
- [115] Gabrielse G *et al* 2004 First measurement of the velocity of slow antihydrogen atoms *Phys. Rev. Lett.* **93** 073401
- [116] Storry C H *et al* 2004 First laser-controlled antihydrogen production *Phys. Rev. Lett.* **93** 263401
- [117] Gabrielse G 2005 Atoms made entirely of antimatter: two methods produce slow antihydrogen *Adv. At. Mol. Opt. Phys.* **50** 155
- [118] Amoretti M *et al* 2004 High rate production of antihydrogen *Phys. Lett. B* **578** 23–32
- [119] Amoretti M *et al* 2006 Search for laser-induced formation of antihydrogen atoms *Phys. Rev. Lett.* **97** 213401
- [120] Holzscheiter M H and Charlton M 2004 The route to ultra-low energy antihydrogen *Phys. Rep.* **402** 1
- [121] Squires T M, Yesley P and Gabrielse G 2001 Stability of a charged particle in a combined Penning-Ioffe trap *Phys. Rev. Lett.* **86** 5266
- [122] Gabrielse G *et al* 2007 Antiproton confinement in a Penning-Ioffe trap for antihydrogen *Phys. Rev. Lett.* **98** 113002
- [123] Andresen G *et al* 2007 Antimatter plasmas in a multipole trap for antihydrogen *Phys. Rev. Lett.* **98** 023402
- [124] Holzscheiter M H *et al* 2006 The biological effectiveness of antiproton irradiation *Radiother. Oncol.* **81** 233
- [125] Yamazaki T *et al* 1993 Formation of long-lived gas-phase antiprotonic helium atoms and quenching by H_2 *Nature* **361** 238–40
- [126] Kino Y, Kamimura M and Kudo H 2004 Numerical accuracy of the energy levels of antiprotonic helium atoms *Nucl. Instrum. Methods Phys. Res. B* **412** 84–8
- [127] Hori M *et al* 1998 Laser spectroscopic studies of state-dependent collisional quenching of the lifetimes of metastable antiprotonic helium atoms *Phys. Rev. A* **57** 1698–712
Hori M *et al* 1998 Laser spectroscopic studies of state-dependent collisional quenching of the lifetimes of metastable antiprotonic helium atoms *Phys. Rev. A* **58** 1612–27 (erratum)
- [128] Beck W A, Wilets L and Alberg M A 1993 Semiclassical description of antiproton capture on helium atoms *Phys. Rev. A* **48** 2779–85
- [129] Russell J E 1970 Auger rates for circular orbits of $\alpha\pi^-e^-$, αK^-e^- , and αpe^- atoms *Phys. Rev. A* **1** 742

- [130] Ahlrichs R, Dumbraijs O, Pilkuhn H and Schlaile H G 1982 Antiprotonic helium and lithium with one or two electrons *Z. Phys. A* **306** 297–300
- [131] Nakamura S N *et al* 1994 Delayed annihilation of antiprotons in helium gas *Phys. Rev. A* **49** 4457–65
- [132] Hori M *et al* 2004 Populations and lifetimes in the $v = n - l - 1 = 2$ and 3 metastable cascades of $\bar{p}\text{He}^+$ measured by pulsed and continuous antiproton beams *Phys. Rev. A* **70** 012504
- [133] Greenland P T and Thürwächter R 1993 The antiprotonic helium atom *Hyperfine Interact.* **76** 355–69
- [134] Korobov V I and Shimamura I 1997 Auger transition rates for metastable states of antiprotonic helium $\text{He}^+\bar{p}$ *Phys. Rev. A* **56** 4587–94
- [135] Bakalov D, Jeziorski B, Korona T, Szalewicz K and Tchoukova E 2000 Density shift and broadening of transition lines in antiprotonic helium *Phys. Rev. Lett.* **84** 2350–3
- [136] Hori M 2004 Parallel plate chambers for monitoring the profiles of high-intensity pulsed antiproton beams *Nucl. Instrum. Methods Phys. Res. A* **522** 420
- [137] Hori M, Yamashita K, Hayano R S and Yamazaki T 2003 Analog Cherenkov detectors used in laser spectroscopy experiments on antiprotonic helium *Nucl. Instrum. Methods Phys. Res. A* **496** 102
- [138] Hori M, Hayano R S, Widmann E and Torii H 2003 Resolution enhancement of $\bar{p}\text{He}^+$ atomic line profiles measured with a pulsed dye laser and a Fizeau wavelength meter *Opt. Lett.* **28** 2479–81
- [139] Mishin V I, Fedoseyev V N, Kluge H J, Letokhov V S, Ravn H L, Scheerer F, Shirakabe Y, Sundell S and Tengblad O 1993 Chemically selective laser ion-source for the CERN-ISOLDE on-line mass separator facility *Nucl. Instrum. Methods Phys. Res. B* **73** 550
- [140] Engel T *et al* 1997 Laser systems specialized for laser spectroscopy at storage rings *Hyperfine Interact.* **108** 251
- [141] Van Duppen P, Bruyneel B, Huyse M, Kudryavtsev Y, Van Den Bergh P and Vermeeren L 2000 Beams of short lived nuclei by selective laser ionization in a gas cell *Hyperfine Interact.* **127** 401
- [142] Pohl R *et al* 2005 The muonic hydrogen Lamb-shift experiment *Can. J. Phys.* **83** 339
- [143] Hänsch T W 1972 Repetitively pulsed tunable dye laser for high resolution spectroscopy *Appl. Opt.* **11** 895
- [144] Westling L A, Raymer M G and Snyder J J 1984 Single-shot spectral measurements and mode correlations in a multimode pulsed dye laser *J. Opt. Soc. Am. B* **1** 150–4
- [145] Kajava T T, Lauranto H M and Salomaa R R E 1992 Mode structure fluctuations in a pulsed dye laser *Appl. Opt.* **31** 6987–92
- [146] Velchev I, van Dierendonck R, Hogervorst W and Ubachs W 1998 A dense grid of reference iodine lines for optical frequency calibration in the range 571–596 nm *J. Mol. Spectrosc.* **187** 21
- [147] Xu S C, van Dierendonck R, Hogervorst W and Ubachs W 2000 A dense grid of reference iodine lines for optical frequency calibration in the range 595–655 nm *J. Mol. Spectrosc.* **201** 256
- [148] Bodermann B, Klug M, Winkelhoff U, Knöckel H and Tiemann E 2000 Precise frequency measurements of I_2 lines in the near infrared by Rb reference lines *Eur. Phys. J. D* **11** 213
- [149] Barbieri B, Beverini N and Sasso A 1990 Optogalvanic spectroscopy *Rev. Mod. Phys.* **62** 603–44
- [150] Hori M *et al* 2002 Primary populations of metastable antiprotonic ^4He and ^3He atoms *Phys. Rev. Lett.* **89** 093401
- [151] Hayano R S *et al* 1994 Laser studies of the decay chain of metastable antiprotonic helium atoms *Phys. Rev. Lett.* **73** 1485–8
- Hayano R S *et al* 1994 Laser studies of the decay chain of metastable antiprotonic helium atoms *Phys. Rev. Lett.* **73** 3181 (erratum)
- [152] Widmann E *et al* 1997 Hyperfine structure of the metastable $\bar{p}\text{He}^+$ atomcule revealed by a laser-induced $(n, l) = (37, 35) \rightarrow (38, 34)$ transition *Phys. Lett. B* **404** 15–19
- [153] Yamanaka N, Kino Y, Kudo H and Kamimura M 2000 Coupled rearrangement channel calculation of the fine and hyperfine structures of the antiprotonic helium atoms *Phys. Rev. A* **63** 012518
- [154] Yamaguchi H *et al* 2002 Anomalies in the decay rates of antiprotonic helium-atom states *Phys. Rev. A* **66** 022504
- [155] Kartavtsev O, Monakhov D and Fedotov S 2000 Auger decay rates of antiprotonic helium *Phys. Rev. A* **61** 062507
- Kartavtsev O, Monakhov D and Fedotov S 2000 Auger decay rates of antiprotonic helium *Phys. Rev. A* **61** 019901(E) (erratum)
- [156] Korobov V I 1999 Metastable states of antiprotonic helium *Hyperfine Interact.* **119** 185–93
- [157] Yamaguchi H *et al* 2004 Systematic study of the decay rates of antiprotonic helium states *Phys. Rev. A* **70** 012501
- [158] Lombardi A M, Pirkl W and Bylinsky Y 2001 First operating experience with the CERN decelerating RFQ for antiprotons *Proc. 2001 Particle Physics Accelerator Conf. (Chicago, IL, 18–22 June 2001)* ed P Lucasa and S Webber (Piscataway, NJ: IEEE) pp 585–7
- [159] Paul W 1990 Electromagnetic traps for charged and neutral particles *Rev. Mod. Phys.* **62** 531
- [160] Hori M 2005 Photocathode microwire monitor for nondestructive and highly sensitive spatial profile measurements of ultraviolet, x-ray, and charged particle beams *Rev. Sci. Instrum.* **76** 113303

- [161] Korobov V I 2006 Hyperfine structure of metastable states in $\bar{p}^3\text{He}^+$ atom *Phys. Rev. A* **73** 22509
- [162] Hori M *et al* 2005 Observation of cold, long-lived antiprotonic helium ions *Phys. Rev. Lett.* **94** 063401
- [163] Korobov V I 1998 Metastable states of antiprotonic helium atoms *Frontier Tests of Quantum Electrodynamics and Physics of the Vacuum* ed E Zavattini E *et al* (Sofia: Heron Press) pp 215–21
- [164] Udem T, Holzwarth R and Hänsch T W 2002 Optical frequency metrology *Nature* **416** 233–7
- [165] Holzwarth R, Udem T, Hänsch T W, Knight J C, Wadsworth W J and Russell P S J 2000 Optical frequency synthesizer for precision spectroscopy *Phys. Rev. Lett.* **85** 2264–7
- [166] Jones D J, Diddams S A, Ranka J K, Stentz A, Windeler R S, Hall J L and Cundiff S T 2000 Carrier-envelope phase control of femtosecond mode-locked lasers and direct optical frequency synthesis *Science* **288** 635
- [167] Eikema KSE, Ubachs W, Vassen W and Hogervorst W 1997 Lamb shift measurement in the 1^1S ground state of helium *Phys. Rev. A* **55** 1866–84
- [168] Fee M S, Danzmann K and Chu S 1992 Optical heterodyne measurement of pulsed lasers: toward high-precision pulsed spectroscopy *Phys. Rev. A* **45** 4911–24
- [169] Reinhard I, Gabrysch M, Fischer von Weikersthal B, Jungmann K and zu Putlitz G 1996 Measurement and compensation of frequency chirping in pulsed dye laser amplifiers *Appl. Phys. B* **63** 467–72
- [170] Fischer M *et al* 2004 New limits on the drift of fundamental constants from laboratory measurements *Phys. Rev. Lett.* **92** 230802
- [171] Yiannopoulou A, Melikechi N, Gangopadhyay S, Meiners J C, Cheng C H and Eyler E E 2006 Determinations of $\text{EF } ^1\Sigma_g^+ \leftarrow X ^1\Sigma_g^+$ transition frequencies in H_2 , D_2 and HD *Phys. Rev. A* **73** 022506
- [172] Reinhold E, Buning R, Hollenstein U, Ivanchik A, Petitjean P and Ubachs W 2006 Indication of a cosmological variation of the proton-electron mass ratio based on laboratory measurement and reanalysis of H_2 spectra *Phys. Rev. Lett.* **96** 151101
- [173] Bergeson S D *et al* 1998 Measurement of the He ground state Lamb shift via the two-photon $1^1\text{s}-2^1\text{s}$ transition *Phys. Rev. Lett.* **80** 3475
- [174] Maas F E *et al* 1994 A measurement of the $1\text{s}-2\text{s}$ transition frequency in muonium *Phys. Lett. A* **187** 247–54
- [175] Meyer V *et al* 2000 Measurement of the $1\text{s}-2\text{s}$ energy interval in muonium *Phys. Rev. Lett.* **84** 1136–9
- [176] Chu S and Mills A P Jr 1984 Measurements of the positronium $1^3\text{S}_1-2^3\text{S}_1$ interval by Doppler-free two-photon spectroscopy *Phys. Rev. Lett.* **52** 1689
- [177] Oskay W H *et al* 2006 Single-atom optical clock with high accuracy *Phys. Rev. Lett.* **97** 020801
- [178] Hori M, Dax A and Hayano R S Fluctuations in the frequency chirp of a nanosecond continuous-wave pulse-amplified dye laser, unpublished
- [179] Hori M *et al* ppb-scale laser spectroscopy of antiprotonic helium, unpublished
- [180] Korobov V I 2007 Private communication
- [181] Widmann E *et al* 2002 Hyperfine structure of antiprotonic helium revealed by a laser-microwave-laser resonance method *Phys. Rev. Lett.* **89** 243402
- [182] Sakaguchi J 2003 Observation of hyperfine and superhyperfine structure of antiprotonic helium atom by laser-microwave spectroscopy *PhD Thesis* University of Tokyo
- [183] Sakaguchi J *et al* 2004 Study of the hyperfine structure of antiprotonic helium *Nucl. Instrum. Methods Phys. Res. B* **214** 89
- [184] Sakaguchi J *et al* 2004 Cryogenic tunable microwave cavity at 13 GHz for hyperfine spectroscopy of antiprotonic helium *Nucl. Instrum. Methods Phys. Res. A* **533** 598–611
- [185] Korenman GYa, Yudin N and Yudin S 2004 Collisional effects on HFS transitions of antiprotonic helium *Nucl. Instrum. Methods Phys. Res. B* **214** 94–7
- [186] Korenman GYa and Yudin S 2006 Coupled-channel analysis of collisional effects on hfs transitions in antiprotonic helium atoms *J. Phys. B: At. Mol. Opt. Phys.* **39** 1473–84
- [187] Bakalov D 2001 private communication
- [188] Korobov V I and Bakalov D 2001 Fine and hyperfine structure of the (37,35) state of the $^4\text{He}^+\bar{p}$ atom *J. Phys. B: At. Mol. Opt. Phys.* **34** L519
- [189] Bakalov D 1999 Measuring the fine and hyperfine structure of antiprotonic helium *Nucl. Phys. A* **655** 301c–5
- [190] Bakalov D and Widmann E 2007 Determining the antiproton magnetic moment from measurements of the hyperfine structure of antiprotonic helium *Phys. Rev. A* **76** 012512
- [191] Day T B 1960 K^- -meson capture by helium 1960 *Nouvo Cimento* **18** 381–93
- [192] Leon M and Bethe H A 1962 Negative meson absorption in liquid hydrogen *Phys. Rev.* **127** 636–47
- [193] Bethe H A and Salpeter E E 1957 *Quantum Mechanics of One- and Two-Electron Atoms* (Berlin: Springer)
- [194] Reifenröther G, Klempf E and Landua R 1988 Cascade of antiprotonic helium atoms *Phys. Lett. B* **203** 9–12
- [195] CODATA Internationally recommended values of the fundamental physical constants: 2006 <http://physics.nist.gov/cuu/Constants/index.html>